Università degli Studi di Napoli *Federico II*

Dark Matter indirect detection at Neutrino Telescopes: a multi-messenger approach

Dottorando
Marco Chianese

Tutori
Prof. Gennaro Miele
Dr.   Stefano Morisi

Anni 2014/2017

Contents

Publications

The thesis is based on the following publications:

[1] S. M. Boucenna, M. Chianese, G. Mangano, G. Miele, S. Morisi, O. Pisanti and E. Vitagliano, *Decaying Leptophilic Dark Matter at IceCube*, JCAP **1512** (2015) no.12, 055 [arXiv:1507.01000 [hep-ph]].

[2] M. Chianese, G. Miele, S. Morisi and E. Vitagliano, *Low energy IceCube data and a possible Dark Matter related excess*, Phys. Lett. B **757** (2016) 251 [arXiv:1601.02934 [hep-ph]].

[3] M. Chianese and A. Merle, *A Consistent Theory of Decaying Dark Matter Connecting IceCube to the Sesame Street*, JCAP **1704** (2017) no.04, 017 [arXiv:1607.05283 [hep-ph]].

[4] M. Chianese, G. Miele and S. Morisi, *Dark Matter interpretation of low energy IceCube MESE excess*, JCAP **1701** (2017) no.01, 007 [arXiv:1610.04612 [hep-ph]].

[5] M. Chianese, R. Mele, G. Miele, P. Migliozzi and S. Morisi, *Use of ANTARES and IceCube data to constrain single power-law neutrino flux*, arXiv:1707.05168 [hep-ph].

[6] M. Chianese, G. Miele and S. Morisi, *Interpreting IceCube 6-year HESE data as an evidence for hundred TeV decaying Dark Matter*, Phys. Lett. B **773** (2017) 591 [arXiv:1707.05241 [hep-ph]].

Other articles completed during the PhD only partially included here:

[7] Z. Berezhiani, M. Chianese, G. Miele and S. Morisi, *Chances for SUSY-GUT in the LHC Epoch*, JHEP **1508** (2015) 083 [arXiv:1505.04950 [hep-ph]].

[8] F. Buccella, M. Chianese, G. Mangano, G. Miele, S. Morisi and P. Santorelli, *A neutrino mass-mixing sum rule from SO(10) and neutrinoless double beta decay*, JHEP **1704** (2017) 004 [arXiv:1701.00491 [hep-ph]].

Other articles completed during the PhD but not included here:

[9] M. Chianese, E. Di Grezia, M. Manfredonia and G. Miele, *Characterising exotic matter driving wormholes*, Eur. Phys. J. Plus **132** (2017) no.4, 164 [arXiv:1701.08770 [gr-qc]].

Introduction

After more than 80 years from its first evidence in the Coma galaxy cluster, dark matter represents one of the deepest mystery in current physics. Even though its existence is strongly suggested by several gravitational effects such as the anomalies of galactic rotation curves, the gravitational lensing, the bullet clusters and the cosmological observations, the nature of dark matter still remains unknown. The most attractive and simplest scenario is the one dubbed as Weakly Interacting Massive Particle (WIMP) paradigm in which dark matter particles typically have a mass in the GeV–TeV range and interactions of the order of weak processes. However, the lacking detection of a signal related to dark matter has led to very stringent constraints to the WIMP paradigm, encouraging physicists to look for alternatives to it. During the last decades, different interesting schemes have been investigated in elementary particle physics in order to allocate viable dark matter candidates. In the so-called dark matter *zoo*, the mass is spread over many orders of magnitude, ranging from about 10^{-32} GeV up to 10^{18} GeV (see Fig. 1 for a pictorial representation of the typical mass scales for some dark matter candidates). For instance, alternatives to WIMPs, with a mass smaller than the GeV energy scale, are represented by axions at about $10^{-6} \div 10^{-3}$ eV or keV sterile neutrinos. On the other hand, WIMPzilla generally have a mass of the order of 10^{12} GeV.

Up to now all direct, indirect and colliders searches, especially dedicated to the GeV–TeV energy range, have not provided any clear evidence for dark matter. In this context, the only viable way to look for very massive dark matter candidates, with a mass larger than TeV, is based on exploiting indirect searches in astrophysical observations. Indeed, the astrophysical measurements of high energy neutrinos and gamma-rays have opened

1
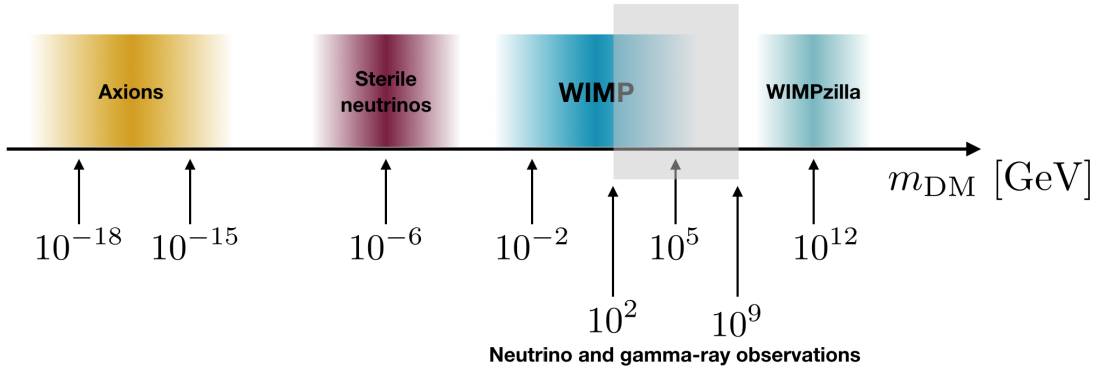
Figure 1: Pictorial representation of the typical mass scales for some promising dark matter candidates. The shaded gray area shows the energies at which modern Neutrino and Gamma-Ray Telescopes are sensitive to constrain the properties of dark matter candidates.

a new window to the cosmos (see Fig. 1), giving the chance to explore very high-energy phenomena that can be potentially linked to new physics.

The recent discovery of a diffuse neutrino flux at the TeV–PeV range by the IceCube Collaboration has ushered us into a new era for astroparticle physics, since it provides an important diagnostic tool for physics and astrophysics. The IceCube Neutrino Observatory is a neutrino telescope located at the Amundsen-Scott South Pole Station, able to observe highly energetic neutrinos reaching the Earth's surface. In six year of data-taking (2010–2016), the IceCube detector has collected 82 High Energy Starting Events (HESE) with energies larger than about 10 TeV. Moreover, for the first time, three events fully contained in the detector with energy larger than PeV (Ernie (1.14 PeV), Bert (1.04 PeV), and Big Bird (2.2 PeV)) have been observed. In the other hemisphere, from 2007 to 2015, the ANTARES Neutrino Telescope has additionally observed 33 events with energies above 20 TeV. All these events correspond to the most energetic neutrinos ever measured and offer the possibility to study neutrino physics at energies where phenomena beyond the Standard Model (SM) can be relevant. The origin of such high energy neutrinos still remains unclear: they can be produced by a variety of galactic and extragalactic astrophysical sources, or they could be intriguingly related to dark matter.

In this context, this thesis aims to investigate the relation of the dark matter paradigm

to neutrino and gamma-ray telescopes. Indeed, depending on the interaction with SM particles, dark matter can decay or annihilate producing high-energy neutrinos and gamma-rays. Hence, one can infer the properties of dark matter particles that are able to provide a detectable signal by comparing the predicted neutrino and gamma-ray fluxes with the corresponding astrophysical observations. Such studies based on characterizing at the same time the neutrino and gamma-ray fluxes are defined as *multi-messenger* analyses. In this thesis, we deeply analyze the scenario where the diffuse TeV–PeV neutrino flux is explained in terms of a two-component flux, one of which is related to dark matter. The two-component flux is indeed suggested by the tension of neutrino data, taken by IceCube and ANTARES telescopes, with the simple assumption of a single power-law, behavior that is expected in case of standard astrophysical sources once a correlation with hadronic cosmic-rays is reasonably considered. Indeed, since one would expect a hard power-law (spectral index smaller than 2.3) according to the gamma-ray and up-going muon neutrino observations, the diffuse neutrino flux shows a 2–3σ excess at 10–100 TeV energies, pointing towards a two-component neutrino flux. Remarkably, such a *low-energy excess* is present in different IceCube and ANTARES data samples. Once such a tension is statistically characterized, we focus on the scenario where the low-energy excess is intriguingly due to dark matter. For this purpose, we phenomenologically scrutinize several dark matter models characterized by distinct interactions with the Standard Model particles and by different halo density distributions of our galaxy. Moreover, we show that the dark matter models proposed to explain the diffuse neutrino flux are further constrained once the gamma-ray observations, measured for instance at Fermi-LAT, are taken into account. This strongly underlines the paramount importance of multi-messenger analysis in the attempt to unveil the nature of dark matter.

The thesis is organized as follows. In the first Chapter we briefly introduce the Standard Model and, in particular, we discuss theoretical open problems and experimental observations (like the ones related to the neutrino physics) that underline the need to go beyond. The second Chapter is devoted to dark matter: all its evidence and its properties are presented, different production mechanisms are described, a list of dark matter candidates is reported and the status of dark matter searches is reviewed. In the third Chapter, we

introduce all the ingredients required to compute the flux of neutrinos and gamma-rays that are produced by decaying/annihilating dark matter particles. The fourth Chapter is dedicated to review the physics and the observations of Neutrino Telescopes. Moreover, we also report the first combined analysis of IceCube and ANTARES measurements, highlighting the tension of data with the assumption of a single power-law explaining the diffuse neutrino flux. In the fifth Chapter, the low-energy excess is statistically characterize and its interpretation in terms of a dark matter signal is investigated by performing analyses on the angular distribution and the energy spectrum of the observed neutrinos. In the sixth Chapter, we propose a complete theoretical framework allocating a very heavy leptophilic dark matter candidate. Here, the model is constrained by examining its predictions for the neutrino flux and by requiring a viable production mechanism in the early Universe. Finally, the last Chapter is devoted to the conclusions.

Chapter 1

The Standard Model and Beyond

A series of measurements performed at high-energy particle colliders, as the Stanford Linear Collider (SLC), the Super Proton Synchrotron (SPS), the Large Electron-Positron collider (LEP), the TEVATRON and the Large Hadron Collider (LHC), has established the Standard Model (SM) as a precise theory of particle interactions up to energies of the order of 100 GeV. The SM includes the electroweak theory describing the electromagnetic and weak interactions of elementary particles, which was originally formulated by S.L. Glashow [10], S. Weinberg [11] and A. Salam [12], and the quantum chromodynamics [13, 14, 15, 16]. The model also incorporates the Brout-Englert-Higgs mechanism [17, 18, 19] through which the matter and interaction fields become massive. The recent discovery of the Higgs boson by ATLAS [20] and CMS [21] Collaborations at LHC has represented the last piece that has once again confirmed the predictive effectiveness of the SM.

The most important conceptual basis upon which the SM is built is the gauge principle [22]. The invariance under a local gauge symmetry was originally proposed in the Quantum Electrodynamic (QED) where, according to the conservation of the electric charge, the global symmetry of the theory is promoted to a local one: the interactions are then fixed by the requirement of the invariance under the local gauge transformations of the $U(1)$ group. Such a gauge principle has been generalized to any compact Lie group providing the conceptual basis to build any quantum field theory model [23].

The Chapter is organized as follows. In the first Section we introduce the readers to the

Name	1st Family	2nd Family	3rd Family
Leptons	ν_e	ν_μ	ν_τ
	e	μ	τ
Quarks	u	c	t
	d	s	b

Table 1.1: Three families of the SM matter content divided in Leptons and Quarks.

SM. In the second Section we report all the conceptual theoretical problems and physical phenomena that are not accounted for in the SM. The last Section is devoted to briefly review the neutrino phenomenology.

1.1   Standard Model in a nutshell

Let us present a very short overview of the Standard Model in oder to provide some notation and concepts used in this thesis. The Standard Model is a renormalizable[1] gauge theory based on the $SU_C(3) \otimes SU_L(2) \otimes U_Y(1)$ group. The subscript C, L and Y mean color, left-handed chirality and weak hypercharge, respectively. In particular, the $SU_C(3)$ group is the local symmetry group of the quantum chromodynamics describing the strong interactions, while the $SU_L(2) \otimes U_Y(1)$ is the Glashow-Weinberg-Salam theory of the electroweak interactions. The matter content of the SM consists of three copies (families) of fermions. Each family contains 15 chiral fermions, i.e. 2 charged and 1 neutral (neutrino) leptons, and 12 quarks (see Tab. 1.1). The three generations of quarks and leptons have identical properties except for different masses. In addition to fermions, the model contains two spin zero scalar particles gathering the Higgs field and 12 vector fields. The irreducible representations of all the SM fields are reported in Tab. 1.2. We note that the SM is an *axial* or *chiral* theory since the left-handed (L) and right-handed (R) chiral components of the fermion fields belong to different irreducible representations of the gauge symmetry group.   The hyperchage assignments follow the Gell-Mann-Nishijima relation

$$Q = I_3 + Y \, ,\tag{1.1}$$

---

[1]The SM renormalizability was proved by G. 't Hooft and M. Veltman in 1971 [24].

Name	Fields	$SU_L(2)$	$U_Y(1)$	$SU_C(3)$
Leptons	$L_{\alpha L} \equiv \begin{pmatrix} \nu_{\alpha L} \\ l_{\alpha L} \end{pmatrix}$	**2**	$-\frac{1}{2}$	**1**
	$\ell_{\alpha R}$	**1**	-1	**1**
Quark	$Q_{\beta L} \equiv \begin{pmatrix} u_{\beta L} \\ d_{\beta L} \end{pmatrix}$	**2**	$+\frac{1}{6}$	**3**
	$u_{\beta R}$	**1**	$+\frac{2}{3}$	**3**
	$d_{\beta R}$	**1**	$-\frac{1}{3}$	**3**
Higgs	$H \equiv \begin{pmatrix} H^+ \\ H^0 \end{pmatrix}$	**2**	$+\frac{1}{2}$	**1**
Gauge Bosons	B_μ	**1**	0	**1**
	W_μ^a	**3**	0	**1**
	G_μ^b	**1**	0	**8**

Table 1.2: Irreducible representations of the SM fields: $\alpha = e,\ \mu,\ \tau,\ \beta = u,\ c,\ t$ for u-quark and $\beta = d,\ s,\ b$ for d-quark, $a = 1, 2, 3$ and $b = 1, ..., 8$.

which provides the electric charge Q in terms of the third component of the weak isospin I_3 and the hypercharge Y. In the Tab. 1.2, we have neglected the three color indexes of the quarks. Moreover, since in the SM neutrinos are massless, only left-handed neutrinos are present.

The SM Lagrangian can be divided into four conceptually different pieces[2]: Dirac, Gauge (Yang-Mills), Yukawa, and Higgs interactions.

$$\mathcal{L}_{SM} = \mathcal{L}_{Dirac} + \mathcal{L}_{Gauge} + \mathcal{L}_{Higgs} + \mathcal{L}_{Yukawa}\,. \tag{1.2}$$

The first term contains the kinetic terms

$$\mathcal{L}_{Dirac} = i\sum \overline{\psi}\gamma^\mu D_\mu \psi\,, \tag{1.3}$$

where the sum runs over all the chiral fermions ψ of the model. The gauge interactions of the matter fields are encoded in the covariant derivative

$$D_\mu = \partial_\mu + ig_s G^b_\mu \lambda_b + igW^a_\mu \sigma_a + ig'B_\mu Y\,, \tag{1.4}$$

where g_s, g and g' are the three gauge couplings of the groups $SU_C(3)$, $SU_L(2)$ and $U_Y(1)$, respectively, whereas λ_b and σ_a are the generators of $SU_C(3)$ and $SU_L(2)$, respectively. In particular, the Dirac Lagrangian contains the so-called neutral-current interactions (NC) mediated by the neutral vector bosons W^3_μ and the B_μ, and the so-called charged-current interactions (CC), which are instead mediated by the charged vector bosons W^1_μ and W^2_μ. The four vector bosons can be recast in the following linear combinations

$$W^\pm_\mu = \frac{W^1_\mu \mp iW^2_\mu}{\sqrt{2}}\,, \quad Z_\mu = \cos\theta_W W^3_\mu - \sin\theta_W B_\mu\,, \quad A_\mu = \sin\theta_W W^3_\mu + \cos\theta_W B_\mu\,, \tag{1.5}$$

where $W^\pm$ and Z_μ are the physical weak bosons, and A_μ is the electromagnetic potential field. The angle θ_W is the so-called *Weinberg's weak mixing angle*.

The second term in Eq. (1.2) encodes the interactions of the gauge vector boson fields. It takes the form

$$\mathcal{L}_{Gauge} = -\frac{1}{2}\mathrm{Tr}\left(G_{\mu\nu}G^{\mu\nu}\right) - \frac{1}{2}\mathrm{Tr}\left(W_{\mu\nu}W^{\mu\nu}\right) - \frac{1}{4}B_{\mu\nu}B^{\mu\nu}\,, \tag{1.6}$$

---

[2]For the sake of simplicity, here we omit the gauge-fixing terms and the ghost interactions.

where $G_{\mu\nu}$, $W_{\mu\nu}$ and $B_{\mu\nu}$ are the field strengths of $SU_C(3)$, $SU_L(2)$ and $U_Y(1)$, respectively.

The third term in Eq. (1.2) is the Higgs potential whose expression is given by

$$\mathcal{L}_{Higgs} = D_\mu H^\dagger D^\mu H - \mu^2 H^\dagger H - \lambda \left(H^\dagger H \right)^2 . \tag{1.7}$$

The coupling λ must be positive in order to have the Higgs potential bounded from below, whereas the coupling μ^2 is negative in order to have the spontaneous breaking of the electroweak symmetry. Indeed, under the prescription of $\mu^2 < 0$, the Higgs acquires a vacuum expectation value (*vev*) v_{SM} and breaks the group $SU_L(2) \otimes U_Y(1)$ down to the electromagnetic one $U_Q(1)$. Let us write the Higgs field as

$$H = \begin{pmatrix} H^+ \\ \frac{v_{SM}+h+iA}{\sqrt{2}} \end{pmatrix} . \tag{1.8}$$

After the electroweak symmetry breaking, the fields $H^\pm$ and A are identified with the three Nambu-Goldstone bosons corresponding to the broken generators of $SU_L(2) \otimes U_Y(1)$ [25, 26, 27]. The three broken degrees of freedom are absorbed by the three physical weak gauge bosons ($W^\pm$ and Z) which consequently acquire the masses [28]

$$M_W = \frac{g}{2}v_{SM} \approx 80.4\,\text{GeV}\,, \qquad M_Z = \frac{M_W}{\cos\theta_W} \approx 91.2\,\text{GeV}\,, \tag{1.9}$$

with $v_{SM} = 246$ GeV. The photon instead remains massless, as a consequence of the preserved residual $U_Q(1)$ symmetry. The field h is the recently discovered Higgs boson, whose mass M_h cannot be predicted by the theory but it has to be experimentally measured. The ATLAS [20] and the CMS [21] Collaborations have found that $M_h \approx 125$ GeV.

The last term in the SM Lagrangian concerns the Yukawa interactions through which fermions get mass and couple to the Higgs field. Its expression takes the form

$$\mathcal{L}_{Yukawa} = -\sum_{ij} \Gamma^\ell_{ij} \overline{L}_{iL} H \ell_{jR} - \sum_{ij} \Gamma^d_{ij} \overline{Q}_{iL} H d_{jR} - \sum_{ij} \Gamma^u_{ij} \overline{Q}_{iL} \tilde{H} u_{jR} + \text{h.c.}\,, \tag{1.10}$$

where the indexes i and j label the three generations and $\tilde{H} \equiv i\tau_2 H$ with τ_2 being the second Pauli matrix. The Yukawa couplings Γ are complex arbitrary non-diagonal 3×3 matrices. They can be diagonalized by means of bi-unitary transformations

$$\text{Y}^a = \mathcal{U}^{a\dagger}_L \Gamma^a \mathcal{U}^a_R = \text{diag}\left(y^a_1, y^a_2, y^a_3 \right)\,, \tag{1.11}$$

where $\mathcal{U}_L^a$ and $\mathcal{U}_R^a$ are two 3×3 unitary matrices and the eigenvalues y_i^a are real. Because neutrinos are massless in the SM, it is possible to consider Γ^ℓ to be diagonal without loss of generality by performing a simple redefinition of the leptonic fields. This implies that in the SM the leptonic flavor states coincide with the physical ones that have a definite mass. On the other hand, this is not the case for quarks since the Higgs field couple to both u- and d-quarks. This leads to a mismatch between the flavor and mass bases and consequently to a non-trivial mixing among the quarks. The mixing is encoded in the so-called Cabibbo-Kobayashi-Maskawa matrix (CKM) [29, 30]

$$\mathcal{U}_{CKM} = \mathcal{U}_L^{u\dagger} \mathcal{U}_R^d = \begin{pmatrix} 1 & 0 & 0 \\ 0 & c_{23} & s_{23} \\ 0 & -s_{23} & c_{23} \end{pmatrix} \begin{pmatrix} c_{13} & 0 & s_{13}e^{-i\delta} \\ 0 & 1 & 0 \\ -s_{13}e^{i\delta} & 0 & c_{13} \end{pmatrix} \begin{pmatrix} c_{12} & s_{12} & 0 \\ -s_{12} & c_{12} & 0 \\ 0 & 0 & 1 \end{pmatrix}, \tag{1.12}$$

with $s_{ij} = \sin\theta_{ij}$ and $c_{ij} = \cos\theta_{ij}$. The CKM matrix has therefore four free parameters: three angles and and a phase allowing for $\mathcal{CP}$ violation in the quark sector. The CKM parameters have been measured to be equal to [28]

$$\theta_{12} \approx 13°, \quad \theta_{23} \approx 2.4°, \quad \theta_{13} \approx 0.2°, \quad \delta \approx 59.7°. \tag{1.13}$$

The Yukawa terms also provide a mass to fermions after the electroweak symmetry breaking triggered by the Higgs field. Indeed, it is worth observing that mass terms for fermions cannot be explicitly written because they are not gauge invariant. The masses emerge from the *vev* acquired by the Higgs field. For instance, for the electron we have

$$m_e = \mathrm{Y^e}_{11} \langle H \rangle = \frac{1}{\sqrt{2}} y_1^e v_{SM} \approx 0.511 \,\mathrm{MeV}. \tag{1.14}$$

Lastly, we note that the full SM Lagrangian depends only on 19 unconstrained parameters: 3 gauge couplings, the Higgs quadratic mass coefficient and self-coupling, 9 quark and lepton masses, 4 parameters of the CKM matrix, and 1 more parameter related to the strong $\mathcal{CP}$ problem affecting the quantum chromodynamics Lagrangian.

1.2   Beyond the Standard Model

It is hard to believe that the Standard Model is the last step toward the understanding of nature. There are indeed conceptual theoretical problems in the SM, that deserve some explanation. Examples of such theoretical problems are the separation of very different energy scales in a field theory with scalars (*hierarchy problem*), the hint of an unification of the three gauge couplings for extreme large energy, the particular structure of fermion masses, the need to provide a quantum description of the gravitational force, etc. More-over, the SM cannot account for fundamental physical phenomena like the neutrino masses and oscillations, the existence of dark matter and dark energy, and the matter-antimatter asymmetry of the Universe. All these aspects, which are referred to as physics Beyond the SM (BSM), show us the need of new theoretical developments.

Among the conceptual theoretical problems, the hierarchy problem is the large discrepancy between aspects of the weak force and gravity. Within the SM, the question is why the Higgs boson is so much lighter than the Planck mass ($M_{\mathrm{Pl}} \sim 10^{19}\,\mathrm{GeV}$) at which gravitational effects cannot no longer be neglected. The problem is that M_h^2 receives enormous quantum corrections from the virtual effects of every particle that couples, directly or indirectly, to the Higgs field. For example, the one loop correction to the Higgs mass is proportional to the squared of ultraviolet momentum cut-off Λ, used to regulate the loop integral ($\Delta M_h^2 \propto \Lambda^2$). Since the cut-off Λ is the energy at which new physics enters to alter the high-energy behavior of the theory, it is at least of order of the Planck mass. Therefore, these corrections are much larger than the Higgs mass: quantum corrections to M_h^2 are some 30 orders of magnitude larger that the required value of M_h^2 which is about $(125\,\mathrm{GeV})^2$. This means that the bare mass parameter of the SM Higgs must be fine-tuned in such a way that it almost completely cancels the quantum corrections. This level of fine-tuning is not in agreement with the principle of naturalness.

According to the SM, neutrinos are massless particles. However, several experiments have observed the neutrino oscillations that can be only originated by non-zero neutrino mixing and masses. Moreover, still there are no experimental observations indicating the nature of neutrinos: since they are neutral particles, neutrinos can be either Dirac or

Majorana particles.

Astrophysical and cosmological observations, such as the measurements of the Cosmic Microwave Background (CMB), the galactic rotation curves, galaxy clusters, gravitational lensing and especially bullet clusters, tell us the SM explains only the 5 % of the energy present in the Universe. About 25 % should be dark matter, a kind of matter hypothesized to account for gravitational effects that appear to be the result of invisible mass. The rest should be dark energy, an almost constant energy density for the vacuum which tends to accelerate the expansion of the Universe.

Lastly, the SM does not explain why the Universe is made out of mostly matter. It predicts that matter and antimatter should have been created in almost equal amounts if the initial conditions of the universe did not involve disproportionate matter relative to antimatter. Therefore, no mechanism sufficient to explain this matter–antimatter asymmetry exists in the framework of SM.

Several extensions of the SM have been proposed in the last decades to account for one or more of these problems. Among them we remind the Grand Unified Theories [31, 32, 33, 34, 35], based on the idea that at high-energy scale all the forces have the same magnitude (gauge coupling unification), extra-dimensions [36, 37], the idea of supersymmetry [7, 38, 39, 40, 41] and of baryogenesis through leptogenesis [42]. Regarding supersymmetry, the non-observation of new particles at the electroweak scale leads to the so-called *little hierarchy problem*. Indeed, a small fine-tuning would be still required if supersymmetry is broken at an energy scale larger than TeV. In particular, as shown in Ref. [7], this is the case if one consider that the assumption of a one-step unification for the three gauge couplings naturally provides supersymmetric particles to have a mass as large as about 20 TeV. Such a scale is well above the energy to be reached in the final phase of the LHC accelerator.

Due to its relevance in this thesis, we devote the next Section to provide an overview of the neutrino physics, while the dark matter problem is introduced and described in detail in the next Chapter.

1.3 Neutrino Physics

Since their existence was first proposed by W. Pauli in 1930, neutrinos have fascinated theorists and experimentalists. After huge experimental efforts, we have acquired great knowledge about these particles. In particular, we know that neutrinos change their flavor during the propagation, and that at least two of them have a non-zero mass. The mass splittings and oscillations parameters are now measured with great accuracy. The paramount importance of the discovery of neutrino oscillations was recognized by the Nobel Prize in Physics that in 2015 was given to T. Kajita and A.B. McDonald, since the observation of neutrino oscillations is the proof that neutrinos are massive.

Neutrinos and antineutrinos are produced in a given flavor state $(\nu_e, \nu_\mu, \nu_\tau)$ in charged-current or neutral-current interactions. However, neutrino flavor states are superposition combinations of different mass eigenstates that represent the physical neutrinos. As in case of quarks, the neutrino oscillations are related to the mismatch between the flavor and the mass bases. Similarly to the CKM matrix, such a mismatch is encoded in the so-called Pontecorvo-Maki-Nakagawa-Sakata (PNSM) matrix [43, 44, 45, 46] that can be parametrized as[3]

$$
\mathcal{U}_{PNMS} = \mathcal{U}_L^{\ell\dagger} \mathcal{U}_R^\nu = \begin{pmatrix} 1 & 0 & 0 \\ 0 & c_{23} & s_{23} \\ 0 & -s_{23} & c_{23} \end{pmatrix} \begin{pmatrix} c_{13} & 0 & s_{13}e^{-i\delta} \\ 0 & 1 & 0 \\ -s_{13}e^{i\delta} & 0 & c_{13} \end{pmatrix} \begin{pmatrix} c_{12} & s_{12} & 0 \\ -s_{12} & c_{12} & 0 \\ 0 & 0 & 1 \end{pmatrix} \mathcal{T},
$$

(1.15)

with $s_{ij} = \sin\theta_{ij}$ and $c_{ij} = \cos\theta_{ij}$. According to how they are measured, the angles θ_{13}, θ_{23} and θ_{12} are defined as reactor, atmospheric and solar angles, respectively. The angle δ is the Dirac phase that accounts for the $\mathcal{CP}$ violation in the leptonic sector. Differently from the CKM, the PNMS matrix also contains two additional phases encoded in

$$
\mathcal{T} = \text{diag}\left(1, e^{i\alpha}, e^{i\beta}\right).
$$

(1.16)

The angles α and β are the Majorana phases. Indeed, since neutrinos are neutral particles, they can be Dirac or Majorana particles. In the latter case, two additional phases (α and

---

[3]Note that there exist other parametrizations for the lepton mixing matrix like for example the symmetrical ones [47].

β) cannot be absorbed by a redefinition of the neutrino fields and have to be taken into account.

The angles appearing in the PNMS matrix have been measured by several experiments. In particular, one has to remind the following observations

- disappearance of solar ν_e [48]: Kamiokande [49], SAGE [50], GALLEX [51, 52], GNO [53], Super-Kamiokande [54] and SNO [55, 56] Collaborations;

- disappearance of reactor $\overline{\nu}_e$: KamLAND Collaboration [57, 58], Double Chooz [59], Daya Bay [60, 61, 62] and RENO [63] Collaborations;

- disappearance of $\nu_\mu/\overline{\nu}_\mu$: Super-Kamiokande [64, 65], K2K [66], MINOS [67, 68, 69] and T2K [70, 71] Collaborations;

- $\nu_\mu \to \nu_e$ oscillations: T2K [72, 73], MINOS [74] and Double Chooz [75] Collaborations;

- remarkably, the first constraints to Dirac phase δ by the T2K Collaboration [76].

Hence, the fundamental parameters describing the neutrino physics are three angles, three phases (1 Dirac and 2 Majorana phases), and three masses m_1, m_2 and m_3. However, neutrino oscillations only depend on the neutrino mass squared differences $\Delta m_{ij}^2 = m_i^2 - m_j^2$. Indeed, one can show that the probability of the oscillation for a neutrino of flavor α with momentum $\overrightarrow{p}$ into a neutrino of flavor β, during its propagation of a source-detector distance L, is given by

$$P_{\nu_\alpha \to \nu_\beta} = \sum_{k=1}^{3} |\mathcal{U}_{\alpha k}|^2 \, |\mathcal{U}_{\beta k}|^2 + 2\mathrm{Re}\left[\sum_{j>k} \mathcal{U}_{\alpha k}^* \mathcal{U}_{\beta k} \mathcal{U}_{\alpha j} \mathcal{U}_{\beta j}^* \exp\left(-i\frac{\Delta m_{kj}^2}{2\,|\overrightarrow{p}|}L\right)\right]. \qquad (1.17)$$

Hence, oscillation experiments can only measure the differences $|\Delta m_{12}^2|$ (solar) and $|\Delta m_{13}^2|$, while they are not sensitive to the neutrino absolute mass scale. Under the convention that $m_1 < m_2$ ($\Delta m_{12}^2 < 0$), there exist two possibilities:

- **Normal Ordering (NO)** $m_1 < m_2 < m_3$;

- **Inverted Ordering (IO)** $m_3 < m_1 < m_2$.

The neutrino absolute mass scale could be instead measured by experiments analyzing beta decays and neutrinoless double beta decays. The former corresponds to the measurement of the spectrum of the electrons in the beta decay of tritium atoms, while the latter aims to observe a double beta decay without the emission of neutrinos, i.e. without missing energy. The observation of neutrinoless double beta decay is of paramount importance since it would eventually demonstrate the Majorana nature of neutrinos [77].[4] The most stringent upper bounds coming from beta decay experiments are $m_{\bar{\nu}_e} < 2.05$ eV and $m_{\bar{\nu}_e} < 2.3$ eV at 95% C.L. obtained by the Troitzk [78] and Mainz [79] experiments, respectively. On the other hand, the non-observation of the neutrinoless double beta decay in the phase 1 of the GERDA experiment provides the constraint $\langle m_{ee} \rangle < 0.2$ eV at 90% C.L. [80], where the quantity $\langle m_{ee} \rangle$ is a combination of neutrino masses and elements of the PNMS matrix. Other experiments looking for neutrinoless double beta decay are CUORE [81], EXO-200 [82], KamLAND-Zen [83] and NEMO-3 [84]. In addition to such laboratory experiments, cosmological observations also provide upper bounds on the sum of stable neutrinos. In particular, the recent analysis performed by the Planck Collaboration gives the cosmological bound $\sum m_\nu < 0.17$ eV [85].

The known properties of neutrinos are reported in Tab. 1.3. They are obtained by performing a global fit of the available experiment data [86] (other global fits are provided in Ref.s [87, 88]).

$$\delta m^2 = \Delta m_{21}^2 = m_2^2 - m_1^2, \quad \text{and} \quad \Delta m^2 = m_3^2 - \frac{m_1^2 + m_2^2}{2}. \tag{1.18}$$

---

[4]The detection of the neutrinoless double beta decay would constrain and provide important information on the possible extensions of the Standard Model as shown in Ref. [8].

Parameter	Hierarchy	Best-Fit	1σ range	3σ range
$\delta m^2/10^{-5}\,\mathrm{eV}^2$	NO or IO	7.37	$7.12 - 7.54$	$6.93 - 7.96$
$\sin^2\theta_{12}/10^{-1}$	NO or IO	2.97	$2.81 - 3.14$	$2.50 - 3.54$
$\left|\Delta m^2\right|/10^{-3}\,\mathrm{eV}^2$	NO	2.525	$2.495 - 2.567$	$2.411 - 2.646$
	IO	2.505	$2.473 - 2.539$	$2.390 - 2.624$
$\sin^2\theta_{13}/10^{-2}$	NO	2.15	$2.08 - 2.22$	$1.90 - 2.40$
	IO	2.16	$2.07 - 2.24$	$1.90 - 2.24$
$\sin^2\theta_{23}/10^{-1}$	NO	4.25	$4.10 - 4.46$	$3.81 - 6.15$
	IO	5.89	$4.17 - 4.48 \oplus 5.67 - 6.05$	$3.84 - 6.36$
δ/π	NO	1.38	$1.18 - 1.61$	$0 - 0.17 \oplus 0.76 - 2$
	IO	1.31	$1.12 - 1.62$	$0 - 0.15 \oplus 0.69 - 2$

Table 1.3: Neutrino oscillation parameters of the global 3ν analysis provided in Ref. [86]. Here, the two mass squared differences are defined as $\delta m^2 = \Delta m^2_{21} = m_2^2 - m_1^2$ and $\Delta m^2 = m_3^2 - \frac{m_1^2 + m_2^2}{2}$.

Chapter 2

The Quest for Dark Matter

The first evidence of the existence of Dark Matter (DM) dates back to 1933 when Fritz Zwicky studied the gravitational anomalies in the Coma cluster of galaxies [89, 90]. By using the virial theorem, he found that a hidden mass not emitting light was required to account for the very large dispersion velocities of some galaxies in the Coma cluster. In particular, the ratio (*mass-to-light* ratio) between this hidden matter and the directly visible one was estimated to be roughly 500 to 1. F. Zwicky dubbed such a kind of invisible mass as *dark matter*, following the definition of astrophysical dark bodies provided by H. Poincaré in 1906. The Zwicky's studies was largely overlooked until the 1970, when Vera Rubin and Kent Ford analyzed the rotation curves of the spiral galaxies, providing a very strong evidence for the existence of dark matter [91].

We know that dark matter fills the Universe, plays a fundamental role during the structure formation, and explains the discrepancy between visible and dynamical astronomical observations. However, after more than 80 years from the Zwicky's observations, the nature of dark matter still remains an open question. The Standard Model, whose success was once again confirmed by the discovery of the Higgs boson at LHC, only describes the 5% of the energy content of the Universe, consisting of stars, dust, galaxies, clusters of galaxies and black holes only. The remaining 95% is given by dark matter and dark energy, whose nature is completely unknown. Several theoretical frameworks allocating viable DM candidates have been proposed in literature. DM mass is spread over many orders of magnitude:

from about 10^{-32} GeV up to 10^{18} GeV, e.g. axions (10^{-6}–10^{-3} eV), keV sterile neutrinos, WIMPzilla ($\sim 10^{12}$ GeV). Among the interesting schemes provided by elementary particle physics, one of the most attractive and simplest scenario regards the Weakly Interacting Massive Particle (WIMP) paradigm that typically predicts a DM mass in the GeV–TeV range and interaction rates of the order of weak interactions. However, up to now almost all indirect, direct and collider searches have not provided any clear evidence of dark matter [28]. Hence, DM observations remain linked to their indirect gravitational footprint only.

The Chapter, based on Ref.s [92, 93, 94], is organized as follows. In the first Section, we discuss all the evidence suggesting the existence of dark matter and, consequently, its properties. In the second Section we describe how DM particles are generally produced in the early Universe, paying particular attention to the freeze-out production mechanism. In third Section we report a list of interesting DM candidate, while in the last Section we provide a review of all DM searches.

2.1   Evidences and properties

There exists a wide variety of astrophysical and cosmological observations that supports the existence of dark matter. These observations range from galactic scales up to cosmological ones. At galactic scales, the most convincing and direct evidence comes from the measurements of circular velocities of stars and gas, i.e. the rotation curves. Indeed, according to the Newtonian dynamics, one would expect a radial velocity decreasing with the distance from the galactic center. The flatness of the rotation curves at large radii can be explained by considering an invisible matter spherically distributed in the outer parts of the galaxy. Moreover, one has also to remind the weak [95] and strong gravitational lensing [96, 97]. At larger astronomical scales, the observations of the dispersion velocities of individual stars in cluster of galaxies also provide the indication of a mass-to-light ratio significantly different from the unity. The collision of two clusters of galaxies, the so-called *bullet clusters*, gives the strongest evidence that the mass distribution of clusters is dominated by dark matter [98]. At cosmological scales, the presence of dark matter is required during the

epochs of recombination and the structures formation. Furthermore, the analysis of CMB temperature anisotropies leads to the determination of the matter content (baryons and dark matter) of the Universe [85].

All the evidence for dark matter is related to gravitational "anomalies". In 1983, M. Milgrom proposed a phenomenological model known as modified Newtonian dynamics (MOND) in order to account for the observed galactic rotation curves without dark matter [99]. In such a model, the Newton's second law is modified at very small accelerations as $F = ma^2/a_0$ with a_0 being a constant. However, MOND and its relativistic formulation known as Tensor-Vector-Scalar gravity fail in explaining all the observations previously discussed, in particular the ones related to cluster and cosmological scales. Hence, the introduction of dark matter is the only way to explain all the gravitational anomalies related to systems of different sizes and epochs.

Even thought the nature of dark matter is still unknown, the various astronomical and cosmological observations provide us some properties that a viable DM candidate has to have. In particular, an acceptable DM candidate should be:

- **Neutral**. Very strong limits on the electric charge of dark matter are placed by searches for heavy Hydrogen-like atoms and by limits on strongly interacting DM [100, 101, 102]. In particular, for a DM mass m_{DM} smaller than the electron mass, the DM electric charge q_{DM} could be as large as 10^{-15} [103]. For larger masses, the allowed range is instead $q_{DM} \lesssim 10^{-7} \, (m_{DM}/\mathrm{GeV})$ [104].

- **Stable**. Since we observe some of the gravitational anomalies today, DM particles have to be stable or very long lived. The lifetime τ_{DM} has to be at least larger than the age of Universe, i.e. $\tau_{DM} \geq 10^{17}$ sec. However, observations of cosmic-rays, gamma-rays and neutrinos provide stronger constraints that in general lead to $\tau_{DM} \geq 10^{26}$ sec [105, 106, 107, 108].

- **Cold**. The N-body simulations describe the observed structure in the Universe [109] when dark matter is cold [110, 111], that means it was non-relativistic during the epoch of formation of galaxies ($T \approx 1$ eV). The galaxies have been formed by primordial density fluctuations that at small scales are washed out by the random thermal

motion of DM particles. Hence, hot (relativistic) DM particles suppress the growth of small scale structures. Warm DM particles yield also a good fit predicting the right amount of satellite galaxies for the Milky Way [112, 113].

- **Consistent with Big Bang Nucleosynthesis (BBN)**. BBN [114] is the epoch during which the light elements are produced. Since it occurs at $T \sim$ MeV, DM masses of the order of MeV energy are strongly constrained in order to not spoil the right abundances of Hydrogen, Helium and other elements.

- **Collisionless**. In frameworks where DM particles interact with themselves [115], the self-interaction has to be not too strong ($\sigma/m_{\mathrm{DM}} \lesssim 0.3\,\mathrm{cm}^2\,\mathrm{g}^{-1}$) otherwise the galactic halos would quickly evaporate [116].

- **Right DM abundance**. The model allocating the DM candidate has to account also for its production providing the observed abundance

$$\Omega_{\mathrm{DM}} h^2\big|_{\mathrm{obs}} = 0.1188 \pm 0.0010\,, \tag{2.1}$$

according to the Planck analysis [85].

Moreover, the DM candidate has to be compatible with all the exclusion limits placed by DM searches experiments. Such limits will be discussed in the last Section of this Chapter. In the next Section, instead, it is briefly reviewed the standard mechanism through which DM particles are in general produced in the early Universe: the *thermal freeze-out*.

2.2   Production mechanisms: the thermal freeze-out

According to the theoretical paradigm of the evolution of the Universe in standard cosmology, the Universe began from an isotropic and quasi-homogeneous hot plasma some fifteen billion years ago, and then it cooled down due to its rapid expansion. During the history of the Universe, DM particles are in general produced through their interactions with particles of the hot plasma. In order to provide an acceptable DM candidate, one has to address the question "how is dark matter produced in the early Universe?". In general, it is

possible to divide the production mechanisms in two categories: thermal and non-thermal. Among the non-thermal mechanisms, we remind the *freeze-in* mechanism [117, 118], the direct production from inflaton decay or from coherent oscillations [119]. Such production mechanisms are usually model-dependent and fine-tuned to reproduced the correct relic abundance reported in Eq. (2.1). On the other hand, the *thermal freeze-out* production mechanism provides a simple, calculable, and almost model-independent way to create DM particles from thermal processes with the hot plasma [120, 121, 122]. Let us now briefly describe the history of DM particles, focusing on the freeze-out mechanism.

The evolution of the number density n_χ of DM particles (hereafter denoted as χ) with mass m_χ during the history of the Universe is encoded into the Boltzmann equation. It is possible to cast the Boltzmann equation in terms of the yield

$$Y_\chi \equiv \frac{n_\chi}{\mathfrak{s}} , \tag{2.2}$$

where $\mathfrak{s}$ is the entropy density whose expression as a function of the temperature T of the thermal plasma is equal to

$$\mathfrak{s} = \frac{2\pi^2}{45} g_*^{\mathfrak{s}} (T) \, T^3 . \tag{2.3}$$

Here, $g_*^{\mathfrak{s}} (T)$ is the sum of the relativistic bosonic (B) and fermionic (F) degrees of freedom g_i weighted by the temperatures of each species in the plasma.

$$g_*^{\mathfrak{s}} (T) = \sum_B g_B \left(\frac{T_B}{T} \right)^3 + \frac{7}{8} \sum_F g_F \left(\frac{T_F}{T} \right)^3 . \tag{2.4}$$

The Boltzmann equation for the yield Y_χ reads

$$\frac{dY_\chi}{dT} = -\frac{1}{\mathcal{H} \, T \, \mathfrak{s}} \left[\frac{g_\chi}{(2\pi)^3} \int \mathcal{C} \, \frac{d^3 p_\chi}{E_\chi} \right] , \tag{2.5}$$

where the quantity in brackets contains a general collision term $\mathcal{C}$ related to the interactions of DM particles with SM ones, and $\mathcal{H}$ is the Hubble parameter defined as

$$\mathcal{H} = 1.66 \sqrt{g_* (T)} \frac{T^2}{M_{\mathrm{Pl}}} , \tag{2.6}$$

where M_{Pl} is the Planck mass and $g_* (T)$ is given by

$$g_* (T) = \sum_B g_B \left(\frac{T_B}{T} \right)^4 + \frac{7}{8} \sum_F g_F \left(\frac{T_F}{T} \right)^4 . \tag{2.7}$$

The Boltzmann equation (2.5) has been obtained by assuming that the relativistic degrees of freedom of the thermal bath do not change with decreasing of the temperature, i.e.,

$$\frac{dg_*}{dT} = \frac{dg_*^{\mathfrak{s}}}{dT} = 0 \,. \tag{2.8}$$

This implies that $\dot{T} \approx \mathcal{H}T$. Such an approximation holds in different settings frequently studied. At temperatures higher than the electroweak scale, we have $g_* = g_*^{\mathfrak{s}} = 106.75$. Such a value corresponds to the total number of relativistic degrees of freedom in the SM at high temperature.

The Boltzmann equation (2.5) describes how the yield Y_χ changes as a function of the temperature T. By integrating this equation over the temperature, or over the auxiliary variable $x \equiv m_\chi/T$, one obtains the DM relic abundance

$$\Omega_{\rm DM}h^2 = \frac{2m_\chi \mathfrak{s}_0}{\rho_{\rm crit}/h^2} \left[m_\chi \int_0^\infty dx \frac{1}{x^2} \left(-\frac{dY_\chi}{dT}\bigg|_{T=\frac{m_\chi}{x}} \right) \right] , \tag{2.9}$$

where $\mathfrak{s}_0 = 2891.2\,{\rm cm}^{-3}$ is today's entropy density and $\rho_{\rm crit}/h^2 = 1.054 \times 10^{-5}\,{\rm GeV\,cm}^{-3}$ is the critical density [28]. In the above expression, the factor 2 accounts for the contribution of DM antiparticles to the relic abundance in case of Dirac particles.

As an illustrative example, let us now obtain the collision term in case of scenario where DM particles interact with SM fields ψ through an unidentified process $\chi\overline{\chi} \leftrightarrow \psi\overline{\psi}$ with cross section $\sigma_{\chi\overline{\chi}}$. If the particles ψ are in thermal equilibrium with the plasma, one can show that the Boltzmann equation (2.5) becomes equal to

$$\frac{dY_\chi}{dT} = -\frac{\langle \sigma_{\chi\overline{\chi}}|v|\rangle\,\mathfrak{s}}{\mathcal{H}\,T} \left(Y_\chi^2 - Y_{\chi,{\rm eq}}^2 \right) , \tag{2.10}$$

where $\langle \sigma_{\chi\overline{\chi}}|v|\rangle$ is the thermally averaged cross section of $\chi\overline{\chi}$ annihilation. The quantity $Y_{\chi,{\rm eq}}$ is the yield when the thermal equilibrium holds. It can be obtained by considering the expressions

$$n_{\chi,{\rm eq}} = \begin{cases} g_\chi \frac{\xi}{\pi^2} T^3 & \text{relativistic particles} \\ \\ g_\chi \left(\frac{m_\chi T}{2\pi^2} \right)^{3/2} e^{-m_\chi/T} & \text{non-relativistic particles} \end{cases} , \tag{2.11}$$

where g_χ is the number of internal degrees of freedom of DM particles. At high temperatures $T \gg m_\chi$ the processes of creation and annihilation are strong enough to maintain

the DM particles in thermal equilibrium. Hence, in this regimes (relativistic particles) $n_\chi = n_{\chi,\text{eq}} \propto T^3$. As the temperature falls below the DM mass, the processes of creation become exponentially suppressed while the annihilation should in principle continue. In this case, the number density of DM particles would be exponentially suppressed (non-relativistic regime) and DM particles would quickly disappear from the plasma. However, if the expansion of the Universe, that is encoded by the Hubble parameter $\mathcal{H}$, dominates over the annihilation rate, it becomes increasingly hard for DM particles to find each other to annihilate. Hence, the number density n_χ *freeze-out*. The condition of freeze-out is simply expressed by the equality

$$\mathcal{H} \sim \langle \sigma_{\chi\bar{\chi}} |v| \rangle \, n_{\chi,\text{eq}} \, , \tag{2.12}$$

that means the expansion rate is comparable to the annihilation rate. The exact temperature of freeze-out (T_{FO} or alternatively x_{FO}) can be obtained by solving the Boltzmann equation numerically. However, it is approximately given by the following analytical expression

$$x_{\text{FO}} = \frac{m_\chi}{T_{\text{FO}}} \approx \ln \left[c \, (c+2) \, \sqrt{\frac{45}{8}} \frac{g_\chi}{2\pi^3} \frac{m_\chi M_{\text{Pl}} \, (a + 6b/x_{\text{FO}})}{g_*^{1/2} x_{\text{FO}}^{1/2}} \right] \, , \tag{2.13}$$

where $c \approx 0.5$ and the coefficients a and b are related to the s- and p-wave terms in the expansion

$$\langle \sigma_{\chi\bar{\chi}} |v| \rangle = a + b \, \langle v \rangle + \mathcal{O}\left(v^4\right) \, . \tag{2.14}$$

Then, the DM relic density is approximately given by

$$\Omega_{\text{DM}} h^2 \approx \frac{1.04 \times 10^9 \, \text{GeV}^{-1}}{M_{\text{Pl}}} \frac{x_{\text{FO}}}{g_*^{1/2} \, (a + 3b/x_{\text{FO}})} \, . \tag{2.15}$$

2.3   Dark Matter candidates

Here, we provide a brief discussion about some of the most popular and well motivated candidates belonging to the so-called dark matter *zoo*.

Neutrinos were the first particles to be proposed as DM candidates. However, they are not a viable candidates since do not satisfy all the properties listed in the Section 2.1.

Indeed, one can show that the total neutrino relic density is given by

$$\Omega_\nu h^2 = \sum_{i=1}^{3} \frac{m_i}{93\,\text{eV}}\,. \tag{2.16}$$

By considering the limit on the absolute neutrino masses placed by Troitzk [78] and Mainz [79] experiments for all the three mass eigenvalues, one obtains that neutrinos cannot account for the whole DM abundance since $\Omega_\nu h^2 \lesssim 0.07$. Moreover, neutrinos are relativistic (hot) at their decoupling occurring at $T \sim \text{MeV}$, and hence they are incompatible with the N-body simulations for structure formation.

Axions were originally introduced to solve the so-called strong $\mathcal{CP}$ problem related to the fine-tuning of the $\mathcal{CP}$-violating coupling $\theta\,G_{\mu\nu}^a \tilde{G}^{\mu\nu a}$ [123, 124, 125, 126]. Indeed, such a coupling has to be smaller than 10^{-9} according to the measurement of the neutron electric dipole moment. The fine-tuned problem is solved by the Peccei-Quinn $U(1)$ symmetry that is dynamically and spontaneously broken. The axion is the pseudo-Goldstone boson associated to this symmetry. These particles are stable and cold (non-relativistic at production), and have a mass equal to [127, 128, 129]

$$m_a \approx 6 \times 10^{-6} \left(\frac{10^{12}\,\text{GeV}}{f_a}\right)\,\text{eV}\,, \tag{2.17}$$

where f_a is the axion decay constant that ranges from 10^9 to 10^{12} GeV.

Sterile neutrinos are simply right-handed neutrinos ν_R, that are singlet under the SM gauge group [130]. They interacts only through their mixing with the left-handed neutrinos ν_L belonging to the $SU_L(2)$ lepton doubles. By adding ν_R to the SM matter content, one can write two neutrino mass terms

$$\mathcal{L} \supset \frac{m_D}{\langle H \rangle} \overline{L} \tilde{H} \nu_R + \frac{1}{2} m_S \left(\overline{\nu}_R \nu_R^c\right) + \text{h.c.}\,, \tag{2.18}$$

where the former is a Dirac mass Yukawa-like term while the latter provides a Majorana mass. For the sake of simplicity, in the expression we omit the flavor indexes and we consider just one left-handed and one right-handed neutrinos. After the electroweak symmetry breaking, the full neutrino mass term becomes equal to

$$\mathcal{L} \supset \frac{1}{2} \left(\overline{\nu}_L\, \overline{\nu^c}_R\right) \mathfrak{M} \begin{pmatrix} \nu_L^c \\ \nu_R \end{pmatrix} + \text{h.c.} = \frac{1}{2} \left(\overline{\nu}_L\, \overline{\nu^c}_R\right) \begin{pmatrix} 0 & m_D \\ m_D^T & m_S \end{pmatrix} \begin{pmatrix} \nu_L^c \\ \nu_R \end{pmatrix} + \text{h.c.}\,. \tag{2.19}$$

In the limit $m_S \gg m_D$, the two eigenstates obtained by diagonalizing the matrix $\mathfrak{M}$ have the following masses

$$|m_1| \sim \frac{m_D^2}{m_S}, \qquad \text{and} \qquad m_2 \sim m_S. \qquad (2.20)$$

Hence, one eigenstate is a light mainly-active neutrino while the other one is a heavier mainly-sterile state. This is the so-called *type-I seesaw mechanism* [131, 132, 133, 134, 135, 136]. The mixing between the two states is provided by the active-sterile mixing angle given by

$$|\theta| \sim \frac{m_D}{m_S} \sim \sqrt{\frac{m_1}{m_2}} \sim 3 \times 10^{-3} \left(\frac{m_1}{0.05 \, \text{eV}} \right)^{1/2} \left(\frac{6 \, \text{keV}}{m_2} \right)^{1/2}. \qquad (2.21)$$

A viable DM candidate is a sterile neutrino with mass m_2 in the keV range. Such a particle could be cold or warm depending on how it is produced in the early Universe. The most simple production mechanism know as Dodelson-Widrow mechanism is through the oscillations between active and sterile neutrinos [137]. The keV neutrinos are not stable, but decay into a light neutrino and a X-ray photon. Even though there exist stringent astrophysical and cosmological constraints on keV sterile neutrinos, such particles can explain the observation of the 3.5 keV X-ray line [138, 139]. In this framework, the most simple model accounting for dark matter, for the light neutrino masses with the seesaw mechanism and for the baryon asymmetry through leptogenesis is the neutrino minimal standard model (νMSM) [140]. Such a model contains only three sterile neutrinos up to the Planck scale in addition to the SM particles. One of them is at the keV scale and is a viable DM candidate, while the other two have a mass in the range 100 MeV – 100 GeV.

Weakly-interacting massive particles (WIMPs) represent a class of DM candidates that typically have a mass in the GeV–TeV range and have interactions of the same order of the weak ones with SM particles. The WIMP paradigm is the most attractive scenario of dark matter for different reasons:

- WIMP candidates naturally appear in several extensions of the SM. In particular, in supersymmetric theories the lightest supersymmetric particle is a good DM candidate with the WIMPs properties. Possible DM candidates are for instance neutralinos, gauginos or sneutrinos.

- WIMPs are cold, non-relativistic at freeze-out.

- Independently from the initial conditions of the Universe, the correct relic abundance is obtained through the thermal *freeze-out* mechanism once weak scale interactions between SM and DM particles are assumed.

The remarkable coincidence between the annihilation cross section providing the correct DM relic abundance and the typical cross section of weak scale interactions is quoted in literature as the *WIMP miracle*. Indeed, in case of a DM mass in the GeV–TeV range and of an annihilation cross section around the weak scale, we have that the freeze-out occurs at $x_{\rm FO} \approx 17 \div 25$. Hence, by using Eq. (2.15), the resulting relic abundance is

$$
\begin{aligned}
\Omega_{\rm DM} h^2 &\approx 0.1 \left(\frac{x_{\rm FO}}{20}\right) \left(\frac{g_*}{80}\right)^{-1/2} \left(\frac{a + 3b/x_{\rm FO}}{3 \times 10^{-26} {\rm cm}^3\,{\rm s}^{-1}}\right)^{-1} \\
&\approx 0.1 \frac{3 \times 10^{-26} {\rm cm}^3\,{\rm s}^{-1}}{\langle \sigma_{\chi\overline{\chi}} |v| \rangle} \,.
\end{aligned}
\tag{2.22}
$$

The correct DM relic abundance is threfore obtained when a typical cross section of a weak-scale interaction $\alpha^2/(100\,{\rm GeV})^2$ is considered, providing the so-called WIMP miracle.

2.4 Dark Matter searches

DM particle can be searched for in laboratories through recoil off nuclei (N) via processes like $\chi N \to \chi N$ (*direct detection*), in the sky by detecting their annihilation or decay byproducts (*indirect detection*), and with colliders such as LHC in processes like $p\overline{p} \to \chi\overline{\chi}X$, being X any SM particles (*collider searches*). In Fig. 2.1 they are reported the model-independent interactions of WIMPs on which direct, indirect and colliders searches are based. The same interactions are also relevant in different epochs of the history of the Universe like the DM production and the structure formation.

2.4.1 Direct searches

Our galaxy is surrounded by a DM halo that extends far beyond the radius of baryonic matter. Galactic rotation curves and cosmological simulations provides an estimate for the DM local density (at a distance of ~ 8.5 kpc from the Galactic Center). In particular, we
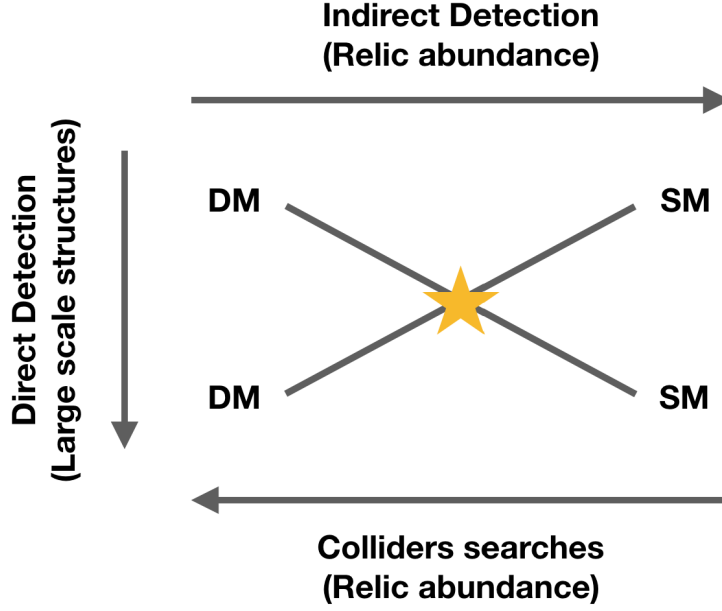
Figure 2.1: Scheme of WIMP interactions in the early Universe and the three ways of detections.

have [141]

$$\rho_\odot = (0.39 \pm 0.03)\,\text{GeV}\,\text{cm}^{-3}\,. \tag{2.23}$$

Due to the motion of the Sun and the Earth, we are crossed by a flux of dark matter particles that move with an averaged relative velocity of $v_0 \approx 300$ km/s. These dark matter particles can scatter off a nucleus in an underground detector. The idea to infer the DM properties by measuring the recoil energy E_R of the nucleus dates back to 1985 by Goodman and Witter [142]. From the kinematics, the recoil energy has the following expression

$$E_R \simeq 50\,\text{keV} \left(\frac{m_\chi}{100\,\text{GeV}}\right)^2 \left(\frac{100\,\text{GeV}}{m_N}\right)\,, \tag{2.24}$$

where m_N is the mass of the target nuclei. The experiments dedicated for DM direct searches are in general sensitive to DM masses m_χ larger than ~ 10 GeV, according to the threshold energy of few keVs for a positive signal in the detector and to a target nuclei mass of ~ 100 GeV (for instance, experiments like XENON100 and LUX we have $m_N^{\text{Xe}} \simeq 120$ GeV, i.e. the mass of Xenon nuclei). Therefore, direct DM searches in underground detectors represent the most promising way to look for WIMP candidates. A list of selected dark

matter experiments is provided in Tab. 2.1. All these experiments provide excluded regions in the plane defined by the WIMP mass and WIMP-nucleon cross section. The status of WIMP direct detection results is summarized in Fig. 2.2. We note that:

- the bounds become weaker for masses $m_\chi \lesssim 10$ GeV due to the energy thresholds of the experiments;

- independently from the experiment, the maximum sensitivity is in general reached for a DM mass of 50–100 GeV;

- the sensitivity weakens towards larger DM mass because the DM number density of the Galaxy scales as $1/m_\chi$.

By the year 2020, direct detection experiments are expected to have a sensitivity $\approx 10^{-48} \, \text{cm}^2$, i.e. close to the so-called "*neutrino floor*". There, coherent neutrinos scatterings become relevant and the direct detection experiments are no longer background free.

One has to highlight the statistical significant positive signal of DM direct detection claimed by the DAMA Collaboration, which observed an annual modulation of the event rate as expected by taking into account the relative motion of the Earth around the Sun [146]. The DAMA data can be interpreted in terms of dark matter interactions with nuclei, but such a scenario is in tension with the null results reported by other experiments [147, 148, 149]. However, it is worth observing that astrophysical inputs (local DM density and its velocity distribution) are subject to large uncertainties, and the responses of detectors are not completely known (especially in the low mass region [150]).

2.4.2 Indirect searches

Dark matter indirect detection experiments look for signatures of DM annihilation or decay into (anti-)matter (AMS, PAMELA, CALET, DAMPE), photons (Fermi-LAT, EGRET, H.E.S.S., MAGIC, HAWC) and neutrinos (IceCube, ANTARES). A summary of the current constraints on annihilating dark matter is depicted in Fig. 2.3, for different final-state channels. Similar constraints can be obtained in case of decaying DM. In all these indirect

Experiment	Location	Readout	Target mass [kg]	Target	Dates
DAMA/NaI	Gran Sasso	γ	87	NaI	1995–2002
DAMA/LIBRA	Gran Sasso	γ	223	NaI	2003–
ANAIS	Canfranc	γ	11 / 100	NaI	2000–2005 / 2011–
KIMS	Yangyang	γ	35 / 104	CsI	2006–2007 / 2008–
CDMS II	Soudan	ϕ, q	1 / 3	Si / Ge	2001–2008 / 2001–2008
superCDMS	Soudan SNOLAB	ϕ, q	12	Ge	2010–2012 / 2013–2016
EDELWEISS I	Modane	ϕ, q	1	Ge	2000–2004
EDELWEISS II	Modane	ϕ, q	4	Ge	2005–
CRESST II	Gran Sasso	ϕ, γ	1	CaWO$_4$	2000–
SIMPLE	Rustrel	d	0.2	Freon	1999–
PICASSO	Sudbury	d	2	Freon	2001–
COUPP	Fermilab	d	2 / 60	Freon	2004–2009 / 2010–
CoGeNT	Chicago Soudan	q	0.3	Ge	2005– / 2008–
ZEPLIN III	Boulby	γ, q	7	LXe	2004–
LUX	Sanford	γ, q	100	LXe	2010–
XENON10	Gran Sasso	γ, q	5	LXe	2005–2007
XENON100	Gran Sasso	γ, q	50	LXe	2009–

Table 2.1: List of selected dark matter experiments, including fiducial mass and readout (scintillation light (γ), phonons (ϕ), ionization (q), and super-heated droplets (q)). The table has been adapted from Ref.s [143, 144].
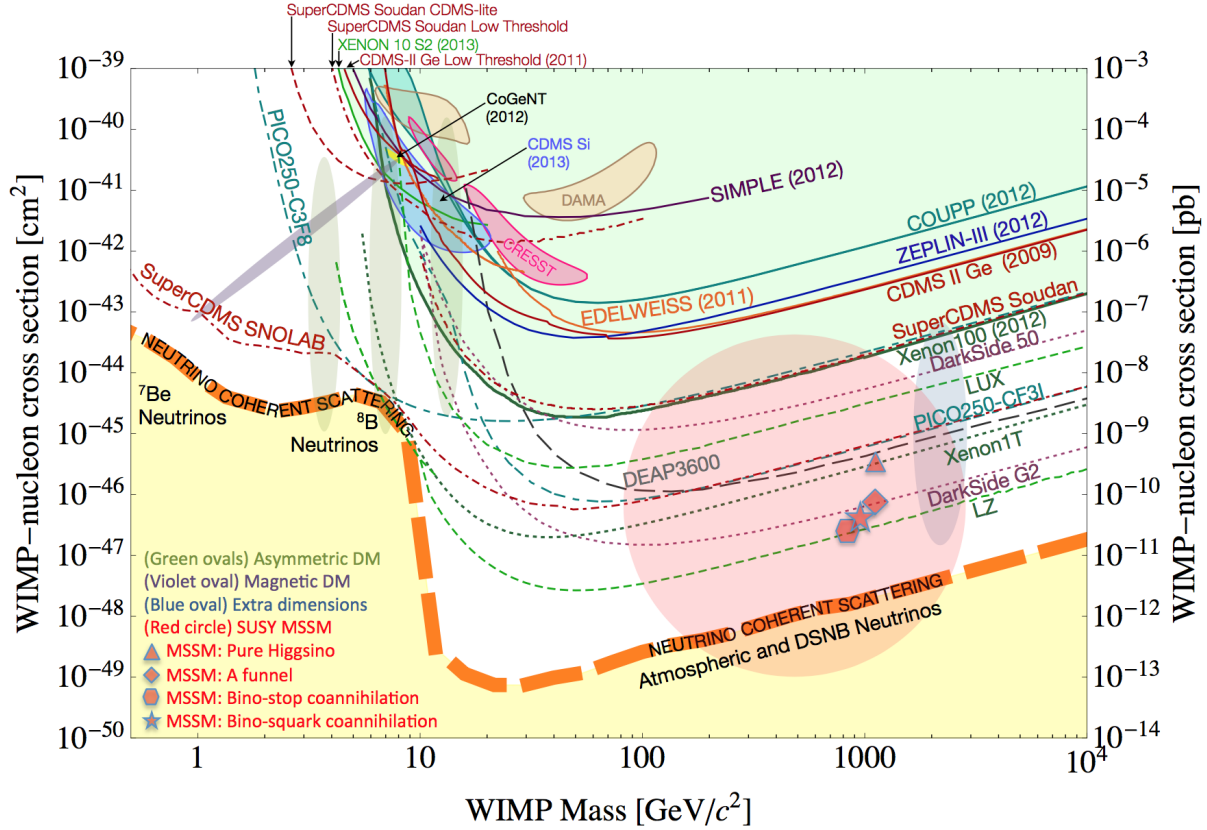
Figure 2.2: WIMP dark matter direct detection status circa 2014. The plot is taken from Ref. [145].

searches, a key role is played by the "background" from ordinary astrophysical processes, above which a possible DM signal is looked for. To the aim to overcome the astrophysical background, one has to consider different final-state channels (like the ones involving anti-matter) and range of energy, or to target regions of the space dominated by DM, like for example the Galactic Center of the Milky Way. However, the astrophysical background is in general affected by large uncertainty, especially in the case of charged particles due to the lack of a precise knowledge of interactions with galactic magnetic fields and with distributions of matter and light.

In this context, it is emblematic the data of the positrons and of anti-protons fractions. In particular, it was claimed that the observed steep increase in the energy spectrum of the positron fraction $e^+/(e^- + e^+)$ measured by PAMELA [152], Fermi [153] and AMS [154]
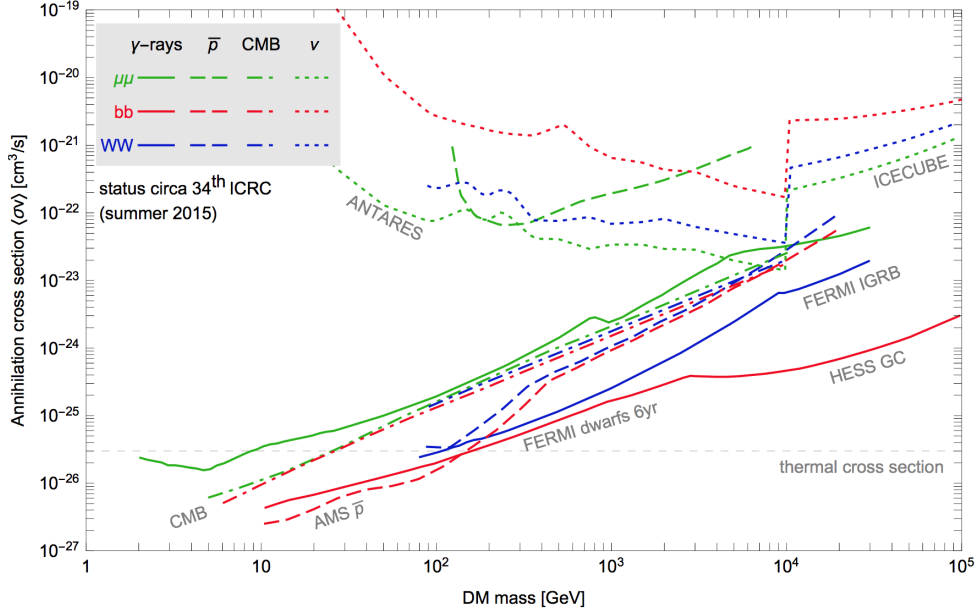
Figure 2.3: Current bounds (circa 2015) on annihilating dark matter, obtained by some experiments considering different annihilating channels. The plot has been taken from Ref. [151].

can be explained by leptophilic DM particles. However, the same signal can be obtained by considering nearby pulsars or supernova remnants. A similar situation occurs for the anti-proton fraction. The discrepancy between the PAMELA [155] and AMS [156] with the expectations from astrophysical observations can be reconciled by taking into account all the uncertainties in the calculation of the proton and anti-proton fluxes reaching the Earth [157].

In the next Chapter, we will discuss the ingredients required to evaluate the flux of neutrinos and gamma-rays produced by decaying/annihilating dark matter. As will be seen, the expected DM signals depend on the astrophysical details related to the DM density distribution in the region of observation. On the other hand, particle physics enters in the determination of the DM mass, annihilation cross section $\langle \sigma v \rangle$ or the decay lifetime τ_χ.

2.4.3   Colliders searches

Lastly, since WIMPs live at the weak scale, they can be detected at colliders like LHC. In this case, the creation of dark matter would be indicated by *missing energy*. For instance, the branching ratio of Higgs decays to invisible provides a very strong constrain on DM models for masses below $M_h/2$ based on the Higgs portal [158, 159]. Moreover, since it is possible to related the DM pair production rate at colliders to the annihilation and scattering at indirect and direct detection experiments, colliders searches represent a complementary probe in unveiling the nature of dark matter.

Chapter 3

Dark Matter Indirect Detection

Dark matter particles are gathered in our galaxy, the Milty Way, and surround other astrophysical objects. Depending on the interaction between DM and SM particles, dark matter can decay or annihilate producing particles like neutrinos, photons, electron and positrons and so on, that can reach the Earth and can be observed in satellite or underground detectors. The detection of these particles provides a way to indirectly infer the properties of dark matter particles. As will be discussed in this Chapter, the differential flux of particles produced by DM decays/annihilations depends on particles physics parameters and on astrophysical ones. The latter represents the major source of uncertainties affecting indirect DM searches.

Among the possible SM particles, neutrinos and photons are the best messengers for the study of the DM properties. Indeed, they are not (or slightly) affected by propagation effects that are in general related to galactic and intergalactic magnetic fields. On the other hand, in case of charged particles like electrons and positions one has to take into account their propagation in the galactic and intergalactic media. In this case, the differential flux at the Earth is modified and degraded in energy, and in general secondary particles are produced.

In this Chapter we describe all the ingredients that are necessary to compute the fluxes of neutrino (first Section), electrons/positrons (second Section) and photons (third Section) produced by different dark matter models.

3.1 Flux of Neutrinos

Let us firstly discuss the differential flux of neutrinos that are possibly produced by DM decays or annihilations. In this way, we present all the ingredients regarding particle physics and astrophysics that are required in indirect DM searches.

Neutrinos can be produced as primary or secondary particles by the decays of unstable DM particles or by the pair-annihilation of stable DM particles. The DM differential neutrino flux of a flavor α at the Earth (denoted with the symbol $\odot$) consists of two contributions

$$\frac{\mathrm{d}\phi_\alpha^{\mathrm{DM}}}{\mathrm{d}E_\nu \mathrm{d}\Omega}\bigg|_\odot = \sum_\beta P_{\alpha\beta} \left[\frac{\mathrm{d}\phi_\beta^{\mathrm{G}}}{\mathrm{d}E_\nu \mathrm{d}\Omega} + \frac{\mathrm{d}\phi_\beta^{\mathrm{EG}}}{\mathrm{d}E_\nu \mathrm{d}\Omega} \right] . \tag{3.1}$$

The first term corresponds to the Galactic (G) contribution associated with the Milky Way, while the secondrefers to the Extragalactic (EG) component. In case of neutrinos, the only effect due to the propagation is due to neutrino oscillations. In order to take into account the neutrino flavor oscillations during the propagation, the differential neutrino fluxes at the source and at the Earth are related by the mixing probabilities $P_{\alpha\beta}$. Such quantities are the probabilities that a neutrino of flavor β is converted into a neutrino of flavor α. By taking the limit of long baseline oscillations in Eq. (1.17) ($L \gg |\overrightarrow{p}_\nu|/\Delta m_\nu^2$) the mixing probabilities are equal to [160]

$$P_{ee} = 0.573\,, \qquad P_{e\mu} = 0.348\,, \qquad P_{e\tau} = 0.150\,,$$

$$\tag{3.2}$$

$$P_{\mu\mu} = 0.348\,, \qquad P_{\mu\tau} = 0.375\,, \qquad P_{\tau\tau} = 0.475\,.$$

Let us now report and discuss the expressions of the Galactic and Extragalactic flux of Eq. (3.1) for the two cases of decaying (dec.) and annihilating (ann.) DM particles. In the first case, the two contributions take, respectively, the expressions

$$\frac{\mathrm{d}\phi_\beta^{\mathrm{G}}}{\mathrm{d}E_\nu \mathrm{d}\Omega}\bigg|_{\mathrm{dec.}} = \frac{1}{4\pi\, m_{\mathrm{DM}}} \sum_f \Gamma_f \frac{\mathrm{d}N_{\nu_\beta}^f}{\mathrm{d}E_\nu} \int_0^\infty \mathrm{d}s\, \rho_h\left[r\left(s, \ell, b\right)\right] , \tag{3.3}$$

$$\frac{\mathrm{d}\phi_\beta^{\mathrm{EG}}}{\mathrm{d}E_\nu \mathrm{d}\Omega}\bigg|_{\mathrm{dec.}} = \frac{\Omega_{\mathrm{DM}}\rho_c}{4\pi\, m_{\mathrm{DM}}} \int_0^\infty \mathrm{d}z\, \frac{1}{\mathcal{H}(z)} \sum_f \Gamma_f \frac{\mathrm{d}N_{\nu_\beta}^f}{\mathrm{d}E_\nu}\bigg|_{E'=E(1+z)} . \tag{3.4}$$

In these expressions we can distinguish two different sets of parameters: the ones referred
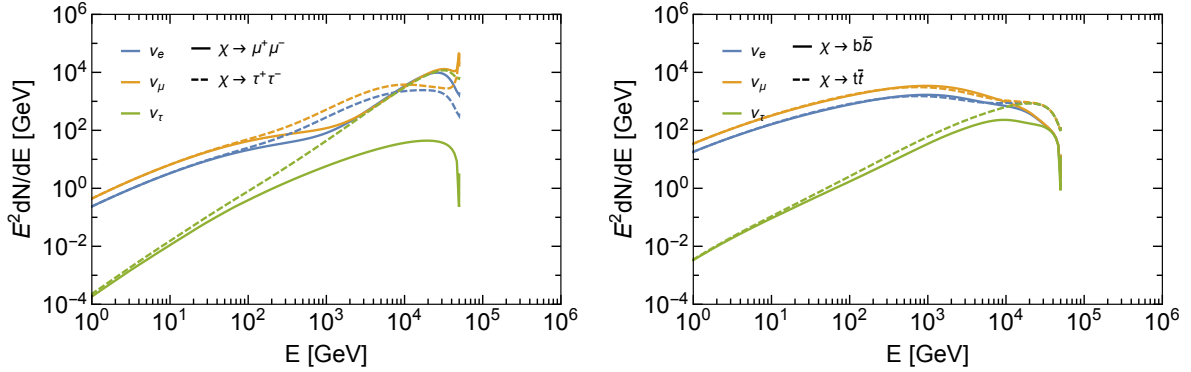
Figure 3.1: Three flavors neutrino energy spectra for four DM decay channels: leptonic (left panel) and hadronic (right panel) ones. The DM mass has been fixed to 100 TeV.

to particle physics and the ones to astrophysics. Among the particle physics parameters we have:

- **The Dark Matter mass** m_{DM}**.** This quantity provides the energy cut-off of the differential flux. Indeed, for a decay channel with n particle in the final-states, the maximum energy allowed for each particle is m_{DM}/n according to kinematics.

- **The decay channels** f **and their decay widths** Γ_f**.** In general, DM particles can decay through different channels producing primary and secondary neutrinos. The weight of each decay channel is represented by the decay width Γ_f. If it is not specified in the text, hereafter we consider only one decay channel at a time. In this case, we have

$$\sum_f \Gamma_f \frac{\mathrm{d}N^f_{\nu_\beta}}{\mathrm{d}E_\nu} \quad \rightarrow \quad \frac{1}{\tau_{\mathrm{DM}}} \frac{\mathrm{d}N_{\nu_\beta}}{\mathrm{d}E_\nu}, \tag{3.5}$$

where τ_{DM} is the DM lifetime.

- **The energy spectrum of neutrinos for a give channel.** The quantity $\mathrm{d}N_{\nu_\beta}/\mathrm{d}E_\nu$ is the energy spectrum of β-flavor neutrinos produced by DM particles, that means the number of neutrinos in the energy interval E–$E + \mathrm{d}E$. It depends on the particular DM interaction with the SM particles and, in general, is obtained by means of a Monte Carlo procedure. In Fig. 3.1 we report the energy spectra of three flavor neutrinos for a hundred TeV DM mass, in case of four different DM decay channels.

We note that in case of leptonic final states (left panel) the neutrino energy spectra are more peaked in correspondence of the DM mass, while in case of hadronic channels they are more flat. The energy spectra are taken from Ref. [161], where they have been evaluated up to a DM mass of 100 TeV by means of a Monte Carlo procedure that takes into account the decays of unstable SM particles (like pions) and the electroweak radiative corrections, which are relevant for heavy DM particles [162]. The electroweak radiative corrections correspond to the bremsstrahlung of electroweak W and Z bosons. They affect the energy spectra by providing unexpected particles in the final states, especially at low energies. The larger the DM mass, more relevant the electroweak radiative corrections, since it becomes more probable the emission of electroweak bosons. In order to perform the analysis for DM masses larger than 100 TeV, we extrapolate the energy spectra given in Ref. [161] by considering an appropriate rescaling. In particular, for $m_{\rm DM} \geq 100$ TeV, the energy spectrum is given by

$$\left. \frac{{\rm d}N_{\nu_\beta}}{{\rm d}E_\nu} \right|_{m_{\rm DM} \geq 100\,{\rm TeV}} = \frac{1}{E_\nu \ln(10)} \left. \frac{{\rm d}N_{\nu_\beta}}{{\rm d}\log x}(x) \right|_{100\,{\rm TeV}} \tag{3.6}$$

where the quantity ${\rm d}N_{\nu_\beta}/{\rm d}\log x$, provided in Ref. [161], is a function of the variable $x = E_\nu/m_{\rm DM}$ and it is evaluated with a DM mass of 100 TeV.

On the other hand, among the astrophysical parameters appearing in Eq.s (3.3) and (3.4) we have:

- **The DM halo density density.** The Galactic contribution given in Eq. (3.3) is proportional to the integral over the line-of-sight s of the galactic DM halo density $\rho_h(r)$, function of the radial coordinate

$$r = \sqrt{s^2 + r_\odot^2 - 2sr_\odot \cos\ell \cos b}, \tag{3.7}$$

where $r_\odot = 8.5$ kpc is the distance between the Sun and the Galactic Center, and (b, ℓ) are the Galactic coordinates. The DM halo density encodes how the DM particles are distributed in our galaxy. There exist different parametrization for $\rho_h(r)$, providing different effects to the numerical simulations of structure formation and to galactic

Dark Matter halo	α	r_s [kpc]	ρ_s [GeV/cm³]
NFW	–	24.42	0.184
Einasto	0.17	28.44	0.033
EinastoB	0.11	35.24	0.021
Isothermal	–	4.38	1.387
Burkert	–	12.75	0.712
Moore	–	30.28	0.105

Table 3.1: Parameters of the different DM halo density profiles reported in Eq. (3.8). The values are taken from Ref. [161].

rotation curves. We remind the following distributions referred as the Navarro-Frenk-White (NFW) [163], which is considered as a benchmark, Einasto [164, 165], Isothermal [166, 167],Burkert [168] and Moore [169]. They take the following expressions

$$
\begin{aligned}
\text{NFW}: \quad & \rho_{\text{NFW}}(r) = \rho_s \frac{r_s}{r}\left(1 + \frac{r}{r_s}\right)^{-2} \\
\text{Einasto}: \quad & \rho_{\text{Ein}}(r) = \rho_s \exp\left\{-\frac{2}{\alpha}\left[\left(\frac{r}{r_s}\right)^{\alpha} - 1\right]\right\} \\
\text{Isothermal}: \quad & \rho_{\text{Iso}}(r) = \frac{\rho_s}{1+(r/r_s)^2} \qquad\qquad (3.8)\\
\text{Burkert}: \quad & \rho_{\text{Bur}}(r) = \frac{\rho_s}{(1+r/r_s)\left(1+(r/r_s)^2\right)} \\
\text{Moore}: \quad & \rho_{\text{Moo}}(r) = \rho_s \left(\frac{r_s}{r}\right)^{1.16}\left(1 + \frac{r}{r_s}\right)^{-1.84}
\end{aligned}
$$

where the quantities ρ_s, r_s and α are reported in Tab. 3.1. In Fig. 3.2 we depict the different DM halo density distributions as a function of the radial coordinate r. As can be seen from the plot, they have very different behaviors especially towards the Galactic Center ($r = 0$). In this thesis, we mainly consider two DM halo density profiles that provide two extreme cases (predicting different angular distributions of neutrino arrival directions): the Navarro-Frenk-White distribution (NFW) and the Isothermal one (ISO). The former is enhanced towards the Galactic Center, while the latter is practically uniform.

- **Cosmological parameters.** The Extragalactic flux of Eq. (3.4) is instead obtained by integrating over the redshift z. The required cosmological parameters are the
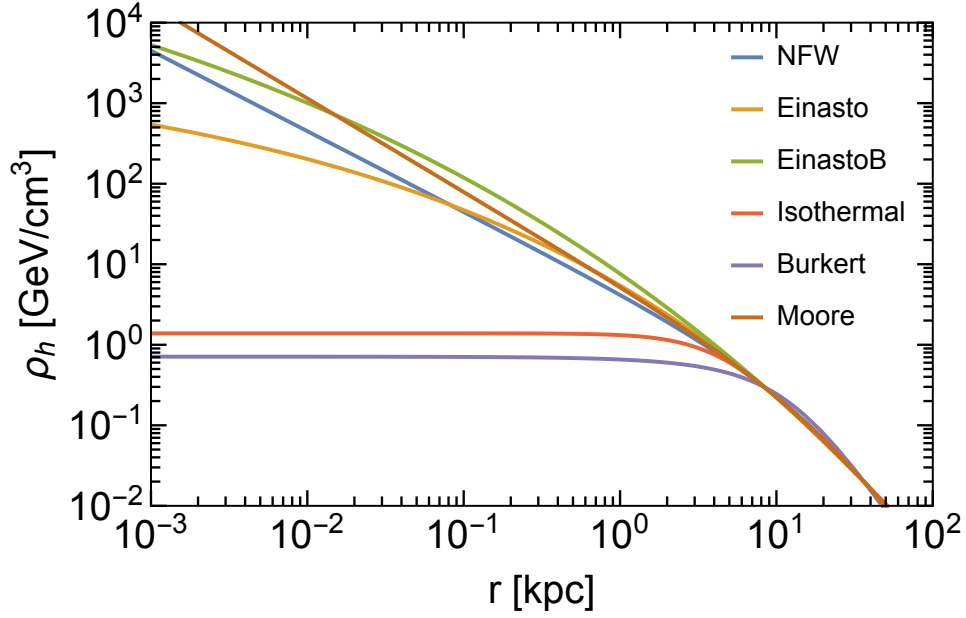
Figure 3.2: Different DM halo density profiles as a function of the radial distance r.

critical energy density $\rho_c = 5.5 \times 10^{-6} \, \mathrm{GeV} \, \mathrm{cm}^{-3}$ and the Hubble expansion rate

$$\mathcal{H}(z) = \mathcal{H}_0 \sqrt{\Omega_\Lambda + \Omega_m (1+z)^3} , \tag{3.9}$$

with $h = H_0/100 \, \mathrm{km} \, \mathrm{s}^{-1} \, \mathrm{Mpc}^{-1} = 0.6711$, $\Omega_{\mathrm{DM}} = 0.2685$, $\Omega_\Lambda = 0.6825$ and $\Omega_m = 0.3175$ according to Planck analysis [85]. Differently from the Galactic contribution, the Extragalactic one corresponds to an isotropic flux, i.e. it is independent on the Galactic coordinates (b, ℓ).

- **Propagation effects.** In case of neutrinos, the absorption in the intergalactic medium is negligible. However, as will be discussed in the next Sections, this is not the case for charged particles (electron and positrons) and photons.

In case of annihilating DM particles instead, the two contributions to the neutrino flux of Eq. (3.1) are equal to

$$\left. \frac{\mathrm{d}\phi_\beta^{\mathrm{G}}}{\mathrm{d}E_\nu \mathrm{d}\Omega} \right|_{\mathrm{ann.}} = \frac{1}{2} \frac{1}{4\pi \, m_{\mathrm{DM}}^2} \sum_f \langle \sigma v \rangle_f \frac{\mathrm{d}N_{\nu_\beta}^f}{\mathrm{d}E_\nu} \int_0^\infty \mathrm{d}s \, \rho_h^2 \left[r(s, \ell, b) \right] , \tag{3.10}$$

$$\left. \frac{\mathrm{d}\phi_\beta^{\mathrm{EG}}}{\mathrm{d}E_\nu \mathrm{d}\Omega} \right|_{\mathrm{ann.}} = \frac{1}{2} \frac{(\Omega_{\mathrm{DM}} \rho_c)^2}{4\pi \, m_{\mathrm{DM}}^2} \int_0^\infty \mathrm{d}z \, \frac{B(z) \, (1+z)^3}{\mathcal{H}(z)} \sum_f \langle \sigma v \rangle_f \left. \frac{\mathrm{d}N_{\nu_\beta}^f}{\mathrm{d}E_\nu} \right|_{E'=E(1+z)} . \tag{3.11}$$

Here, the quantity $\langle \sigma v \rangle_f$ is the thermally averaged cross section for the annihilation channel f. It is averaged over the DM velocity v, and over DM particle and anti-particles (providing the factor $1/2$). An additional factor of $1/2$ arises in case of Dirac DM particles. Moreover, in the Extragalactic component there is the quantity $B(z)$, i.e. the *boost factor* (or *clumpiness factor*). Such a quantity encodes the effect of the inhomogeneities of the DM distribution in the intergalactic medium. The clumpiness factor can be simply parametrized as [170]

$$B(z) = \frac{\Delta^2(0)}{(1+z)^3} , \qquad (3.12)$$

where the quantity Δ_0^2 ranges from 10^4 to 10^8 depending on the model considered [171]. In this thesis, we also adopt the cosmological boost factor reported in Ref. [161], which is numerically obtained by considering a Navarro-Frenk-White distribution in each subhalo and the *power-law* model [172, 173] with a minimum halo mass of $10^{-6} M_\odot$ [174, 175] for the concentration parameter. However, one has to underline that the boost factor is affected by large uncertainties, and the previous model has to be considered as a benchmark model. Indeed, different models for the concentration parameter, as well as different DM distributions, can be considered. This implies an uncertainty of orders of magnitude for the cosmological boost factor at low redshift. Such a large uncertainty mainly affects the angular distribution of neutrino arrival directions, as shown in Ref. [2].

3.2 Flux of charged particles: electron and positrons

Charged particles like electrons and positrons are trapped in the Galaxy by galactic magnetic fields and undergo several different interactions through which they loss energy. In order to take into account these effects due to propagation, one has to solve the diffuse-loss equation that for the electrons/positrons number density per unit energy

$$f(t, \overrightarrow{x}, E) \equiv \frac{\mathrm{d}n_{e^\pm}}{\mathrm{d}E} , \qquad (3.13)$$

takes the following expression

$$\frac{\partial f}{\partial t} - \nabla \left(\mathcal{K}(\overrightarrow{x}, E) \nabla f \right) - \frac{\partial}{\partial E} \left(b(\overrightarrow{x}, E) f \right) = Q(\overrightarrow{x}, E) . \qquad (3.14)$$

Here, the function $\mathcal{K}(\overrightarrow{x}, E)$ is *diffusion coefficient function* describing the propagation throughout the magnetic fields of the Galaxy. Such a function is affected by quite large uncertainties related to our lack of knowledge about the profile of the Galactic magnetic field. Furthermore, the function $b(\overrightarrow{x}, E)$ is the *energy loss coefficient function* that is related to different phenomena characterizing the energy losses of electrons and positrons during their propagations in the Galaxy [161]. In particular, the energy losses are due to [176]:

- coulomb interaction and ionization;

- bremsstrahlung, like the emission of gamma-ray;

- inverse Compton scattering, i.e. interactions with CMB, star-light and dust-diffused infrared light in the Galaxy;

- emission of synchrotron radiation.

Lastly, the function $Q(\overrightarrow{x}, E)$ is the *source term* and it is equal to

$$Q_{\text{dec.}} = \left(\frac{\rho_h(\overrightarrow{x})}{m_{\text{DM}}}\right) \sum_f \Gamma_f \frac{\mathrm{d}N^f_{e\pm}}{\mathrm{d}E}, \tag{3.15}$$

$$Q_{\text{ann.}} = \frac{1}{2}\left(\frac{\rho_h(\overrightarrow{x})}{m_{\text{DM}}}\right)^2 \sum_f \langle\sigma v\rangle_f \frac{\mathrm{d}N^f_{e\pm}}{\mathrm{d}E}, \tag{3.16}$$

where the quantity $\mathrm{d}N^f_{e\pm}/\mathrm{d}E$ is the energy spectrum of electrons/positrons produced in the decay/annihilation channel f.

The general solution of the Eq. (3.14) for the differential flux of electrons and positrons can be written as

$$\frac{\mathrm{d}\phi_{e\pm}}{\mathrm{d}E}(E, \overrightarrow{x}) = \frac{v_{e\pm}}{4\pi b(E, \overrightarrow{x})} \begin{cases} \left(\frac{\rho_h(\overrightarrow{x})}{m_{\text{DM}}}\right) \sum_f \Gamma_f \int_E^{m_{\text{DM}}/2} \mathrm{d}E_s \frac{\mathrm{d}N^f_{e\pm}}{\mathrm{d}E}(E_s) I(E, E_s, \overrightarrow{x}) \\ \frac{1}{2}\left(\frac{\rho_h(\overrightarrow{x})}{m_{\text{DM}}}\right)^2 \sum_f \langle\sigma v\rangle_f \int_E^{m_{\text{DM}}} \mathrm{d}E_s \frac{\mathrm{d}N^f_{e\pm}}{\mathrm{d}E}(E_s) I(E, E_s, \overrightarrow{x}) \end{cases} \tag{3.17}$$

where the function $I(E, E_s, \overrightarrow{x})$ is the Green function of Eq. (3.14), which relates the flux at production with energy E_s to the flux differential flux with energy E, for each given position $\overrightarrow{x}$. The Green function is obtained by means of numerical or semi-analytical

approach (for more details see Ref. [161, 176]) under some approximations. In general, the diffuse-loss equation (3.14) is solved in a region with a shape of a cylinder containing the galactic plane. Moreover, the solutions are obtained by considering the approximation of steady condition, i.e. neglecting the derivative on time.

3.3 Flux of gamma-rays

As for neutrinos, the differential flux of *gamma-rays* (high-energy photons) consists of Galactic and Extragalactic components.

$$\frac{\mathrm{d}\phi_\gamma^{\mathrm{DM}}}{\mathrm{d}E_\gamma \mathrm{d}\Omega}\bigg|_\odot = \frac{\mathrm{d}\phi_\gamma^{\mathrm{G}}}{\mathrm{d}E_\gamma \mathrm{d}\Omega} + \frac{\mathrm{d}\phi_\gamma^{\mathrm{EG}}}{\mathrm{d}E_\gamma \mathrm{d}\Omega}. \tag{3.18}$$

However, differently from neutrinos, in addition to *prompt* gamma-rays produced directly by DM decays/annihilations there are also secondary photons related to the interactions of electrons and positrons. Indeed, secondary high-energy photons (gamma-rays) are produced in inverse Compton scatterings, while low-energy photons (X-rays) are emitted by synchrotron interactions. In this thesis, we are mainly focused on gamma-rays, hence we report only the expression for secondary photons produced in inverse Compton scatterings. The prompt Galactic gamma-ray flux is given by

$$\frac{\mathrm{d}\phi_\gamma^{\mathrm{G}}}{\mathrm{d}E_\gamma \mathrm{d}\Omega}\bigg|_{\mathrm{dec.}} = \frac{1}{4\pi\, m_{\mathrm{DM}}} \sum_f \Gamma_f \frac{\mathrm{d}N_\gamma^f}{\mathrm{d}E_\gamma} \int_0^\infty \mathrm{d}s\, \rho_h\left[r\left(s,\ell,b\right)\right], \tag{3.19}$$

$$\frac{\mathrm{d}\phi_\gamma^{\mathrm{G}}}{\mathrm{d}E_\gamma \mathrm{d}\Omega}\bigg|_{\mathrm{ann.}} = \frac{1}{2}\frac{1}{4\pi\, m_{\mathrm{DM}}^2} \sum_f \langle\sigma v\rangle_f \frac{\mathrm{d}N_\gamma^f}{\mathrm{d}E_\gamma} \int_0^\infty \mathrm{d}s\, \rho_h^2\left[r\left(s,\ell,b\right)\right]. \tag{3.20}$$

Instead, the contribution to the galactic gamma-ray flux provided by inverse Compton scatterings of electrons and positrons can be cast into the following expression

$$\frac{\mathrm{d}\phi_{\mathrm{IC}\gamma}}{\mathrm{d}E_\gamma \mathrm{d}\Omega} = \frac{1}{E_\gamma^2}\frac{r_\odot}{4\pi}\begin{cases}\left(\frac{\rho_\odot}{m_{\mathrm{DM}}}\right)\int_{m_e}^{m_{\mathrm{DM}}/2} dE_s \sum_f \Gamma_f \frac{\mathrm{d}N_{e\pm}^f}{\mathrm{d}E}\left(E_s\right) I_{\mathrm{IC}}\left(E_\gamma, E_s, b, \ell\right) \\ \frac{1}{2}\left(\frac{\rho_\odot}{m_{\mathrm{DM}}}\right)^2 \int_{m_e}^{m_{\mathrm{DM}}} dE_s \sum_f \langle\sigma v\rangle_f \frac{\mathrm{d}N_{e\pm}^f}{\mathrm{d}E}\left(E_s\right) I_{\mathrm{IC}}\left(E_\gamma, E_s, b, \ell\right)\end{cases} \tag{3.21}$$

where $I_{\mathrm{IC}}\left(E_\gamma, E_s, b, \ell\right)$, function of the observed energy of gamma-rays E_γ, of the energy of electrons/positrons at the production E_s, and of the Galactic coordinates (b, ℓ), is a sort of

Green function for the Inverse Compton (IC) radiative processes. It takes the expression

$$I_{\text{IC}}(E_\gamma, E_s, b, \ell) = 2E_\gamma \int_0^\infty \frac{ds}{\rho_\odot} \left(\frac{\rho_h\left[r\left(s, \ell, b\right)\right]}{\rho_\odot} \right)^\eta \int_{m_e}^{E_s} dE \, \frac{\mathcal{P}_{\text{IC}}(E_\gamma, E, r)}{b(E, r)} I(E, E_s, r) ,$$

(3.22)

where $\mathcal{P}_{\text{IC}}$ is the differential power emitted into photon due to inverse Compton scatterings and $I(E, E_s, r)$ is the Green function of the diffuse-loss equation for electrons/positrons. The power η is equal to 1 and 2 in case of DM decays and annihilations, respectively.

Lastly, the differential Extragalactic flux of gamma-rays is given by

$$\left. \frac{\mathrm{d}\phi_\gamma^{\text{EG}}}{\mathrm{d}E_\gamma \mathrm{d}\Omega} \right|_{\text{dec.}} = \frac{\Omega_{\text{DM}}\rho_c}{4\pi \, m_{\text{DM}}} \int_0^\infty dz \, \frac{1}{\mathcal{H}(z)} \sum_f \Gamma_f \left. \frac{\mathrm{d}N_\gamma^f}{\mathrm{d}E_\gamma} \right|_{E'=E(1+z)} e^{-\tau(E,z)} ,$$

(3.23)

$$\left. \frac{\mathrm{d}\phi_\gamma^{\text{EG}}}{\mathrm{d}E_\gamma \mathrm{d}\Omega} \right|_{\text{ann.}} = \frac{1}{2} \frac{(\Omega_{\text{DM}}\rho_c)^2}{4\pi \, m_{\text{DM}}^2} \int_0^\infty dz \, \frac{B(z)\,(1+z)^3}{\mathcal{H}(z)} \sum_f \langle\sigma v\rangle_f \left. \frac{\mathrm{d}N_\gamma^f}{\mathrm{d}E_\gamma} \right|_{E'=E(1+z)} e^{-\tau(E,z)}$$

(3.24)

where the function $\tau(E, z)$ encodes the absorption of gamma-rays during their propagation. Indeed, photons with energy larger than MeV are absorbed through processes of pair production on baryonic matter, and of photon-photon scattering and pair production on ambient photon background radiation. Then, the extragalactic secondary emission of gamma-ray due to inverse Compton scatterings with electrons and positrons is given by

$$\frac{\mathrm{d}\phi_\gamma^{\text{EG}}}{\mathrm{d}E_\gamma \mathrm{d}\Omega} = \frac{1}{4\pi} \int_0^\infty dz \, \frac{1}{\mathcal{H}(z)\,(1+z)^3} j_{\text{EG}\gamma}^{\text{IC}}(E', z)\, e^{-\tau(E,z)} ,$$

(3.25)

where $E' = E(1+z)$ and

$$j_{\text{EG}\gamma}^{\text{IC}}(E', z) = 2 \int_{m_e}^{m_{\text{DM}}(/2)} dE_e \, \frac{\mathcal{P}_{\text{IC}}(E', E_e, z)}{b(E_e, z)} \int_{m_e}^{m_{\text{DM}}(/2)} d\tilde{E}_e \sum_f \frac{\mathrm{d}N_{e\pm}^f}{\mathrm{d}\tilde{E}_e} \left\{ \begin{array}{l} \left(\frac{\Omega_{\text{DM}}\rho_c(1+z)^3}{m_{\text{DM}}} \right) \Gamma_f \\ \frac{1}{2} \left(\frac{\Omega_{\text{DM}}\rho_c(1+z)^3}{m_{\text{DM}}} \right)^2 B(z) \langle\sigma v\rangle_f \end{array} \right.$$

(3.26)

Chapter 4

Physics at Neutrino Telescopes

In this Chapter, we report the main observations made at ICeCube and ANTARES Neutrino Telescopes, and discuss the possible astrophysical interpretation of the diffuse extraterrestrial neutrino flux in the TeV–PeV energy range. The measurement of such a flux is fundamental to astroparticle physics and astrophysics since it provides an important diagnostic tool for physics and astrophysics. This branch of physics is indeed important for different reasons [177].

- Neutrinos, which are neutral and weakly interacting particles, are the best messenger of the cosmos. Due to their nature, neutrinos that are produced in astrophysical objects have a high probability to escape the sources, while protons and photons could be absorbed in the astrophysical environment itself. Hence, detecting high-energy neutrinos can potentially allow us to observe the so-called "hidden sources" that do not emit cosmic-rays and gamma-rays.

- The Universe is not transparent to gamma-rays (high-energy photons) with energies higher than TeV. Indeed, they are absorbed on background radiation through the pair production process $\gamma + \gamma_{\mathrm{bkg}} \to e^+ + e^-$ above a threshold energy that depends on the energy of the background photons. For example, PeV gamma-rays are absorbed in the interactions with the CMB. Hence, neutrinos allow us to trace back very distant sources even in presence of intergalactic backgrounds and magnetic fields.

- The observation of astrophysical neutrinos is a proof for the acceleration of hadronic matter in Galactic and Extragalactic astrophysical environments and can help us to better understand the mechanism of the production of cosmic-rays.

- The IceCube detector is able to measure with high precision the atmospheric neutrinos which are produced in the atmosphere by cosmic-rays.

- The detection of very energetic neutrinos is of paramount importance for elementary particle physics, because it gives the chance to explore very high-energy phenomena that can be potentially linked to new physics (leptoquarks, violation of Lorentz invariance, non-standard neutrino interactions, etc.). For example, neutrinos can be produced by the decays or annihilations of very heavy DM particles (this subject will be analyzed in detail in later Chapters).

The Chapter is organized as follows. In the first two Sections we discuss the atmospheric and the astrophysical neutrinos, respectively. The third Section is devoted to review the IceCube experiment, while the fourth Section is dedicated to ANTARES telescope and its upgrade KM3NeT. In the fifth Section we report the combined analysis of IceCubed and ANTARES data samples, while in the sixth Section we highlight the tension of both data sets with the parametrization of the neutrino flux in terms of a single power-law.

4.1 Atmospheric neutrinos

In the underground based Neutrino Telescopes, one has to distinguish neutrinos that have an astrophysical origin from ones that are produced by cosmic-rays in the Earth's atmosphere. The former are related to astrophysical objects (or possibly to DM interactions) and, therefore, physicists are interested in measuring their flux. While the latter are neutrinos that are produced through different chains, starting from the interaction of cosmic-ray particles with the particles of the Earth's atmosphere, and play the role of a background. Before discussing the *astrophysical neutrinos*, we firstly describe the so-called *atmospheric neutrino background*. Such a background is generally divided into two different fluxes depending on how neutrinos are produced:

- the *conventional* atmospheric background consists of penetrating muons and neutrinos produced by the π/K decays in the atmosphere [178];

- the *prompt* atmospheric background corresponds instead to neutrinos produced by the decays of charmed mesons [179].

4.1.1 Conventional atmospheric background

The conventional background represents the main part of atmospheric neutrinos at low energies. In particular, they are originated in two different chains. The first one is given by the process

$$\pi^{\pm} \rightarrow \mu^{\pm} + \nu_{\mu} \left(\overline{\nu}_{\mu} \right) , \tag{4.1}$$

while the second one is

$$K^{\pm} \rightarrow \mu^{\pm} + \nu_{\mu} \left(\overline{\nu}_{\mu} \right) . \tag{4.2}$$

In addition to this process, kaon mesons also decay into pions through the processes

$$K^{\pm} \rightarrow \pi^{\pm} + \pi^0 \qquad \text{and} \qquad K^{\pm} \rightarrow \pi^0 + e^{\pm} + \nu_e \left(\overline{\nu}_e \right) . \tag{4.3}$$

At low energies (GeV), muon also decay in the atmosphere before reaching the Earth and produces neutrinos and electrons

$$\mu^{\pm} \rightarrow e^{\pm} + \nu_e \left(\overline{\nu}_e \right) + \overline{\nu}_{\mu} \left(\nu_{\mu} \right) . \tag{4.4}$$

Here, the flavor ratio $\left(\nu_{\mu} + \overline{\nu}_{\mu} \right) / \left(\nu_e + \overline{\nu}_e \right)$ is approximately equal to 2, since the conventional atmospheric background is dominated by muon decays.

At $\mathcal{O}$ (TeV) energies, the conventional atmospheric flux is dominated by π/K decays and behaves as $\sim E^{-3.7}$ [178, 180, 181, 182, 183]. This behavior is due to fact that high-energy pions and kaons have a higher probability to interact before decaying, which steepens the cosmic-ray spectrum $\sim E^{-2.7}$ by one power. At these energies, muons do not decay anymore because their lifetime becomes longer and consequently they can reach the Earth and the underground detector. Moreover, the muon neutrino and the muon originated in the same decay (4.1) and (4.2) have the same direction, or, in other words, the opening angle between
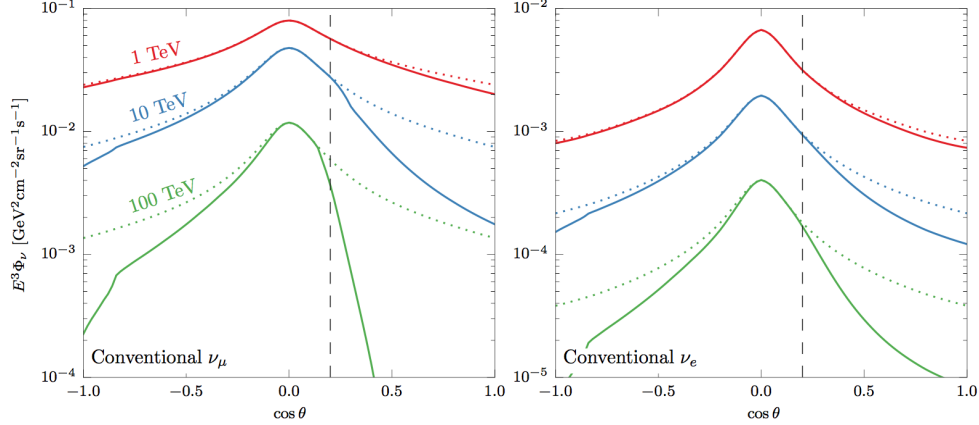
Figure 4.1: Effective conventional atmospheric background (solid lines) for the IceCube experiment as a function of the Zenith angle θ for muon (left panel) and electron (right panel) neutrinos. For down-going neutrinos ($\cos\theta \geq 0.2$) the suppression is provided by looking for the accompanied muons that reach the IceCube detector [185], while for up-going neutrinos ($\cos\theta \leq 0.2$) it is related to the absorption during the propagation through the Earth. The plots are taken from Ref. [186].

ν_μ and μ is very small. Hence, since an atmospheric ν_μ has a certain probability to reach the detector accompanied with its partner μ, the observation of a muon track passing through the detector can be used to suppress the conventional atmospheric background coming from the sky (down-going neutrinos) [184, 185]. In Fig. 4.1, one can see the portion of the conventional atmospheric neutrino flux that is not accompanied by muons and, therefore, cannot be suppressed by looking for muon tracks passing through the IceCube detector. It is worth observing that this suppression works only for down-going neutrinos for which the partner muons are not absorbed by the Earth (in case of IceCube experiment located at the South Pole, down-going neutrinos come from the Southern hemisphere, i.e. $\cos\theta \geq 0.2$). This veto technique is indeed used by the IceCube Collaboration.

At higher energies, the conventional atmospheric background is further suppressed since the lifetime of pions and kaons becomes longer and the interaction probability dominates on the decay. Therefore, for neutrino energies lager than 100 TeV the conventional atmospheric background starts to be negligible.

In general, the angular distribution of the atmospheric background is isotropic. However,
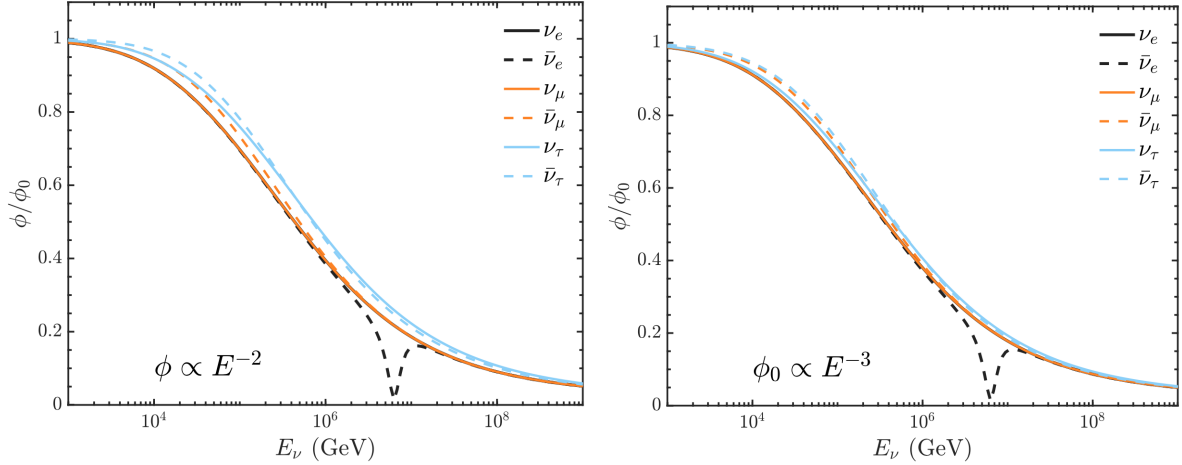
Figure 4.2: Attenuation due to the absorption by the Earth as a function of the neutrino energy, for neutrinos and anti-neutrinos of different flavors. The left panel corresponds to a neutrinos flux $\phi_0 \propto E^{-2.0}$, while the right panel refers to $\phi_0 \propto E^{-3.0}$. The plots are taken from Ref. [187].

at energies larger than 1 TeV the Earth is not transparent to neutrinos. The Earth's opacity is due to the interactions of neutrinos with the particles (mostly protons and neutrons) making up the Earth. At energies up to $E_\nu = 1\,\text{PeV}$, neutrinos are absorbed more than anti-neutrinos since they mainly scatter off the nuclei in the Earth. Since such nuclei are heavy and, therefore, contain more neutrons (uud) than protons (uud), neutrinos interact through the exchange of a W boson with a d quark more efficiently than anti-neutrinos, which instead interact with u quarks. When the energy becomes higher, valence quarks are negligible with respect to the sea quarks, and the interactions of neutrinos and anti-neutrinos with the nuclei asymptotically become equal. Moreover, at a neutrino energy $E_\nu \approx M_W^2/2m_e \approx 6 \times 10^6\,\text{GeV}$, one has to take into account the resonance

$$e^- + \overline{\nu}_e \rightarrow W^- \rightarrow X\,, \tag{4.5}$$

implying that electron anti-neutrinos are absorbed passing through the Earth more than electron neutrinos. The attenuation of the neutrino flux due to the absorption by the Earth is displayed in Fig.s 4.1 and 4.2, where it is reported its dependence on the Zenith angle ($\cos\theta \leq 0.0$) and the neutrino energy, respectively.

In the present thesis, we adopt the calculations of the conventional atmospheric back-

ground performed by Honda et al. [178] that is considered as a benchmark by the scientific community. However, it is worth noticing that such an estimation is affected by large uncertainties related to the hadronic interaction models for the production of mesons in the atmosphere and to cosmic-ray spectral shape and composition at the knee ($\sim 3 \times 10^{15}$ eV). In Ref. [188], a detail treatment of such uncertainties has shown that the atmospheric muon flux is affected by an average error of $^{+15}_{-13}\%$, while the muon and electron neutrino fluxes are evaluated within an average error of $^{+32}_{-22}\%$ and $^{+25}_{-19}\%$, respectively.

4.1.2 Prompt atmospheric background

The prompt atmospheric background flux [179, 189, 190] consists of neutrinos produced in the semi-leptonic decays of charmed mesons and baryons. Their contribution to the total atmospheric flux is expected to be important above 100 TeV, where the only other contribution provided by K decays starts to be negligible. The prompt flux is expected to behave as the cosmic-ray spectrum, i.e. $\sim E^{-2.7}$, because the charmed mesons immediately decay (the rest-frame lifetimes are of the order of 10^{-12} s) and do not have time to propagate in the atmosphere. As for the conventional flux, the calculations of the prompt atmospheric background are affected by uncertainties related to the cosmic-ray normalization and spectral distribution. However, it is also affected by the large uncertainties on the charm production cross sections, which have not been measured in colliders at these high energies.

It is worth noticing the measurements of the atmospheric background made by AMANDA (Antartic Muon And Neutrino Detection Array) [191] and IceCube [186, 192, 193, 194, 195] have not found a significant contribution from charm hadron decays. Moreover, the latest calculations [196, 197, 198], which take into account the new measurements of the hadronic cross sections, predict a prompt neutrino flux that is in general lower than its previous benchmark estimation [179]. For these reasons, in the following analyses we do not take into account the prompt atmospheric background that is hence considered as negligible.

4.2 Astrophysical neutrinos

Differently from the atmospheric neutrinos, the astrophysical neutrinos are the ones that are originated in astrophysical environments where hadronic matter (protons) is accelerated by magnetic fields and then interact with gas or with radiation. Therefore, depending on how the neutrinos are produced, we mainly divide the astrophysical sources into two different classes:

- the *p*-*p* astrophysical sources, where neutrinos are originated by the interactions of accelerated protons with the gas (proton-proton collisions). This interaction is expected for cosmic-ray reservoirs, where the cosmic-rays escaping from their accelerators are confined in magnetized environments for a long time. In this case, the neutrinos are produced through the following processes

$$p + p \rightarrow \pi^+ + \pi^- + \pi^0 \qquad \text{and} \qquad \begin{cases} \pi^\pm \rightarrow \mu^\pm + \nu_\mu \, (\overline{\nu}_\mu) \\ \pi^0 \rightarrow \gamma + \gamma \end{cases} . \qquad (4.6)$$

  In general, neutrinos carry in average the 5% of the energy of the parent proton ($E_\nu \approx 0.05 E_p$).

- the *p*-γ astrophysical sources, where neutrinos are instead produced in the interactions of accelerated protons with light (proton-gamma collisions). The cosmic-rays escape from the astrophysical environment and interact with radiation (like the CMB) in the intergalactic space. For this kind of sources, the neutrinos are produced via the resonance

$$p + \gamma \rightarrow \Delta \rightarrow \begin{cases} \pi^+ & 1/3 \, \text{of cases} \\ \pi^0 & 2/3 \, \text{of cases} \end{cases} , \qquad (4.7)$$

  and the pions later decay into neutrinos and gamma-rays.

In both cases, the flavor ratio of neutrinos at the source is

$$(\nu_e, \nu_\mu, \nu_\tau)_S = (1, 2, 0) . \qquad (4.8)$$

However, due to neutrino oscillations during the propagation, the standard astrophysical sources predict an equal flavor ratio at the Earth.

$$(\nu_e, \nu_\mu, \nu_\tau)_\oplus = (1, 1, 1) . \qquad (4.9)$$

Hence, is it reasonable to assume a correlation between the observed astrophysical neutrinos and the hadronic cosmic-rays. Thus the dependence of the neutrino flux on energy should be, at the source, mostly related to the differential spectrum of charged cosmic-rays and to the pions production efficiency. Under such a hypothesis, the differential neutrino flux (at a given energy E_ν, per unit solid angle Ω and per neutrino flavor α) can be parametrized by a *power-law* behavior

$$\frac{\mathrm{d}\Phi_\alpha^{\mathrm{astro}}}{\mathrm{d}E_\nu \mathrm{d}\Omega} = \frac{1}{4\pi}\Phi_{\mathrm{astro}}^0 \left(\frac{E_\nu}{100 \text{ TeV}}\right)^{-\gamma}, \tag{4.10}$$

where Φ_{astro}^0 is the normalization of the neutrino flux at 100 TeV and γ is the so-called *spectral index*. This parametrization does not depend on the angular coordinates and provides an isotropic neutrino flux as expected for extragalactic astrophysical sources. Moreover, the normalization Φ_{astro}^0 is equal for each neutrino flavor α according to the prediction of flavor ration 1:1:1 at the Earth. In this expression, the sum over neutrinos and anti-neutrinos of flavor α is implicitly assumed.

Depending on the properties of the astrophysical source, the protons can be in general accelerated up to a maximum energy

$$E_p^{\mathrm{max}} = BR, \tag{4.11}$$

where B the magnetic field and R the size of the source. Therefore, one can also parametrized the neutrino flux in terms of a *broken* power-law (BPL) with an exponential cut-off

$$\frac{\mathrm{d}\Phi_\alpha^{\mathrm{astro\,(broken)}}}{\mathrm{d}E_\nu \mathrm{d}\Omega} = \frac{1}{4\pi}\Phi_{\mathrm{astro}}^0 \left(\frac{E_\nu}{100 \text{ TeV}}\right)^{-\gamma} \exp\left(-\frac{E_\nu}{E_\nu^{\mathrm{max}}}\right), \tag{4.12}$$

where E_ν^{max} is typically equal to 5% of E_p^{max}.

The power-law behavior is predicted for protons that are accelerated by magnetic field in a gas cloud or in a shock front [199, 200]. The benchmark prediction of the Fermi acceleration mechanism is a power-law with spectral index $\gamma = 2.0$ [199, 200, 201, 202, 203]. However, depending on the particular neutrino production mechanism there can be deviations from such a value. For instance, if neutrinos arise from hadronuclear *p-p* interactions then $\gamma \lesssim 2.2$ [204, 205], since the neutrino spectral shape follows the initial proton (or

hadron) spectrum. On the other hand, models with photohadronic p-γ interactions generally produce peaked spectra [206], then one could have a steep flux ($\gamma \gtrsim 2.2$) depending on the position of the peak.

In general, theoretical models of acceleration mechanism for hadronic matter produce a flux that should be at most as soft as $E_\nu^{-2.4}$. This is expected for Galactic sources once the proton spectrum at the source is compared to the one measured at the Earth. Once the propagation effects are taken into account, the galactic cosmic-ray spectrum at the Earth becomes $\propto E^{-(\gamma+\delta)}$ with $\gamma + \delta \approx 2.7$ up to the knee at $1 \div 10$ PeV [28]. The quantity $\delta = 0.3 \div 0.6$ depends on galactic magnetic fields [207, 208].

Different extragalactic astrophysical sources have been proposed as potential candidates providing a contribution to the extraterrestrial neutrino flux in TeV–PeV range [177, 209]. Among such sources one can quote:

- **SuperNovae Remnants (SNRs)** [210, 211, 212] are related to the final stage in the evolution of stars with a mass eight times bigger than the mass of the Sun. The hadronic matter is accelerated by the shock waves through the Fermi mechanism. As pointed out in Ref.s [213, 214, 212, 215], the gamma-ray flux produced in these p-p astrophysical sources is constrained by the Fermi-LAT measurements [216]. This leads to a corresponding constraint on the neutrino flux, i.e. the spectral index has to be smaller than 2.2. Moreover, it was claimed that, according to the gamma-ray constraints, star-forming galaxies can provide at most a contribution to the neutrino flux of $\sim 30\%$ at 100 TeV and $\sim 60\%$ at 1 PeV [214]. Therefore, they cannot be the dominant neutrino sources. The tension between neutrino and gamma-ray data can be alleviated by considering the uncertainties on the gamma-rays absorption in the astrophysical environment itself and in the intergalactic medium [212]. In case of StarBurst galaxies (SB) the radio observations lead to a lower bound on the cumulative diffuse neutrino flux [204]

$$E_\nu^2 \phi_\nu^{\mathrm{SB}} \approx 10^{-7} \left(\frac{E_\nu}{1\,\mathrm{GeV}} \right)^{-0.15 \pm 0.1} \mathrm{GeV\,cm^{-2}\,s^{-1}\,sr^{-1}}, \qquad (4.13)$$

implying the constraint on the spectral index $\gamma \leq 2.25$.

- **Active Galactic Nuclei (AGN)** [217, 218, 219, 220] are accelerators in the center of a young galaxy. The most powerful AGN are Blazars that are AGN with a super-massive black hole accelerating matter via jets. These objects can be see if the jets point towards the Earth. The contribution of AGN to the diffuse TeV–PeV neutrino flux is constrained by searches for spatial correlation with the Fermi-LAT observations (point-like searches) [221, 222, 223]. Such analyses claim that AGN can explain up to $\sim 25\%$ of the diffuse TeV–PeV neutrino spectrum, only.

- **Gamma Ray Bursts (GRBs)** [224, 225, 226] are generated in some type of cataclysmic transient process involving dying massive stars. GRBs are excellent sources of neutrinos with energies from MeV to EeV and above. However, the non-observation of spatial and temporal correlations with the detection of gamma-rays at Fermi-LAT provides very stringent constraints on GRBs [227, 228]. In particular, only $\sim 1\%$ of the total diffuse TeV–PeV neutrino flux can be accounted for by GRBs [228, 229].

In general, one can set an upper bound to these kinds of astrophysical objects, assuming that they provide a contribution to cosmic-ray spectrum as well. In particular, this is the so-called Waxman-Bahcall bound (WB) that implies [230]

$$E_\nu^2 \phi_\nu^{\text{WB}} \lesssim 2 \times 10^{-8}\,\text{GeV}\,\text{cm}^{-2}\,\text{s}^{-1}\,\text{sr}^{-1}\,. \tag{4.14}$$

It is worth observing that such a bound and the multi-messenger constraints with gamma-rays do not hold in case of *hidden* astrophysical sources, in which cosmic-rays and gamma-rays are absorbed in the surrounding environment [231, 232, 233]. For instance, in case of low-luminosity GRBs with choked jets [233], no production of detectable gamma-rays in GeV–TeV energy range is expected, avoiding in this way the Fermi-LAT constraints.

If we consider a marginal contribution of the hidden sources to the diffuse TeV–PeV neutrino flux, in view of the previous considerations one can regard as fully compatible models for neutrino flux the one that predict a power-law with spectral index between 2.0 (Fermi acceleration mechanism) and about 2.2 (upper bound from the observations of gamma-rays at Fermi-LAT experiment). The range $[2.0, 2.2]$ is also compatible with the bound provided in Eq. (4.13).

4.3   IceCube Experiment

The IceCube Neutrino Observatory, located at the National Science Foundation's Amundsen-Scott South-Pole Station, is a huge Cherenkov detector with a fiducial volume of 1 km³. The experiment is based on the Cherenkov effect affecting charged particles produced by neutrinos after their interaction with nuclei in the ice. The photons are collected by Digital Optical Modules (DOMs), that are equipped with Photo-Multipliers (PMTs). The detector consists of 86 strings with 60 DOMs each, between 1450 m and 2450 m below the surface. It is places underground in deep ice in order to suppress part of the atmospheric flux of down-going muons that are absorbed before reaching the detector. Moreover, part of the detector as a veto in order to distinguish the atmospheric muons from the neutrinos, whose induced events start inside the fiducial volume. Such a veto, as already discussed in Section 4.1, is useful to discard both atmospheric muons and atmospheric neutrinos, which at high energies are accompanied by collinear muons. Taking into account also a threshold on the deposited energy for each event, the veto technique is able to discard 99.999% of the atmospheric muon background.

In IceCube, there were observed two different event topology: *tracks* and *showers*. The tracks are related to CC interactions of muon neutrinos

$$\nu_\mu + N \to \mu + X \,, \tag{4.15}$$

where the energetic muon can travel through the entire detector and, consequently, produces a track as signature. For this event topology, the angular resolution is $\sim 1°$ at 50% C.L.. The showers, instead, correspond to CC interactions of electron and tau neutrinos and to NC interactions of all flavors

$$\nu_\alpha + N \to \nu_\alpha + X \,. \tag{4.16}$$

The angular resolution is worse, namely $\sim 15°$ at 50% C.L.. There exists a third event topology that has not been observed so far: the *double-bang*. Such a topology occurs when a very energetic τ lepton ($E_\nu \gtrsim 1\,\mathrm{PeV}$) is produced and then decay far from the first vertex interaction. This produces two different shower-like vertexes.

Depending on the different veto implementations and on the characteristics of the events, the IceCube data are divided into three classes:
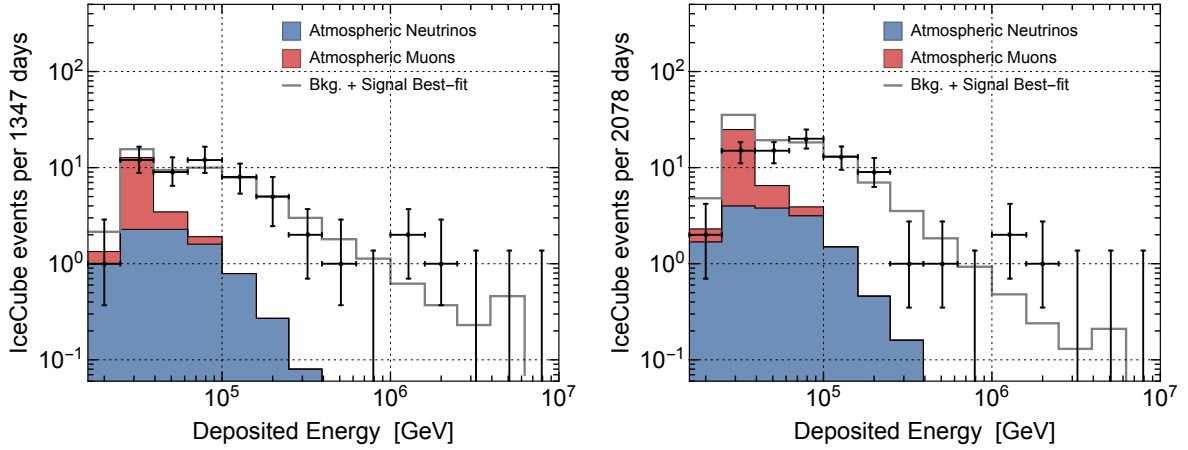
Figure 4.3: IceCube HESE neutrino events as a function of the deposited energy for 4 years (left panel) [234] and 6 years (right panel) [235] of data taking.

- **High-Energy Starting Events (HESE)**. This data set refers to neutrino events whose vertex is located inside the detector, and it has an energy threshold of $E_\nu \geq$ 20 TeV. It contains 82 events after 6 years of data taking (2010–2016) [235]. In six years of data, the expected background is 25.2 ± 7.3 muons and $16.5^{+11.4}_{-3.9}$ neutrinos. Therefore, a purely atmospheric origin of such events is rejected at more than 7σ. The HESE spectrum (number of neutrino events as a function of the deposited energy) is reported in Fig. 4.3 for 4 years (left panel) and 6 years (right panel) of data taking, respectively. The plots also show the best-fits of the single power-law flux provided in Eq. (4.10), whose spectral indexes are $\gamma_{\mathrm{IC}}^{\mathrm{HESE(4yr)}} = 2.58 \pm 0.25$ and $\gamma_{\mathrm{IC}}^{\mathrm{HESE(6yr)}} = 2.92^{+0.29}_{-0.33}$, respectively.

- **Medium-Energy Starting Events (MESE)**. This data set [186] refers to neutrino events whose vertex is located inside the detector, but differently from HESE data neutrino events can have a deposited energy as low as 1 TeV. Such a sample contains 388 events after only 2 year of observations (2010–2012). The down-going (Southern hemisphere) and up-going (Northern hemisphere) neutrino events are reported as a function of the deposited energy in Fig. 4.4. The best-fit spectral index of the astrophysical power-law is $\gamma_{\mathrm{IC}}^{\mathrm{MESE(2yr)}} = 2.46 \pm 0.12$.
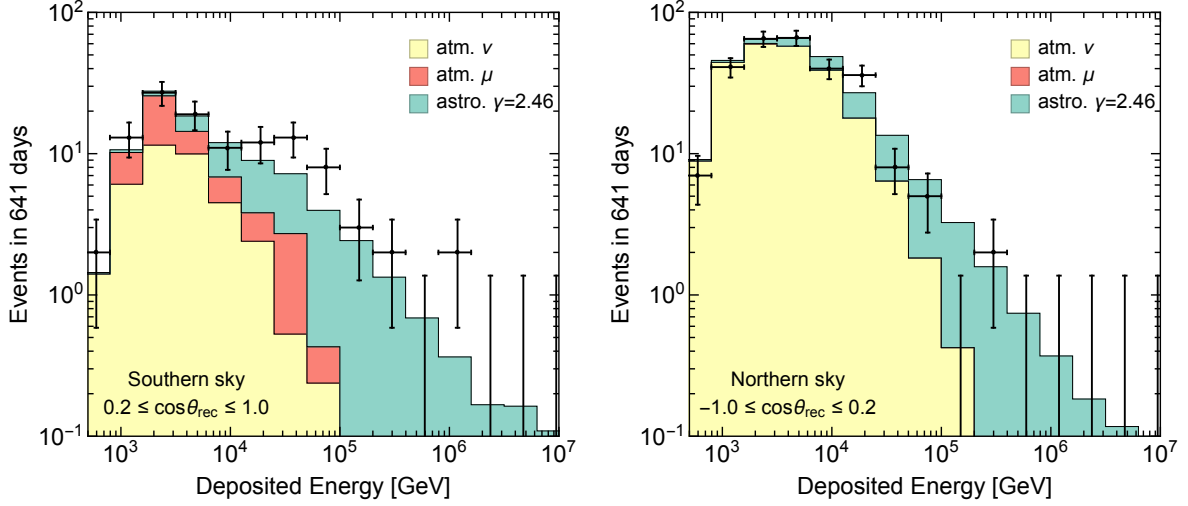
Figure 4.4: IceCube MESE neutrino events as a function of the deposited energy for 2 years of data taking [186].
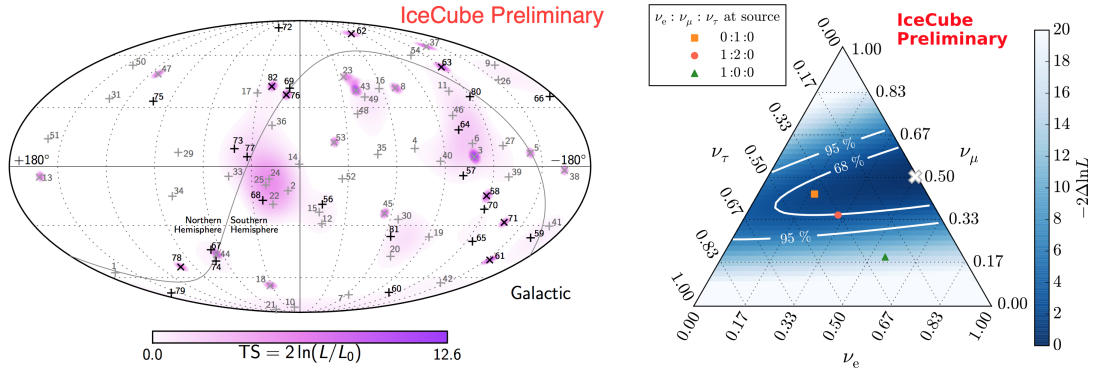
Figure 4.5: *Left*: angular distribution of arrival direction for IceCube 6-year HESE data [235]. *Right*: flavor ratio of 4-year HESE neutrino events [237].

- **Through-going muon neutrinos**. The through-going data sample [195, 236] collects up-going muons which arise from CC interactions of muon neutrinos both inside and outside the detector. The analysis is restricted to the Northern hemisphere where the Earth filters atmospheric muons efficiently. The analysis performed on the 6-year data provides a best-fit spectra index of 2.13 ± 0.13 for neutrino energies higher than about 200 TeV (the data at lower energies are dominated by the atmospheric background) [195].

In addition to neutrino spectrum, IceCube Collaboration also provides two further observables for HESE data: the neutrino sky map [235] and the measured flavor ratio [237], which are reported in Fig. 4.5 in left and right panels, respectively. The distribution of arrival direction of neutrino events is important for searches of point-like sources. No significant correlation with know sources [238, 239, 240] and with the Galactic plan [241] has been observed so far. Moreover, the measurement of the flavor ratio is of paramount importance for testing the astrophysical origin of neutrinos that predict a flavor ratio 1:1:1 at the Earth. Some exotic scenarios providing deviations from the benchmark flavor ratio have been studied in Ref.s [242, 243, 244].

4.4 ANTARES and KM3NeT experiments

The ANTARES (Astronomy with a Neutrino Telescope and Abyss environmental RESearch project) Neutrino Telescope [245] is a Cherenkov detector located at 2.5 km under the Mediterranean sea off the coast of Toulon in France. It consists of 12 strings with 75 PMTs. The ANTARES detector is placed in favored position: since it is in the Northern hemisphere, it is possible to observe the Galactic Center of the Milky Way (that is pointed towards the South Pole) with the maximal suppression of the atmospheric muon background due to the Earth's absorption. Very recently [246], the ANTARES Collaboration has released the 9-year data (shower + track) whose energy spectra are reported in Fig. 4.6. In particular 19 track-like and 14 shower-like events have been observed. This observation provides for the first time a $\sim 2\sigma$ deviation (p-value equal to 0.15) from the expected background 24 ± 7 events (13.5 track-like and 10.5 shower-like events). Indeed, all the analyses performed using the previous ANTARES data have not exhibited any significant excess over the atmospheric background [247, 248].

It is worth observing that the ANTARES detector is not big enough to have a good energy resolution for the track-like events [249]. This is why the energy of the track-like events is expressed in arbitrary units (see left panel in Fig. 4.6). On the other hand, the shower-like events inside the fiducial volume can be reconstructed with an energy resolution of about 10% [250]. The angular resolution is comparable or even better than the one of
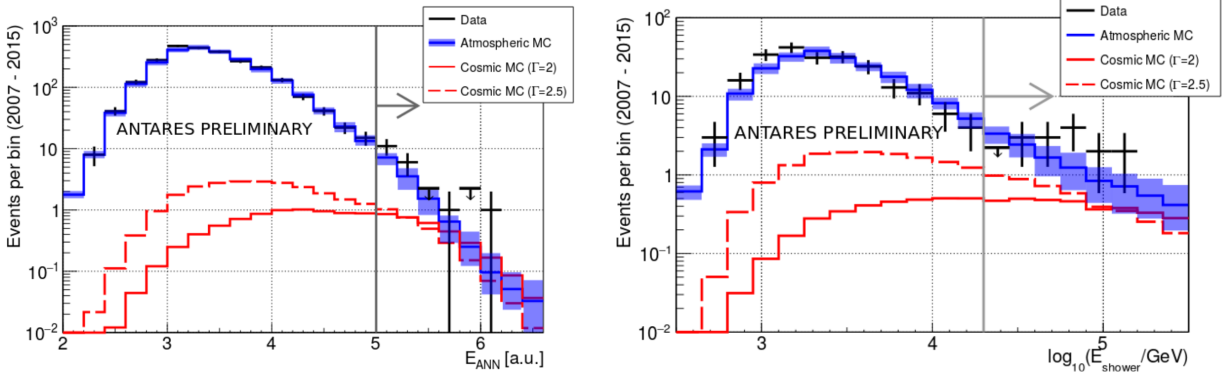
Figure 4.6: ANTARES neutrino track (left panel) and shower (right panel) events after 9-year of data taking [246].

the IceCube Neutrino Telescope. Indeed, for track-like and shower-like events a median angular resolution of 0.4° and 3° is respectively achieved [251], allowing the ANTARES Collaboration to perform detailed searches for point-sources [252].

The KM3NeT Neutrino Telescope [253] is a future Cherenkov detector devoted to Neutrino Astronomy with a fiducial volume of 1 km^3 that will upgrade the ANTARES experiment. It is under construction under the Mediterranean sea off the coast of Toulon in France and Capo Passero in Italy. The bigger fiducial volume would substantially increase the statistics of neutrino events in the Northern hemisphere.

4.5   Combined analysis with IceCube and ANTARES data

In order to constrain the parameters of the single power-law neutrino flux (see Eq. 4.10), we perform the first combined analysis of the diffuse neutrino flux observed by ANTARES (9-year) and IceCube (6-year HESE) [5]. In particular, due to the worse energy resolution, we consider only shower-like events for the ANTARES data set, whereas we take into account both tracks and showers in case of IceCube HESE data. As already discussed in the previous Sections, we consider only the conventional atmospheric background of penetrating muons and neutrinos.
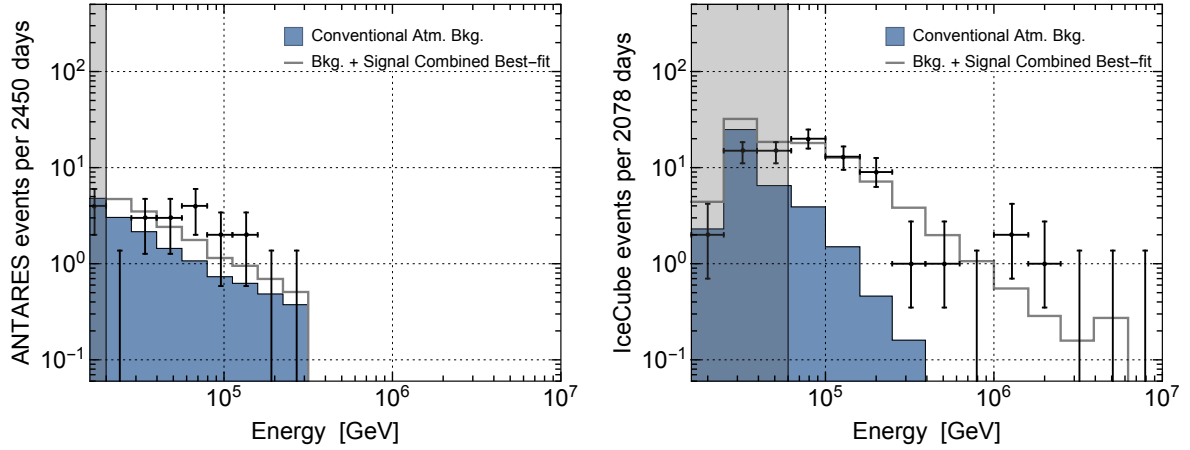
Figure 4.7: Number of neutrino events as a function of the energy for ANTARES (left panel) and IceCube (right panel). The conventional atmospheric background (neutrinos and penetrating muons) is represented by blue areas. The best-fit (signal plus background) is displayed by the gray lines. The best-fit power-law deduced by combining IceCube and ANTARES data corresponds to $\Phi^0_{astro} = 2.30 \times 10^{-18} \, (\mathrm{GeV \, cm^2 \, s \, sr})^{-1}$ and $\gamma = 2.85$.

This analysis has been performed by means of a Maximum Likelihood estimation using binned multi-Poisson likelihoods $\mathcal{L}^{A, IC}$ for both ANTARES (A) and IceCube (IC) experiments. The combined fit (IC+A) is obtained by maximizing the product of the two likelihoods

$$\ln \mathcal{L} \left(n^{IC}, n^A | \Phi^0_{astro}, \gamma \right) = \ln(\mathcal{L}^A \cdot \mathcal{L}^{IC}), \tag{4.17}$$

which is a function of the astrophysical flux normalization Φ^0_{astro} and of the spectral index γ. The quantities n^{IC} and n^A are the IceCube and ANTARES data, respectively. The expression of the multi-Poisson likelihood function is equal to [254]

$$\ln \mathcal{L} = \sum_i \left[n_i - N_i + n_i \ln \left(\frac{N_i}{n_i} \right) \right], \tag{4.18}$$

where the expected number of events N_i is compared with the observed number of neutrinos n_i, once the background events have been subtracted in each bin i. The number of events N_i that is predicted by a differential neutrino flux $\mathrm{d}\Phi_\alpha/\mathrm{d}E_\nu\mathrm{d}\Omega$ in the bin i (defined by the deposited energy range $\Delta E'_i$ and by the reconstructed solid angle $\Delta\Omega'_i$) is given by

$$N_i = \Delta t \int_{\Delta E'_i} \mathrm{d}E'_\nu \int_{\Delta\Omega'_i} \mathrm{d}\Omega' \int \mathrm{d}E_\nu \int_{4\pi} \mathrm{d}\Omega \sum_\alpha \frac{\mathrm{d}\Phi_\alpha}{\mathrm{d}E_\nu\mathrm{d}\Omega} A^{\mathrm{eff}}_\alpha \left(E_\nu, \Omega; E'_\nu, \Omega' \right), \tag{4.19}$$

where Δt is the exposure time of the experiment and the quantity A_α^{eff} is the effective area per neutrino flavor α. Such a quantity is a function of the neutrino energy E_ν, the deposited one E_ν' as well as of the angular coordinates Ω and the reconstructed ones Ω'. Moreover, the sum over neutrinos and anti-neutrinos is implicitly considered. In case of the ANTARES experiment, the exposure time is 2450 days. Its effective area has been obtained by using the two cosmic neutrino spectra reported in figure 1 of Ref. [246] assuming a constant effective area in each energy bin. The exposure time of the IceCube experiment is 2078 days, and the IceCube effective area for HESE data has been taken from Ref. [255].[1]

Moreover, we consider only neutrino events with $E_\nu \geq 20$ TeV for ANTARES and $E_\nu \geq 60$ TeV for IceCube, following the energetic cuts used by the two Collaborations. Moreover, in case of ANTARES we also consider an upper bound for the neutrino energy ($E_\nu \leq 300$ TeV) according to Ref. [246].

In Fig. 4.7 it is displayed the neutrino spectrum for ANTARES (left panel) and IceCube (right panel). In the plots, the best-fit neutrino signal (power-law) is represented by the gray lines. The total conventional background is instead displayed by the blue regions. The energetic cuts considered in the fit are shown by the shaded regions. The contour plots for the fit deduced by using only IceCube 6-year HESE (black) and for the combined fit with IceCube+ANTARES data (ocher) are shown in Fig. 4.8. The solid (dotted) lines correspond to the 68% (95%) C.L. contours, respectively. The best-fit values and the 1-2σ ranges of the flux normalization and the spectral index are obtained by marginalizing the two-dimensional likelihood and are reported in Tab. 4.1. As can be see in the table, the

---

[1]Note that the IceCube HESE effective area is public under the assumption of equality between the neutrino energy and deposited energy. In general, to statistically estimate the ratio between the deposited and neutrino energies a MonteCarlo simulation of the apparatus is required [256]. When for a bin a significant statistics is collected, one could apply an average ratio that results to be of the order of $(\sigma^{CC}\,97\% + \sigma^{NC}\,23\%)/(\sigma^{CC} + \sigma^{NC}) \sim 75\%$ (see Table 1 of [256]). Remarkably, such a number appears to be quite stable as a function of the neutrino energy. Unfortunately, due to low statistics collected till now, this procedure would be characterized by a large uncertainty in the energy determination. For this reason, in case of HESE data we prefer to assume the simplicity ansatz that the two energies coincide. Notice that in any case an expected shift in the energy of the order of 25% is not going to change dramatically the results reported in this thesis.
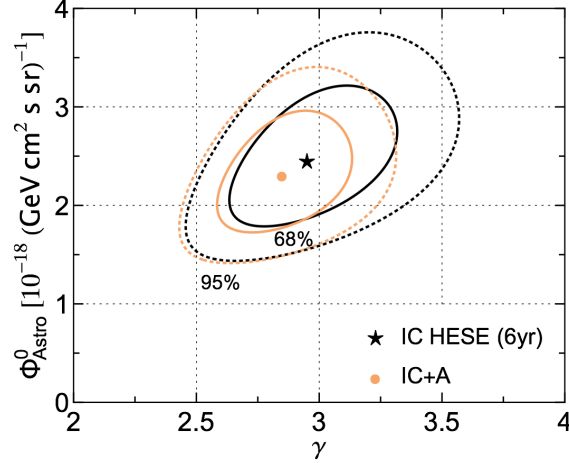
Figure 4.8: Contour plots of the likelihoods obtained by using IceCube data only (black) and the combined IceCube+ANTARES ones (ocher).

Fit	Parameter	Best-fit	68% C.I.	95% C.I.
IceCube	$\Phi^0_{\rm astro}$	2.44	$2.00 - 2.94$	$1.62 - 3.48$
	γ	2.95	$2.76 - 3.21$	$2.56 - 3.46$
IceCube + ANTARES	$\Phi^0_{\rm astro}$	2.30	$1.90 - 2.71$	$1.56 - 3.16$
	γ	2.85	$2.68 - 3.04$	$2.52 - 3.23$

Table 4.1: Best-fit values and 1–2σ intervals of $\Phi^0_{\rm astro}$ (in units of $10^{-18}\,({\rm GeV\,cm^2\,s\,sr})^{-1}$) and γ for the analysis on IceCube 6-year HESE data and the combined analysis IceCube+ANTARES.

best-fit values for the spectral index and the flux normalization, obtained by using IceCube data only, differ from the ones reported by the IceCube Collaboration by 1% and 0.8%, respectively. Moreover, we note that the addition of ANTARES data in this fit provides slightly smaller values for the flux normalization $\Phi^0_{\rm astro}$ and the spectral index γ.

4.6 Tension with the single power-law flux

In this last Section, we comment about the simplest assumption that the whole diffuse TeV–PeV neutrino flux can be interpreted in terms of a single astrophysical power-law. In

Data sample	Best-fit	
	Normalization $\Phi^0_{\mathrm{astro}} \left[10^{-18} \, (\mathrm{GeV \, cm^2 \, s \, sr})^{-1} \right]$	Spectral index γ
MESE (2yr) [186]	$2.06^{+0.4}_{-0.3}$	$2.46^{+0.12}_{-0.12}$
HESE (3yr) [238]	1.50	$2.30^{+0.3}_{-0.3}$
HESE (4yr) [234]	$2.20^{+0.7}_{-0.7}$	$2.58^{+0.25}_{-0.25}$
HESE (6yr) [235]	$2.46^{+0.8}_{-0.8}$	$2.92^{+0.29}_{-0.3}$
Through-going ν_μ (6yr) [195]	$0.90^{+0.30}_{-0.27}$	$2.13^{+0.13}_{-0.13}$
IceCube combined analysis [257]	$2.23^{+0.37}_{-0.30}$	$2.50^{+0.09}_{-0.09}$
IceCube + ANTARES [5]	$2.30^{+0.86}_{-0.74}$	$2.85^{+0.38}_{-0.33}$

Table 4.2: Best-fit values for the flux normalization and the spectral index of the power-law behavior, obtained by considering different data samples of the diffuse TeV-PeV neutrino flux.

Tab. 4.2, we report the best-fit values of the flux normalization Φ^0_{astro} and the spectral index γ deduced by different data samples. We note some interesting trends and features.

- The best-fit flux normalizations deduced by IceCube HESE data with different exposures are compatible among themselves, while the best-fit values for spectral index show an increasing trend with time. This is explained by the fact that IceCube detector has observed only three PeV events, while it is enlarging only the statistics at low energy. For instance, the 28 events observed between 2014 and 2016 (difference between 82 events in 6-year HESE and 54 events in 4-year HESE) have all a deposited energy lower than 200 TeV. It is worth observing that the anomalous large values $\gamma^{\mathrm{HESE(4yr)}}_{\mathrm{IC}}$ and $\gamma^{\mathrm{HESE(6yr)}}_{\mathrm{IC}}$ for the spectral index can be hardly reconciled with the multi-messenger constraints on models for realistic astrophysical sources.

- The through-going muon neutrino data sample favors a smaller value for the spectral index. Such a best-fit value is compatible with the benchmark prediction $\gamma = 2.0$ of the Fermi acceleration mechanism and the allowed values for the spectral index ($\gamma \leq 2.2$) deduced by gamma-ray constraints and models for p-p astrophysical sources.

It is worth noticing that such a best-fit for the spectral index is in a 3.3σ tension with the one obtained by combing different IceCube data samples [257]. Moreover, this data set strongly suggests the presence of an *asymmetry* between the Northern and the Southern neutrino fluxes, once it is compared with the other data sets. We remind that through-going muon neutrinos come only from the Northern hemisphere (up-going neutrinos). Therefore, the mismatch among the best-fit values for the spectral index of this data sample and of the other IceCube data ones points out that a new contribution to the neutrino flux is required at low energies ($E_\nu \leq 200\,\text{TeV}$). Moreover, the origin of such a new component may be galactic according to the North-South asymmetry.

- The spectral index obtained by including the ANTARES data in the fit is slightly smaller, while the flux normalization is compatible with the other best-fit values. This is due to the fact that the ANTARES data set mainly favors a spectral index close to the benchmark Fermi value.

These statements point out that there exists a tension of the IceCube andANTARES data with the simplest assumption of a single power-law neutrino flux (*null hypothesis*). In order to statistically quantify this tension, we perform a χ^2 test. For Poisson distributed data, the test statistics behaving as a χ^2 with $N - m$ d.o.f. is given by

$$\chi^2 = -2\ln\mathcal{L}\left(n^{\text{IC}}, n^{\text{A}}|\Phi^0_{\text{astro}}, \gamma\right) , \tag{4.20}$$

where $\mathcal{L}\left(n^{\text{IC}}, n^{\text{A}}|\Phi^0_{\text{astro}}, \gamma\right)$ is defined in Eq. (4.17). In the case under study (IceCube+ANTARES combined fit), $N = 18$ is the total number of energy bins. Since the statistical test is performed by fixing the spectral index γ to some specific values and by fitting the flux normalization Φ^0_{astro}, the number of free parameters in the fit is $m = 1$. However, since the χ^2 analysis has to be performed when the events of each bin are Gaussian distributed, condition that in principle could not be satisfied for small number of events, we additionally perform a more general non-parametric test, namely the one-dimensional Kolmogorov-Smirnov (KS) statistical test, which will be discussed in detail in the next Chapter. For each experiment, the test compares the empirical cumulative distribution function deduced by data with the
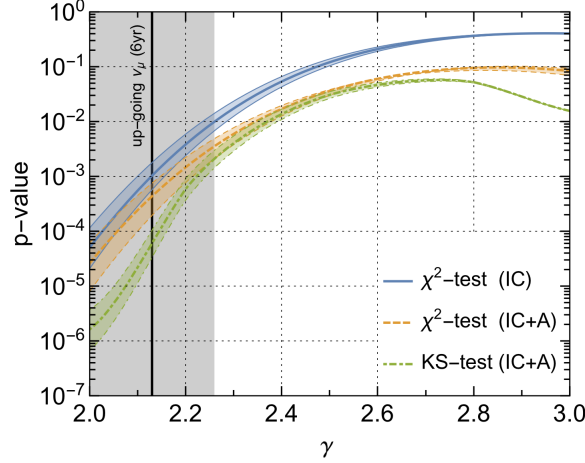
Figure 4.9: The solid (dashed) line represents the p-value as a function of the spectral index for the χ^2-test for the IC (IC+A) data sample. The dot dashed line refers to the KS-test performed by combining the two data samples with the Fisher's method. The bands correspond to an uncertainty of $\pm 20\%$ on the conventional background estimation. The vertical band, instead, represents the best-fit for the spectral index as deduced by 6-year up-going muon neutrinos ($\gamma = 2.13 \pm 0.13$) [195].

one obtained under the null hypothesis of power-law behavior. For a given spectral index, the p-value is evaluated by a bootstrap method for IceCube and ANTARES experiments, respectively. The two p-values are then combined by means of the Fisher's method.

The results of the hypothesis tests are reported in Fig. 4.9. The plot shows the p-value for the null hypothesis as a function of the spectral index adopted in the analysis. The solid line corresponds to the χ^2 test performed by considering only the IceCube 6-year HESE data. While the dashed line represents the p-values for the combined analysis with IceCube and ANTARES data. The dot dashed line instead refers to the KS test. The bands are obtained by considering an uncertainty of $\pm 20\%$ on the conventional background estimation in both experiments. The addition of ANTARES data set has the effect to reduce the p-values by about a factor $2 \div 3$, independently of the assumed spectral index. This implies that if one fix a certain threshold in p-value for rejecting the null hypothesis, the addition of the ANTARES to the fit enlarges the range of spectral indexes for which the null hypothesis can be rejected. In particular, the benchmark prediction of Fermi acceleration mechanism

$\gamma = 2.0$ is excluded, since it corresponds to a p-value equal to $2.6^{+3.6}_{-1.8} \times 10^{-5}$ for χ^2 and $1.6^{+2.1}_{-1.0} \times 10^{-6}$ for KS statistical tests, where the errors correspond to a $\pm 20\%$ uncertainty on the conventional atmospheric background. Moreover, the interpretation of the whole data sample with a single power-law according to the 6-year through-going muon neutrinos is strongly disfavored (p-value smaller than 10^{-2}).

Such a tension with the single power-law scenario is currently under debate. Nevertheless, the theoretical prior of a single astrophysical power-law component with a spectral index dictated by the Fermi acceleration mechanism suggests the presence of a second component dominating the diffuse neutrino flux for energies lower than 200 TeV. Such an additional component can be an another power-law as studied in Ref.s [235, 258, 259, 260, 261, 262]. Viable astrophysical candidates for the large neutrino flux observed at about 100 TeV are the "hidden" astrophysical sources [231, 232, 233], since these kinds of sources are not constrained by gamma-ray and radio observations. On the other hand, the second component at 100 TeV can be also related to DM that could produce a neutrino flux through its annihilations or decays [1, 2, 3, 4, 6]. This interesting scenario is presented and studied in detail in the next two Chapters.

Chapter 5

The low-energy excess: a DM interpretation

In the previous Chapter, we have noted that different IceCube data samples are in tension with the interpretation of the diffuse TeV–PeV neutrino flux in terms of a single astrophysical power-law. Such a tension is also strengthened once the ANTARES 9-year shower data are included in the analysis. In particular, we underline that, according to the multi-messenger constraints and with the fit of through-going muon neutrinos, the fully compatible astrophysical models are represented by a power-law with a spectral index γ in the range $[2.0, 2.2]$. Once a hard power-law is assumed, a *low-energy excess* around 100 TeV is shown in the neutrino data. Fig.s 5.1 and 5.2 display the residual in the number of neutrino events once the sum of a hard astrophysical power-law (γ equals to 2.0 or 2.2) and the standard conventional atmospheric background is subtracted. In particular, the black points in the plots of Fig. 5.1 refer to the analysis performed by using the IceCube 6-year HESE data, in case of a spectral index $\gamma = 2.0$ (left panel) and $\gamma = 2.2$ (right panel). The gray points instead corresponds to the residuals obtained with IceCube 4-year HESE events. On the other hand, in Fig. 5.2 we report the residual in the number of neutrino events in case of the IceCube 2-year MESE data for $\gamma = 2.0$ (upper panels) and $\gamma = 2.2$ (lower panels). We remind that this data set is further divided into neutrino events coming from the Southern hemisphere (left panels) and the Northern one (right panels). Remark-
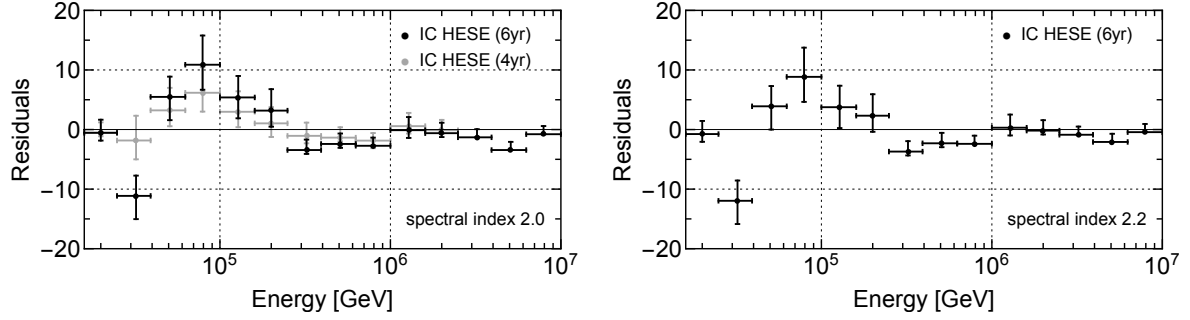
Figure 5.1: Residuals in the number of neutrino events as a function of the neutrino energy with respect to the sum of the conventional atmospheric background and a single astrophysical power-law with spectral index 2.0 (left panel) and 2.2 (right panel). The black (gray) points refer to IceCube 6-year (4-year) HESE data.

ably, the low-energy excess highlighted in the IceCube observations is also shown in the ANTARES 9-year data sample as can be seen in Fig. 5.3.

Data sample	Maximum Local Significance	
	$\gamma = 2.0$	$\gamma = 2.2$
IceCube MESE (2yr)	2.3 σ	1.9 σ
IceCube HESE (4yr)	~ 2 σ	$-$
IceCube HESE (6yr)	2.6 σ	2.1 σ

Table 5.1: Maximum local statistical significance of the low-energy excess for different IceCube data samples.

It is worth underlining the presence of an excess between about 40 and 200 TeV in all the data samples. The *maximum local* statistical significance of such a low-energy excess is reported in Tab. 5.1. We observe that the statistical significance of the low-energy excess increases from 4 years to 6 years of data taking in case of HESE sample. Moreover, the excess shown in the IceCube 2-year MESE data has a larger significance with respect to the one of the IceCube 4-year HESE data, since the former data set has a large sensitivity at low energies due to the different veto implementation.

Under the assumption that such an excess has a genuine physical origin, we pursue a
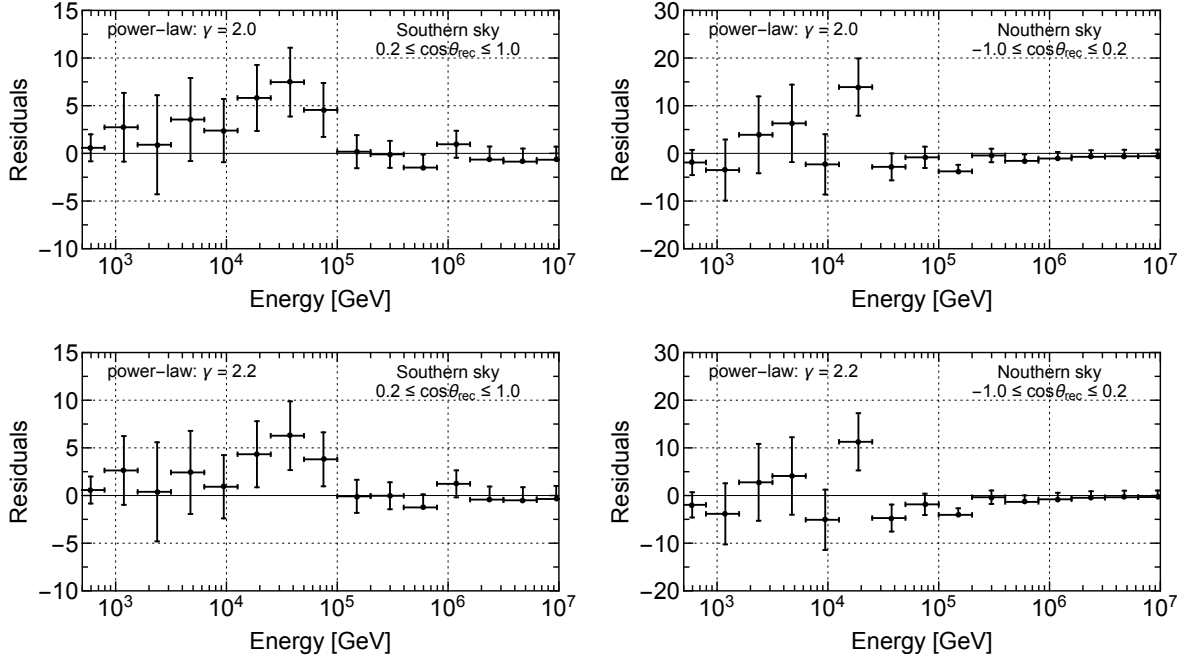
Figure 5.2: Residuals in the number of neutrino events for the IceCube 2-year MESE data, which are divided into Southern (upper panels) and Northern (lower panels) hemisphere.
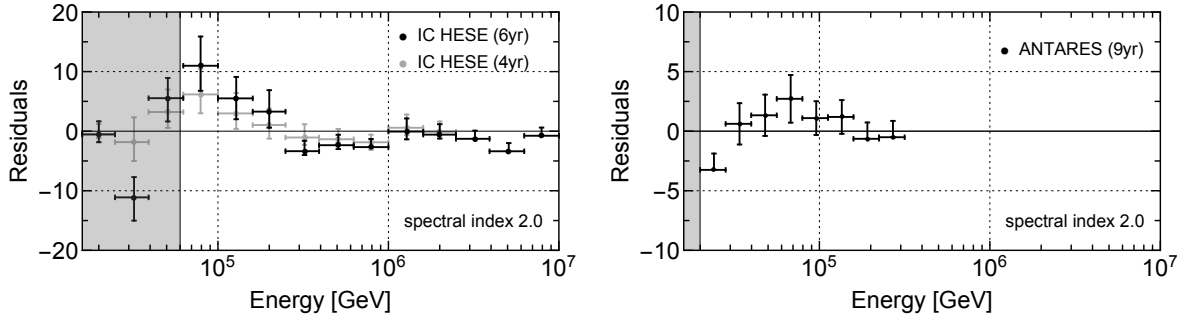
Figure 5.3: Residuals in the number of neutrino events obtained by combining the IceCube 6-year HESE data and the ANTARES 9-year ones for a power-law with $\gamma = 2.0$. The shaded regions represent the low energy cuts adopted in the fit procedure.

study in order to unveil the nature of the low-energy excess. The Chapter is divided into two Sections. In the first, we report the study based on the angular distribution of the observed neutrinos, while in the second we discuss the statistical analysis performed on the energy spectrum by using different IceCube data samples. The constraints coming from gamma-rays observations are also discussed.

5.1   Analysis on the angular distribution

In order to analyze the origin of the low-energy excess, we firstly compare the angular distribution of the observed events with the angular distributions expected in case of astrophysical sources (galactic and extragalactic sources) and DM signal (both decaying and annihilating cases). This angular analysis is performed by using the IceCube 4-year HESE data, where the excess is concentrated in the energy bin 60–100 TeV. Due to the small number of events collected till now in the energy bin under study, for the sake of simplicity we consider just one additional component to explain the excess, on top of the conventional atmospheric background and of the astrophysical E^{-2} power-law. This allows us to be more predictive even though more involved scenarios can be proposed where the diffuse neutrino flux can be explained in terms of several components of different origin. Differently from previous angular analyses [263, 264], we also take into account the angular efficiency of the IceCube detector for all neutrino flavors through the expression provided in Eq. (4.19).[1] The IceCube HESE effective area, normalized and averaged in the energy range considered (60–100 TeV), is depicted in Fig. 5.4 as a function of the sine of the declination δ. We note that the effective area decreases in the Northern hemisphere ($\sin \delta > 0$) due to the Earth's absorption. In the Southern hemisphere ($\sin \delta < 0$), only the effective area for muon neutrinos (green line) is slightly dependent on the declination.

As already stated, we consider different scenarios for the low-energy excess. In the following, we report the expected neutrino angular distributions for all the cases considered, without explicitly considering the IceCube effective area, which is instead taken into account for the real analysis.

- **Galactic astrophysical sources (gal)**. For Galactic astrophysical sources, a correlation with the Galactic plane is expected. Therefore, the angular distribution of galactic astrophysical sources in the arrival directions (Galactic latitude b and Galactic longitude l) is given by

$$p^{\mathrm{gal}}(\sin b, l) = \frac{\Theta(\sin b + \sin b_{\mathrm{gal}}) - \Theta(\sin b - \sin b_{\mathrm{gal}})}{4\pi \sin b_{\mathrm{gal}}} \; . \tag{5.1}$$

---

[1]The IceCube HESE effective area is available at `http://icecube.wisc.edu/science/data/HE-nu-2010-2012`.
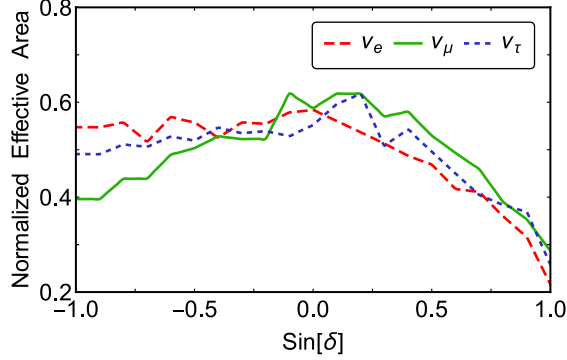
Figure 5.4: Normalized IceCube effective area for HESE data set as function of the declination δ, averaged in the energy range 60–100 TeV.

We note that the galactic plane angular distribution depends only on the Galactic latitude and on the angular size of the Galactic disk, denoted as b_{gal}. Such a quantity can be derived by assuming that the neutrinos and gamma-rays produced by galactic astrophysical sources have the same galactic angular distribution [265]. We adopt the Fermi-LAT template [266], implying that the quantity b_{gal} varies in the range $[2°, 4°]$.

- **Extragalactic astrophysical sources (iso)**. Extragalactic sources are isotropically distributed in the Galactic angular coordinates. Therefore, their angular distribution is isotropic, meaning that it is simply a constant.

$$p^{\text{iso}}(\sin b, l) = \frac{1}{4\pi} \, . \tag{5.2}$$

- **Decaying DM scenario (dec)**. According to Eq. (3.1), the resulting neutrino flux consists of both a galactic and an extragalactic DM component. As shown in Eq.s (3.3) and (3.4), the neutrino flux depends on the neutrino energy spectrum dN/dE_ν produced by the decay of a DM particle. Since the excess is localized in a particular energy range 60–100 TeV, for this angular analysis we simply assume that the neutrino energy spectrum is almost peaked in the same range. This is equivalent to assume that neutrino energy spectrum for $E_\nu \geq 100$ TeV is negligible. In other words, we consider the case of a DM mass of the order of 100 TeV. We observe that a not vanishing neutrino energy spectrum for energy smaller that 60 TeV does not

provide any contribution neither to the galactic component nor to the extragalactic one for the energy bin considered. Under this assumption, the redshift integral appearing in the extragalactic component has an upper limit that corresponds to $z_{\max} = 100\,\mathrm{TeV}/60\,\mathrm{TeV} - 1$. The quantity $z_{\max}$ is obtained by considering the relation $E' = E\,(1+z)$ when the conditions $E' \leq 100\,\mathrm{TeV}$ and $60\,\mathrm{TeV} \leq E \leq 100\,\mathrm{TeV}$ are applied. After the integration on the redshift, the extragalactic component given in Eq. (3.4) can be recast in the following approximated expression

$$
\frac{\mathrm{d}\Phi_{\mathrm{DM}}^{\mathrm{EG}}}{\mathrm{d}\Omega} \simeq \frac{\Omega_{\mathrm{DM}}\rho_c}{4\pi m_{\mathrm{DM}}\tau_{\mathrm{DM}}} \int_0^{z_{\max}} \frac{\mathrm{d}z}{(1+z)H(z)}
$$
$$
\times \left\{ \int_{E_{\min}}^{E_{\max}} \mathrm{d}E_\nu \frac{\mathrm{d}N}{\mathrm{d}E_\nu} + \left[\left.\frac{\mathrm{d}N}{\mathrm{d}E_\nu}\right|_{E_{\max}} E_{\max} - \left.\frac{\mathrm{d}N}{\mathrm{d}E_\nu}\right|_{E_{\min}} E_{\min} \right] z \right\} , \tag{5.3}
$$

where $E_{\min} = 60$ TeV and $E_{\max} = 100$ TeV. This expression has two interesting limits: *i)* the neutrino energy spectrum is fully contained in the energy bin considered, then $\mathrm{d}N/\mathrm{d}E_\nu\,(E_{\min}) \simeq \mathrm{d}N/\mathrm{d}E_\nu\,(E_{\max}) \simeq 0$; *ii)* the neutrino energy spectrum is wider than the energy bin, hence it is flat within the energy range 60–100 TeV, implying $\mathrm{d}N/\mathrm{d}E_\nu\,(E_{\min}) \simeq \mathrm{d}N/\mathrm{d}E_\nu\,(E_{\max})$. In these two cases, the dependence on the neutrino energy spectrum can be factorized (as in case of the galactic DM component). Therefore, the previous reasonable assumption considerably simplifies the calculations that are now independent on the particular decay channel of DM particles. Hence, we arrive to the following expression for the angular distribution

$$
p^{\mathrm{dec}}(\cos\theta) \propto \int_0^\infty \rho_h[r(s,\cos\theta)]\mathrm{d}s + \Omega_{\mathrm{DM}}\rho_c\,\beta_\alpha , \tag{5.4}
$$

where

$$
\beta_\alpha = \int_0^{z_{\max}} \frac{\mathrm{d}z}{(1+z)^\alpha H(z)} , \tag{5.5}
$$

whit $\alpha = 1$ and 0 in the first and second cases respectively. Hence, we have $\beta_1 = 0.43/H_0$ and $\beta_0 = 0.56/H_0$. In order to obtain more conservative results, we consider the larger extragalactic contribution that corresponds to $\alpha = 0$. In such a case, the isotropic cosmological contribution results to be more competitive with the galactic term. It is worth observing that including explicitly the IceCube effective area in the above calculations does not change this result, and the case with $\alpha = 0$ still represents the most conservative scenario.

- **Annihilating DM scenario (ann)**. Following the same steps for the case of decaying DM, in this case we similarly obtain

$$p^{\mathrm{ann}}(\cos\theta) \propto \int_0^\infty \rho_h^2[r(s,\cos\theta)]\mathrm{d}s + (\Omega_{\mathrm{DM}}\rho_c)^2\,\Delta_0^2\,\beta_\alpha\,, \qquad (5.6)$$

  where Δ_0^2 is the clumpiness factor [170]. According to Ref. [171], we analyze three particular and extreme cases where where Δ_0^2 is equal to 10^4, 10^6 and 10^8. Such three values for the clumpiness factor correspond to an extragalactic contribution that is sub-dominant, comparable and dominant with respect to the galactic one, respectively. However, as pointed out in Ref. [267], the cumpliness factor Δ_0^2 can be as large as few times 10^6, while larger values are considered unphysical.

Independently of the mass and the couplings of DM, neutrinos originated via decay or annihilation would have an angular distribution that is more peaked around the Galactic Center where a higher DM density ρ_h is expected. This is in particular true for annihilating DM scenario (in case of small clumpiness factor) where the galactic flux is enhanced due to second power of the DM density profile adopted. Here, we consider the two extreme cases of the Navarro-Frenk-White profile (NFW) and the Isothermal profile, as representative of all the parametrization for ρ_h.

In all the listed scenarios, the angular distributions depend on one angle only. Therefore, we perform a *one-dimensional* statistical test under the *null hypothesis* that neutrino events are distributed according to one of the four angular distributions previously discussed. We adopt two different *non-parametric* statistical tests: the Kolmogorov-Smirnov test (KS) [268] and the Anderson-Darling test (AD) [269]. These statistical tests compare the cumulative distribution function (CDF) of the null hypothesis with the empirical cumulative distribution function (EDF), which takes the expression

$$\mathrm{EDF}(\cos\theta) = \frac{1}{n}\sum_{i=1}^n \Theta\left(\cos\theta - \cos\theta_i\right)\,, \qquad (5.7)$$

where n is the number of observed events with directions $\cos\theta_i$ (or $\sin b_i$ for the galactic plane angular distribution). In the Kolmogorov-Smirnov test, the Test Statistics (TS) is the maximum distance between the previous two cumulative distribution functions. Hence,

we have

$$\text{TS}_{\text{KS}} \equiv \sup_\theta \left| \text{EDF}(\cos\theta) - \text{CDF}(\cos\theta) \right| . \tag{5.8}$$

The Test Statistics of Anderson-Darling test is instead given by

$$\text{TS}_{\text{AD}} \equiv -n - \frac{1}{n} \sum_{i=1}^{n} (2i-1) \left[\ln\left(\text{CDF}(\cos\theta_i)\right) + \ln\left(1 - \text{CDF}(\cos\theta_{n+1-i})\right) \right] . \tag{5.9}$$

Since this expression is very sensitive to the difference between the functions EDF and CDF at the two endpoints ($\cos\theta = 1$ corresponds to the Galactic Center), the Anderson-Darling test is a very suitable test for such an analysis.

In oder to take into account the fact that five of the twelve events correspond to the sum of the conventional atmospheric background and of the astrophysical E^{-2} power-law, we consider all possible different choices of 5 among 12, namely $12!/(5!\,7!) = 792$ combinations. Moreover, in order to include the angular uncertainty affecting the reconstruction of the arrival direction, we treat the uncertainties on declination and right ascension as maximum errors, and propagate them on the quantity $\cos\theta$. Such an angular uncertainty is included in the analysis by performing a Monte Carlo by considering 100 possible extractions of the 7 remaining events from their maximum error intervals using a uniform probability. For all the 100 different choices of observed events, we evaluate the corresponding TS values. In this way, we obtain a range of p-values once the TS values are compared with the null hypothesis TS distribution. Such a range is finally averaged on the 792 different background combinations. In Tab. 5.2 it is reported such an average range for each test performed. The IceCube 4-year HESE data show that a correlation with the galactic plane is disfavored. The corresponding p-value range does not significantly change by varying the angular size b_{gal} in the range $[2°, 4°]$. Moreover, the annihilating DM scenario with a small clumpiness factor ($\Delta_0^2 = 10^4$) is already excluded by the IceCube observations for both the halo density profiles. We note that for a largest clumpiness factor considered ($\Delta_0^2 = 10^8$) we obtain p-value ranges similar to the ones of the astrophysical isotropic distribution. This is explained by fact that in this case the angular distribution is almost isotropic (the extragalactic component dominates over the galactic one). Furthermore, it is worth observing that the lack of events from the Galactic Center implies that the NFW profile is more in tension with the observations than the Isothermal profile. Indeed the former is

Scenario		KS	AD
Astrophysics	Galactic plane	$0.007 \div 0.008$	not defined
	Isotropic distribution	$0.20 \div 0.55$	$0.17 \div 0.54$
DM decay	NFW	$0.06 \div 0.16$	$0.03 \div 0.14$
	Isothermal	$0.08 \div 0.22$	$0.05 \div 0.19$
DM annihilation $\Delta_0^2 = 10^4$	NFW	$(0.3 \div 0.9) \times 10^{-4}$	$(0.3 \div 3.8) \times 10^{-4}$
	Isothermal	$(0.9 \div 2.8) \times 10^{-3}$	$(1.0 \div 5.0) \times 10^{-3}$
DM annihilation $\Delta_0^2 = 10^6$	NFW	$0.02 \div 0.05$	$0.02 - \div 0.07$
	Isothermal	$0.10 \div 0.28$	$0.08 \div 0.29$
DM annihilation $\Delta_0^2 = 10^8$	NFW	$0.19 \div 0.54$	$0.17 \div 0.53$
	Isothermal	$0.20 \div 0.55$	$0.17 \div 0.54$

Table 5.2: The p-values ranges for all the four analyzed scenarios, using the Kolmogorov-Smirnov and the Anderson-Darling statistical tests. The Anderson-Darling test is not well defined in case of the galactic plane distribution since its CDF is vanishing within the region $b < b_{\text{gal}}$.

more peaked towards the Galactic Center than the latter. This results in smaller p-values for NFW density profile with respect to Isothermal one. Moreover, such a difference is exacerbated for annihilating DM scenario.

Since the small number of events already observed does not allow to exclude all the DM scenarios, we perform a *forecast* analysis. The aim is to quantify the statistics required (number of events) in order to distinguish, at a certain confidence level, a DM distribution from an isotropic one (extragalactic astrophysical sources). We restrict the forecast analysis to decaying DM scenario and annihilating DM one with $\Delta_0^2 = 10^6$. Both scenarios are not already excluded by the IceCube data. For a given number of events, we generate 10^5 sets of data (in the 60–100 TeV energy range) according to the isotropic distribution, and perform the two statistical tests under null hypothesis that the data samples come from one of the two DM angular distribution. For the sake of simplicity, we assume that each data sample is not affected by the background. The effect of the background effect can be included by
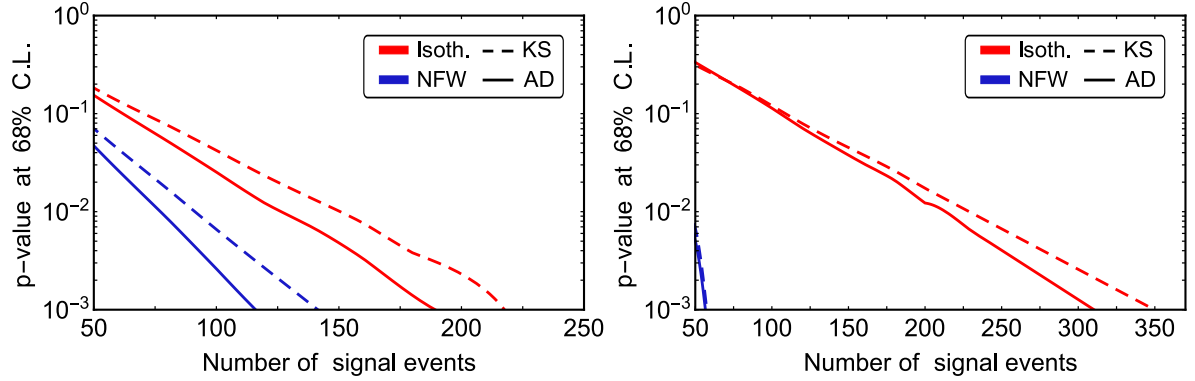
Figure 5.5: Forecast analysis in case of decaying (left panel) and annihilating (right panel) DM scenarios, for NFW (blue) and Isothermal (red) halo density profiles. The solid (dashed) lines are obtained by performing the Anderson-Darling (Kolmogorov-Smirnov) statistical test.

increasing our "predictions" by a factor of $\sim 12/7$ as suggested by present data.

A distribution of p-values is then obtained by varying in the set of 10^5 data samples. In Fig. 5.5 we show the p-value at 68% C.L. of that distribution as a function of the number of signal events (no background) in case of decaying (left panel) and annihilating (right panel) DM scenarios. The p-value at 68% C.L. represents the upper bound for p-values in 68% of cases. As already discussed, the Anderson-Darling statistical test (solid lines) is more appropriate for such an analysis than the Kolmogorov-Smirnov one (dashed lines). In fact, the p-value falls down to zero very rapidly. If we assume that the p-value required to exclude a model is $\mathcal{O}(10^{-3})$, then we have that the decaying (annihilating) case will be completely excluded only when a $\mathcal{O}(200)$ ($\mathcal{O}(300)$) number of signal events is collected in the energy bin of the low-energy excess. However, since the NFW density profile is more spatially concentrated around the Galactic Center, such a case requires a smaller number of signal events, namely $\mathcal{O}(100)$, to be excluded with respect to the Isothermal profile.

5.2   Analysis on the energy spectrum

We also characterize the low-energy excess by performing an analysis on the observed neutrino spectrum (neutrino events as a function of the energy). In particular, we assume that the diffuse TeV–PeV neutrino flux is explained in terms of the standard conventional atmospheric background (neutrinos and penetrating muons) and of two additional components: the first is originated by astrophysical sources (hard power-law with $\gamma = 2.0, 2.2$), whereas the second is given by decaying/annihilating DM particles. Under this ansatz, the total differential flux of extraterrestrial neutrinos at the Earth, at a given energy E_ν, per flavour α and per unit solid angle Ω, is equal to

$$\frac{\mathrm{d}\Phi_\alpha}{\mathrm{d}E_\nu \mathrm{d}\Omega} = \frac{\mathrm{d}\Phi_\alpha^{\mathrm{astro}}}{\mathrm{d}E_\nu \mathrm{d}\Omega} + \frac{\mathrm{d}\Phi_\alpha^{\mathrm{DM}}}{\mathrm{d}E_\nu \mathrm{d}\Omega} \, , \tag{5.10}$$

The first term is an astrophysical unbroken power-law according to Eq. (4.10), while the second one is related to DM and its expression is provided in Section 3.1. In order to cover all the possible phenomenological DM scenarios, we consider the two different and quite extreme halo density profile: the Navarro-Frenk-White and the Isothermal distributions. Moreover, we examine different decay/annihilation channels (only one channel at a time, with branching ratio equal to unity) of DM particles χ into SM, which have different features for the neutrino energy spectrum at the source $\mathrm{d}N/\mathrm{d}E_\nu$. In particular, we study:

- $\boldsymbol{\chi \to f\overline{f}}$. A bosonic DM particle that decays into a SM fermion and its anti-fermion. The SM fermions could be quarks ($\chi \to t\bar{t}$ or $\chi \to b\bar{b}$) or leptons ($\chi \to \mu^-\mu^+$ or $\chi \to \tau^-\tau^+$).

- $\boldsymbol{\chi \to \ell^-\ell^+\nu}$. A fermionic DM particle couples only to charged leptons and neutrinos (*leptophilic* DM).[2] This channel has two intriguing features: *i)* since it is a three-body decay, the neutrino energy spectrum is spread differently from the case of two-bodies decays; *ii)* the absence of quarks in the final states provides a peaked neutrino spectrum for energies close to the DM mass.

---

[2]In the next Chapter we will present a complete model that provides this leptophilic coupling and accounts for the DM production in the early Universe as well.

- $\chi\chi \to f\overline{f}$. Two fermionic stable DM particles that annihilate into SM ones with $f = b, t, \mu, \tau$.

In order to statistically quantify how much the IceCube observations are in favor of a two-component neutrino flux, where one component is related to DM, we perform a likelihood-ratio statistical test. In particular, we adopt the Test Statistics (TS) given by

$$\text{TS} = 2\ln\frac{\mathcal{L}\left(\Phi^0_{\text{astro}}, \Phi^0_{\text{DM}} \neq 0\right)}{\mathcal{L}\left(\Phi^0_{\text{astro}}, \Phi^0_{\text{DM}} = 0\right)}, \tag{5.11}$$

where Φ^0_{astro} is the normalization of the astrophysical power-law, whereas Φ^0_{DM} is the normalization of the DM signal. We have $\Phi^0_{\text{DM}} = 1/\tau_{\text{DM}}$ and $\Phi^0_{\text{DM}} = \langle\sigma v\rangle$ in case of decaying and annihilating DM, respectively. The likelihood function $\mathcal{L}$ is the binned multi-Poisson likelihood defined in Eq. (4.18).

We perform the likelihood-ratio statistical test by fixing the DM model (defined by the choice of final states and DM mass m_{DM} in the range 10 TeV–10 PeV)[3] and the spectral index γ of the astrophysical contribution. For each choice of the spectral index ($\gamma = 2.0, 2.2$), the flux normalization Φ^0_{astro} is always fixed at its best-fit through a maximum-likelihood procedure. Then, we scan over the only reaming free parameter Φ^0_{DM}. The quantity ϕ^{Astro}_0 is always fixed at the best-fit for the two values of the spectral index considered ($\gamma = 2.0, 2.2$).

According to the Wilks [274] and the Chernoff [275] theorems, the Test Statistics follows the distribution

$$\frac{1}{2}\delta\left(\text{TS}\right) + \frac{1}{2}\chi^2\left(\text{TS}\right), \tag{5.12}$$

through which we can evaluate the number of standard deviations σ from the expected value $\text{TS} = 0$. Deviation from such a value indeed would show the preference of the data for a two-component flux (astrophysical plus DM fluxes) with respect to the single astrophysical power-law. The larger the number of standard deviations σ, more likely the presence of a second component related to DM. A similar analysis was performed for searches of DM gamma-lines in the Fermi-LAT spectrum [276], and very recently it has been proposed to characterize the significance of DM neutrino-lines in IceCube [160].

---

[3]We focus on DM masses larger than 10 TeV in order to explain the low-energy excess. Bounds on decaying DM signals for $m_{\text{DM}} \leq 10$ TeV are provided in Ref. [270]. The bounds for the annihilating DM scenarios with $m_{\text{DM}} \leq 10$ TeV are provided in Refs. [271, 272, 273].

5.2.1   Gamma-ray constraints

As discussed in Chapter 3, in all the decaying/annihilating channels considered, there is also the production of primary photons, electrons and positrons. The charged particles produce secondary photons through inverse Compton scatterings on the intergalactic radiation like the CMB. Moreover, the primary photon spectrum is degraded in energy due the interactions occurring during the propagation. These processes would provide a photon spectrum in the GeV–TeV energy range that can be potentially measured in current gamma-ray Telescope, like the Fermi-LAT observatory. Therefore, the neutrino flux produced by DM particles is further constrained by *multi-messenger* analyses related to gamma-ray observations.

In particular, the Fermi-LAT Telescope has measured the total *integrated* electromagnetic energy density $\omega_\gamma^{\mathrm{exp}}$ of the isotropic diffuse gamma-ray background (IGRB) from 100 MeV up to 820 GeV [216]. In particular, we have

$$\omega_\gamma^{\mathrm{exp}} \simeq (4.0 \pm 0.7) \times 10^{-7}\,\mathrm{eV/cm}^3\,. \tag{5.13}$$

This measurement provides a bound on the contribution of DM particles to the IGRB spectrum. The total electromagnetic energy density injected by decaying/annihilating DM particles is evaluated through the following expression.

$$\omega_\gamma^{\mathrm{DM}} = \frac{4\pi}{c} \int_{E_{\min}}^{E_{\max}} \sum_{i=\mathrm{gal,extragal}} \left[E_\gamma \left.\frac{\mathrm{d}\Phi_\gamma}{\mathrm{d}E_\gamma}\right|^i + E_e \left.\frac{\mathrm{d}\Phi_e}{\mathrm{d}E_{e^\pm}}\right|^i \right] dE\,, \tag{5.14}$$

where the first term in the integral is the prompt gamma-ray flux, whereas the second is the $e^\pm$ one. Moreover, the galactic contribution is related to the anti-Galactic Center flux ($b = 0$ and $\ell = \pi$ in Galactic coordinates). The extremes of the integral are $E_{\min} = 0.1$ GeV and $E_{\max} = m_{\mathrm{DM}}/2, m_{\mathrm{DM}}$ in case of decaying and annihilating DM particles, respectively.

The quantity $\omega_\gamma^{\mathrm{DM}}$ cannot be larger than $\omega_\gamma^{\mathrm{exp}}$, independently of the propagation in the intergalactic medium. The relation

$$\omega_\gamma^{\mathrm{DM}} \le \omega_\gamma^{\mathrm{exp}} \tag{5.15}$$

provides a robust constraint on viable DM models. Such a constraint is hereafter defined as IGRB bound.

This multi-messenger approach proposed in Ref. [263] would lead to conservative constraints on the parameters (mass, lifetime or cross section) that define DM models. More dedicate multi-messenger analyses constraining DM models are presented in Ref.s [277, 278, 279]. Taking for example the bounds reported in Eqs. (5.3) and (5.6) of Ref. [277], and updating the measurements of cosmological parameters and the IGRB spectrum, one recovers the same bounds shown in the next plots, once the same clumpiness factor is considered.

5.2.2 Results for IceCube 2-year MESE data

We characterize the two-component flux of Eq. (5.10) by analyzing the IceCube 2-year MESE data in order to provide statistical evidence to a possible interpretation of the low-energy excess shown in Fig. 5.2. We underline that the MESE data sample is more suitable for such an analysis focused on low-energy since it has a larger sensitivity for energies $E_\nu \leq 100$ TeV due to the different veto technique. The expected number of neutrino events for the flux of Eq (5.10) is obtained by using the expression (4.19). The MESE effective area[4] is divided into Northern and Southern hemispheres. The two hemispheres correspond to a reconstructed angle in the range $-1.0 \leq \cos\theta_{\mathrm{rec}} \leq 0.2$ and $0.2 \leq \cos\theta_{\mathrm{rec}} \leq 1.0$, respectively. We remind that the variable θ is the Zenith angle. It is worth observing that it would be interesting to perform a study restricted to the Galactic Center, but it would require the detailed knowledge of the IceCube effective area as a function of the reconstructed arrival direction that is unfortunately not public.

Firstly, we present the results of the likelihood-ratio analysis for the case of scalar DM particles χ decaying into a couple of SM fermions $f = b, t, \mu, \tau$. In Fig. 5.6, it is shown the number of standard deviations σ in the m_{DM}–τ_{DM} plane in case of bottom (upper panels) and top (lower panels) quarks in the final states. The darker the color, the larger the statistical significance in σ in favor of the two-component scenario with a DM neutrino flux. The cases of spectral index 2.0 (2.2) are depicted in left (right) panels. In all the plots,

---

[4]The IceCube effective area can be found at `https:/icecube.wisc.edu/science/data/HEnu_above1tev`.
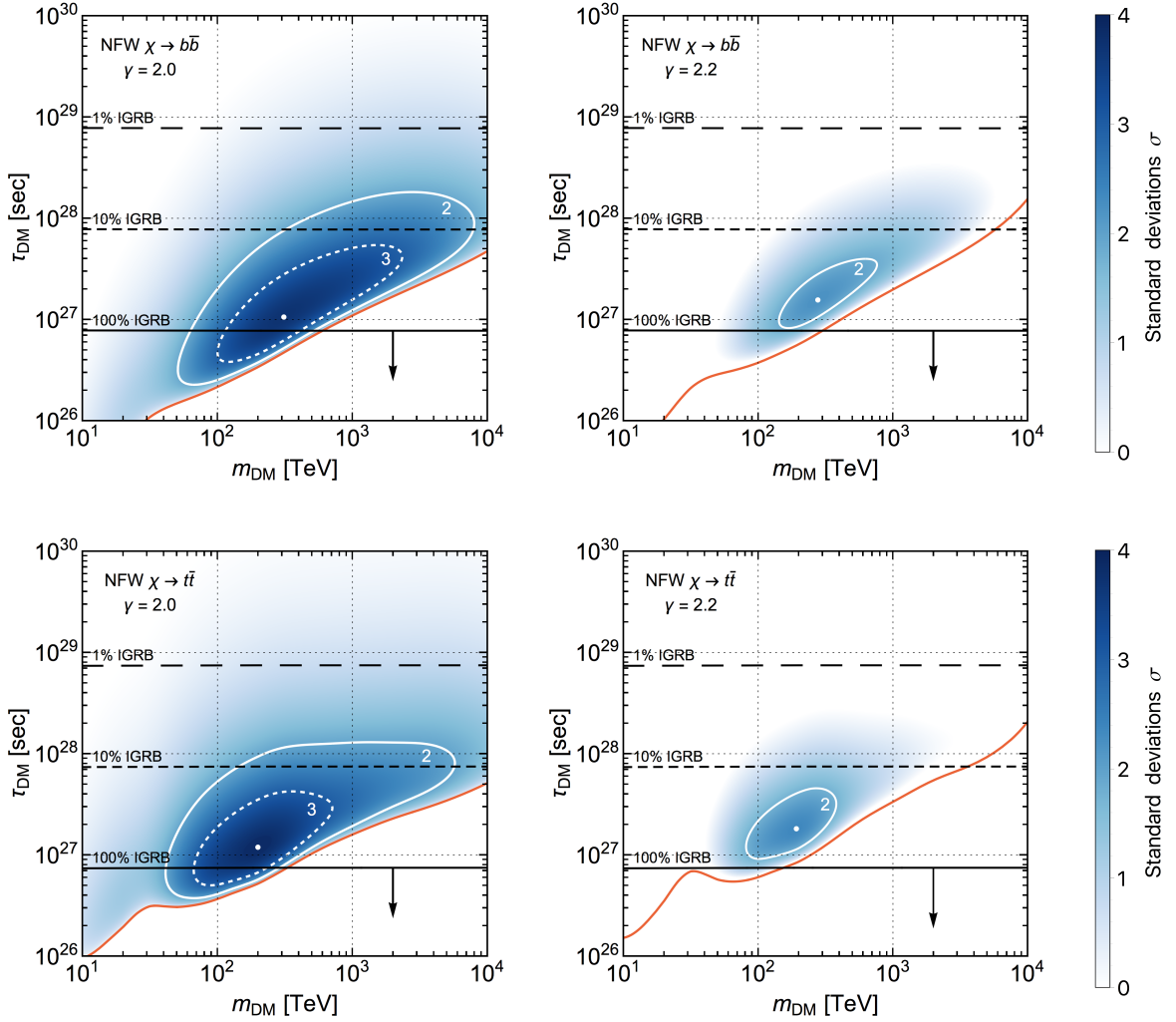
Figure 5.6: Number of standard deviations in σ in the m_{DM}–τ_{DM} plane for the decay channels $\chi \rightarrow b\bar{b}$ (upper panels) and $\chi \rightarrow t\bar{t}$ (lower panels), once the spectral index of the astrophysical flux has been fixed to 2.0 (left panels) and 2.2 (right panels). The white contours bound the regions where the significance level is $\sigma \geq 2$ (solid) and $\sigma \geq 3$ (dashed). The white dots correspond to the best-fit values (maximum significance). The red lines delimit from below the allowed regions according to IceCube data, while the black one refer to different contribution of the DM model to the IGRB measured by Fermi-LAT.

the best-fit corresponding to the maximum significance is represented by white dots. The white contours delimit the regions where $\sigma \geq 2$ (solid lines) and $\sigma \geq 3$ (dashed lines). The red lines instead limit from above the regions in the parameter space where the inclusion
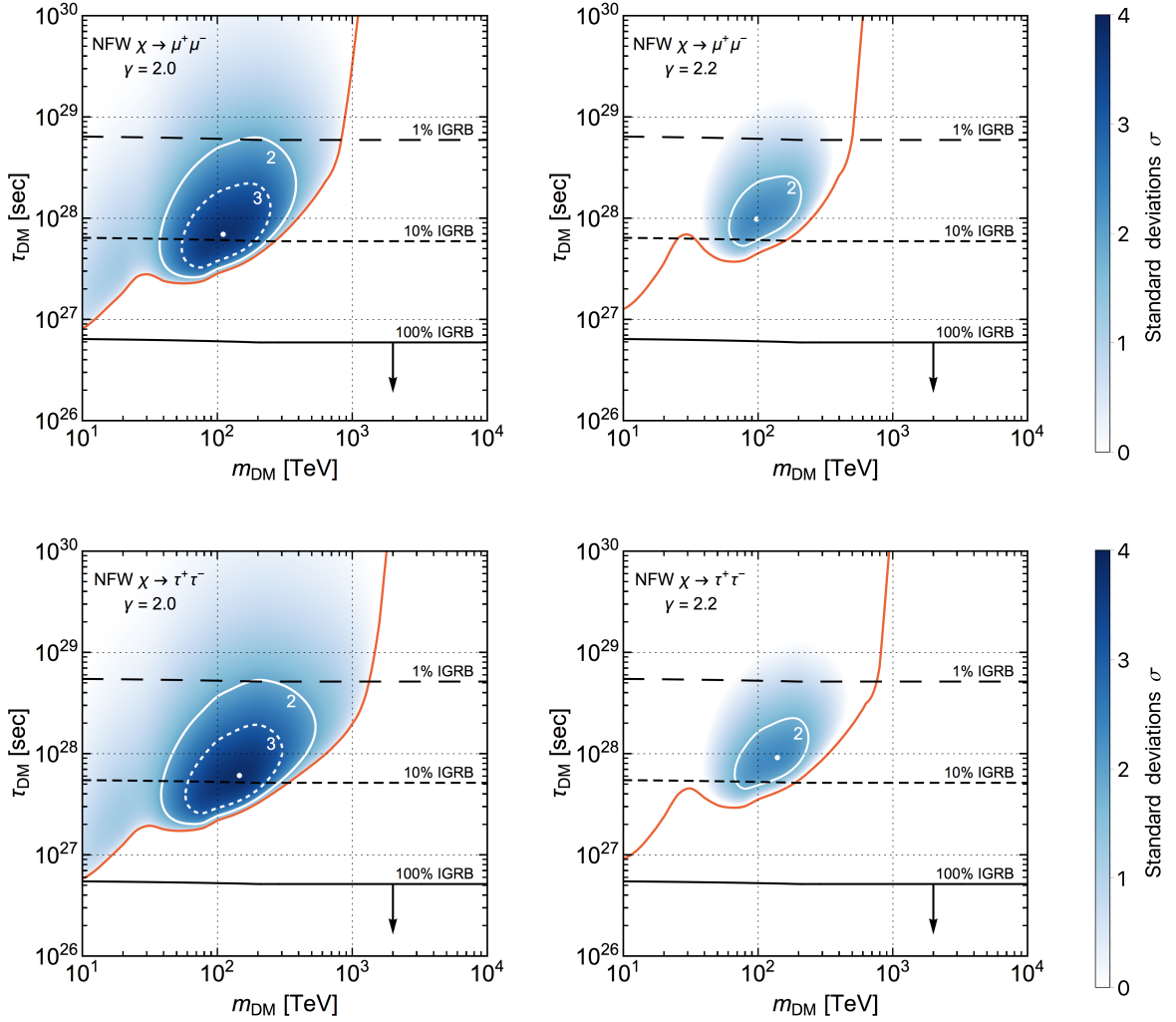
Figure 5.7: Number of standard deviations in σ in the m_{DM}–τ_{DM} plane for the decay channels $\chi \to \mu^+\mu^-$ (upper panels) and $\chi \to \tau^+\tau^-$ (lower panels). The description of the plots is the same of Fig. 5.6.

of a DM component to the neutrino flux makes the fit worse with respect to the case of a single astrophysical power-law. These regions are excluded by the IceCube 2-year MESE data, once a spectral index 2.0 and 2.2 is respectively assumed.

Furthermore, the Fermi-LAT gamma-ray constraints of Eq. (5.15) are shown by the almost horizontal black lines. These lines are related to different DM contributions (1%, 10% and 100%) to the Fermi-LAT IGRB spectrum. In particular, the allowed regions in the m_{DM}–τ_{DM} plane is further limited from below by the solid black lines corresponding to
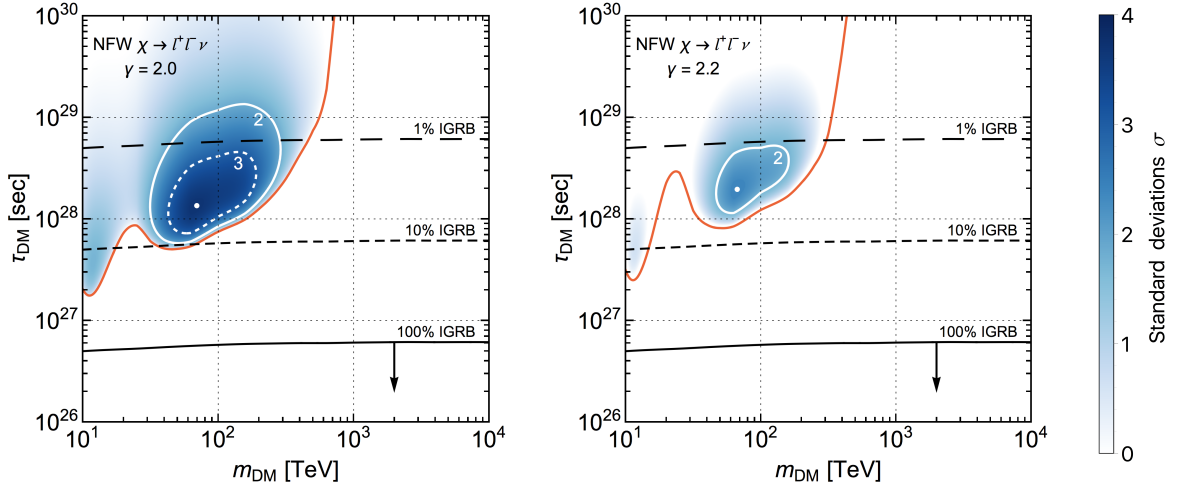
Figure 5.8: Number of standard deviations in σ in the m_{DM}–τ_{DM} plane for the leptophilic three-body decay channels $\chi \to \ell^+\ell^-\nu$. The description of the plots is the same of Fig. 5.6.

$\omega_\gamma^{\mathrm{DM}} = \omega_\gamma^{\mathrm{exp}}$ (100% IGRB). However, the 100% IGRB bound corresponds to the unrealistic situation where the DM signal explains the whole gamma-ray observations made by Fermi-LAT, leaving no room for a contribution of additional astrophysical sources. Since it is quite reasonable to assume that the majority of the IGRB spectrum is accounted for by standard astrophysical sources, we consider the limit $\omega_\gamma^{\mathrm{DM}} \leq 0.1\,\omega_\gamma^{\mathrm{exp}}$ as a realistic constraint for the allowed DM contribution to the gamma-ray flux.

The results for leptophilic couplings are displayed in Fig.s 5.7 and 5.8. The decaying cases into muon and tau leptons are shown in upper and lower panels of Fig. 5.7, respectively. The results of the likelihood-ratio statistical test for the leptophilic three-body decay ($\chi \to \ell^+\ell^-\nu$) are instead reported in Fig. 5.8.

For the plots, one can note that in case of hadronic final states (Fig. 5.6), smaller values for the lifetime τ_{DM} and larger masses m_{DM} are favored with respect to the case of leptonic final states (Fig.s 5.7 and 5.8). Moreover, the tension with the Fermi-LAT data is more evident in models with quarks as final states with respect to the models involving only leptons. Indeed, in order to explain the IceCube measurements, the models with quarks would required values of m_{DM} and τ_{DM} belonging to regions excluded by the 10% IGRB bound. On the other hand, in the case of a leptophilic interaction, the most significant
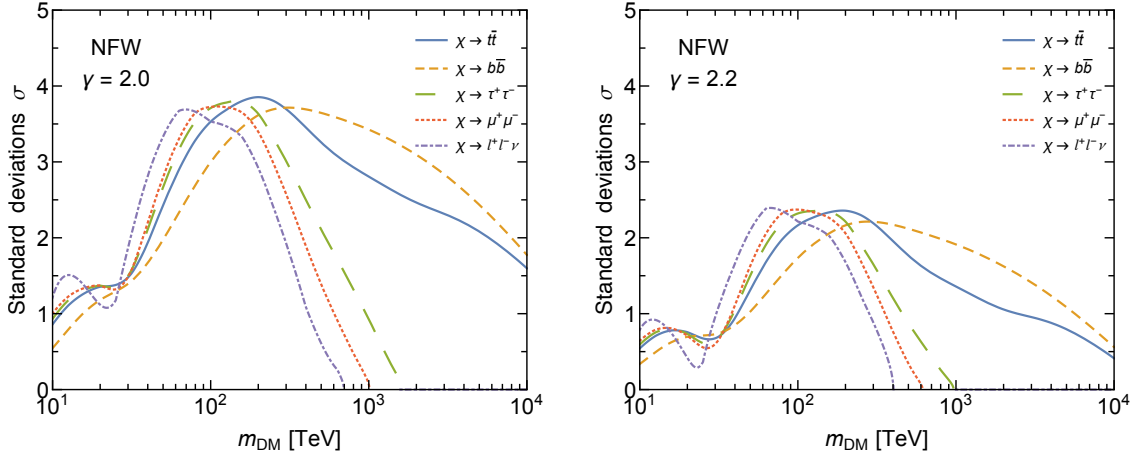
Figure 5.9: Significance in number of standard deviations σ as a function of the mass m_{DM} for all the studied models of decaying DM, in case of a spectral index 2.0 (left panel) and 2.2 (right panel).

region in the parameter space m_{DM}–τ_{DM} corresponds to a IGRB contribution smaller than 10%. Therefore, we can already conclude that the leptophilic scenarios are in fair agreement with both neutrinos and gamma-ray observations under the assumption of a two-component flux. This is not the case of hadronic final states.

For all the analyzed decaying cases, we report the statistical significance in σ as a function of mass m_{DM} in Fig. 5.9. The curves have been obtained by taking the best-fit value for τ_{DM} for each choice of decay channel and mass m_{DM}. We note that the maximum value of such a statistical significance is almost independent on the decay channel. Remarkably, it results to be 3.7–3.9σ and 2.2–2.4σ in case of spectral index 2.0 and 2.2, respectively. Moreover, we find that the maximum significance is achieved for $m_{\mathrm{DM}} \simeq 140$ TeV for $\chi \to \ell^-\ell^+$, while it is maximized at $m_{\mathrm{DM}} \simeq 200$ TeV and $m_{\mathrm{DM}} \simeq 300$ TeV for $\chi \to t\bar{t}$ and $\chi \to b\bar{b}$, respectively. The best-fit of the proposed two-components scenario for the decay channel $\chi \to \tau^-\tau^+$ is displayed in Fig. 5.10, where the DM contribution to the observed neutrino energy spectrum is clearly shown in Southern (left panel) and Northern (right panel) hemispheres. The difference of the best-fit values for m_{DM} among the DM models is explained by the fact that in the hadronic cascades neutrinos are mainly produced at low energies, while in the leptonic channels their energy can be as large as $m_{\mathrm{DM}}/4$ (the

maximum energy of leptons is $m_{\mathrm{DM}}/2$ for a two-body decays). This consideration also explains why DM masses larger than about 1 PeV (700 GeV) are excluded by IceCube data for the leptonic decay channels for $\gamma = 2.0$ ($\gamma = 2.2$), while no constraints are obtained in case of hadronic channels. Moreover, we note that the smallest best-fit DM mass is obtained in case of the leptophilic three-body decays (dotdashed purple line in Fig. 5.9), according to fact that primary neutrinos are produced up to an energy equal to $m_{\mathrm{DM}}/2$.

Finally, the results for the annihilating scenarios are reported in in Fig. 5.11, where only the channels $\chi\chi \to t\bar{t}$ (upper panels) and $\chi\chi \to \tau^+\tau^-$ (lower panels) are shown. Indeed, these two annihilating channels are representative for all the hadronic and leptonic scenarios, respectively. Ase one can see from the plot, the maximum statistical significance (best-fits shown with white dots) is reached for the same values of the DM mass obtained in the decaying case. On the other hand, we find at the best-fit a thermally averaged cross section of the order of $10^{-24} \div 10^{-23}$ cm^3/s. As for the decaying case, the maximum significance in standard deviations is $\sim 3.8\sigma$ and $\sim 2.3\sigma$ for spectral index 2.0 and 2.2, respectively.

In addition to the gamma-rays constraints (black lines) delimiting from above the allowed regions of the parameter space, we have to consider also the constraints due to the *unitarity bound* [280, 281, 282] (yellow line). Too large values for the thermally averaged cross section $\langle \sigma v \rangle$ are indeed excluded according to the relation

$$\langle \sigma v \rangle \leq \frac{4\pi}{m_{\mathrm{DM}}^2\, v} = 1.5 \times 10^{-23} \frac{\mathrm{cm}^3}{\mathrm{s}} \left[\frac{100\,\mathrm{TeV}}{m_{\mathrm{DM}}} \right]^2 , \tag{5.16}$$

where the typical value $v = 300$ km/s of the DM velocity v has been considered ($v = 300$ km/s). This strong constraint implies that the models of DM particles annihilating into quarks are not viable for explaining the IceCube observations, which instead would require larger values for $\langle \sigma v \rangle$. On the other hand, leptophilic scenarios are compatible both with the gamma-ray constraints (IGRB spectrum measured by Fermi-LAT) and with unitarity.

All the plots presented here have been obtained by considering the Navarro-Frenk-White halo density distribution. The results related to the Isothermal distribution do not significantly differ from the shown results, and therefore they are not reported here. In particular,
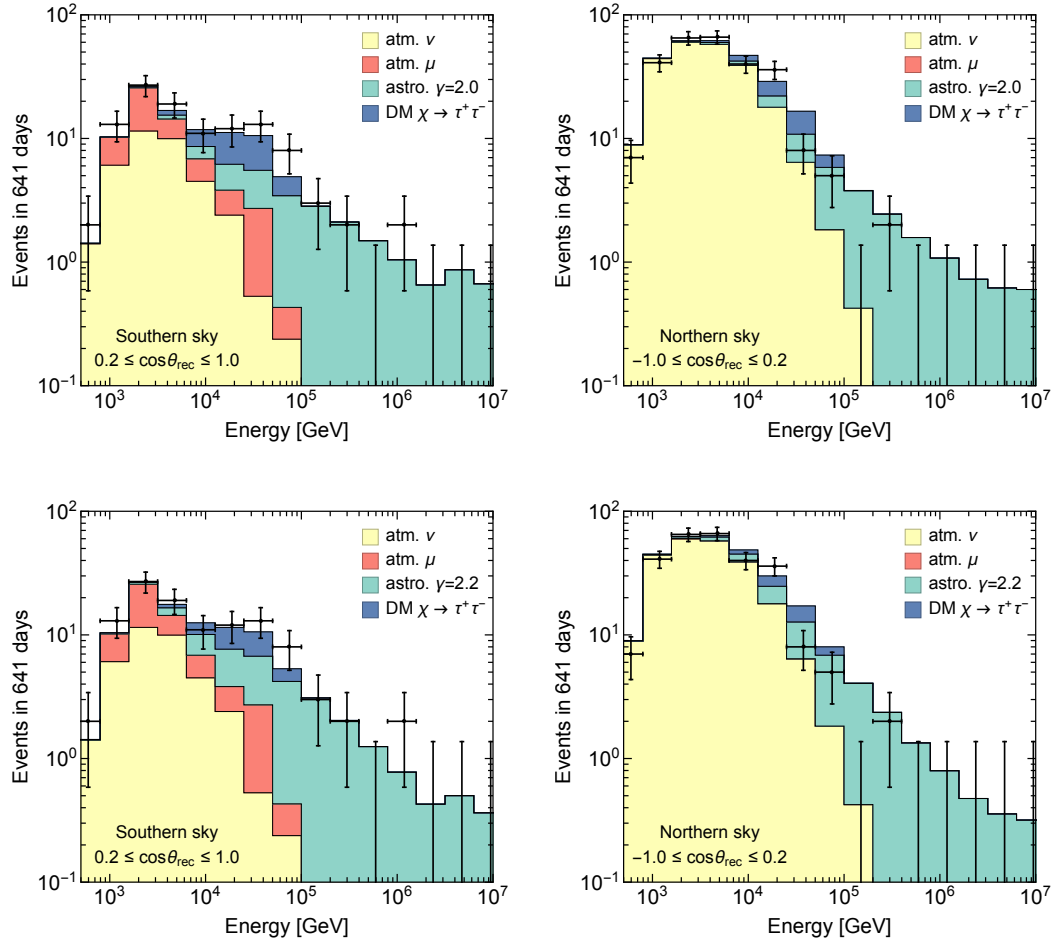
Figure 5.10: Numbers of neutrino events as a function of the neutrino deposited energy after 641 days of data-taking (MESE sample), in the Southern (left panels) and Northern (right panels) hemispheres. The astrophysical component (green color) is a power-law with a spectral index 2.0 (upper panels) and 2.2 (lower panels). The DM contribution (blue color) refers to the decaying DM model $\chi \to \tau^+\tau^-$ with $m_{\mathrm{DM}} = 140$ TeV and $\tau_{\mathrm{DM}} = 6 \times 10^{27}$ sec ($\tau_{\mathrm{DM}} = 9 \times 10^{27}$ sec) for $\gamma = 2.0$ ($\gamma = 2.2$).

in case of decaying DM the Isothermal profile provides a statistical significance that differs less than 1% with respect to the NFW distribution. On the other hand, in case of annihilating DM, the significance level of the two-components flux decreases by 0.1 if the Isothermal distribution rather than the NFW one is considered. A much larger dependence on the halo density profile is in general expected in case of a spatial study on neutrino
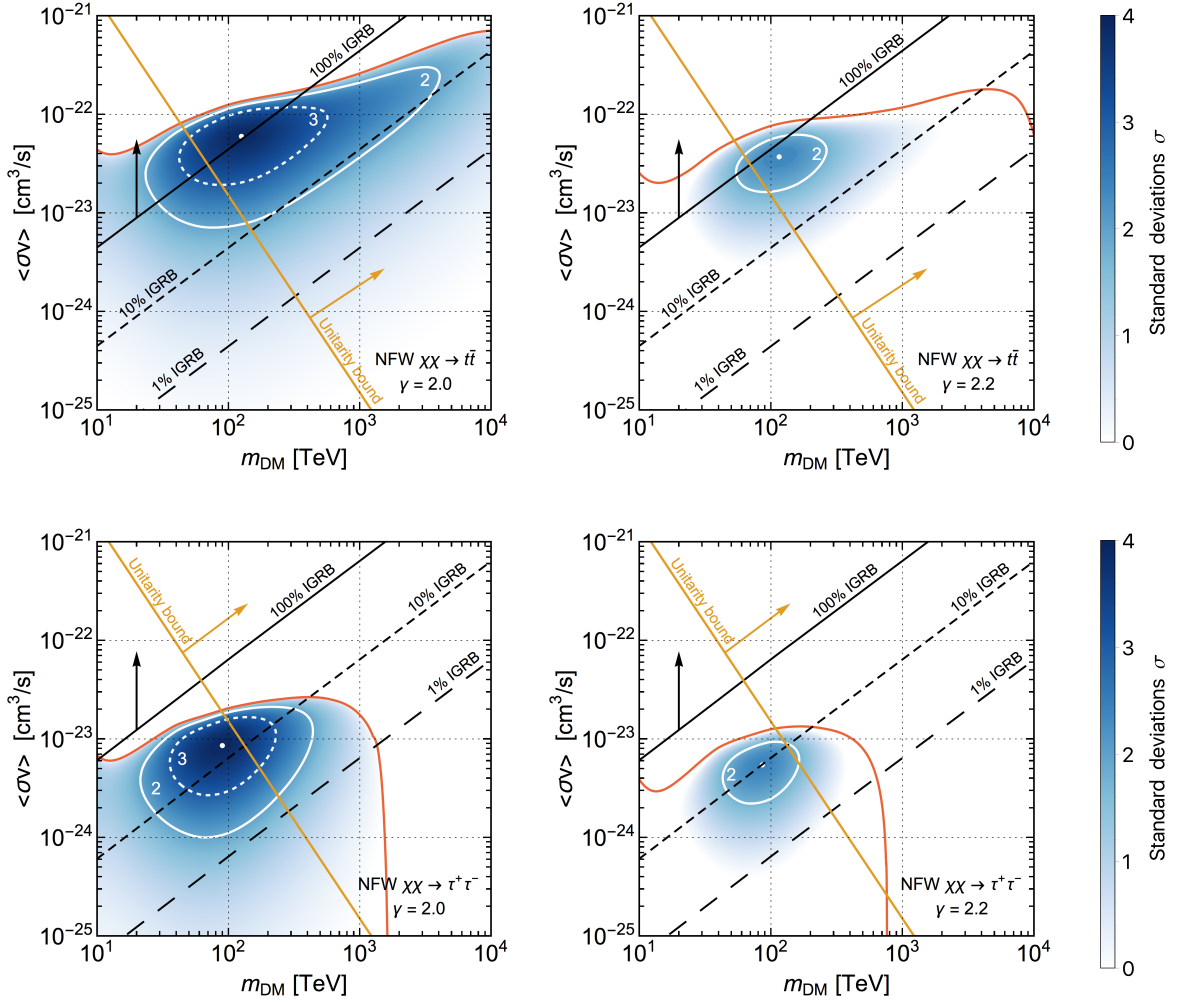
Figure 5.11: Number of standard deviations in σ in the $m_{\mathrm{DM}}-\langle\sigma v\rangle$ plane for annihilation channels $\chi\chi \to t\bar{t}$ (upper panels) and $\chi\chi \to \tau^+\tau^-$ (lower panels). The description of the plots is the same of Fig. 5.6. In addition, the yellow lines show the unitarity constraint of the thermally averaged cross section provided in Eq. (5.16).

events (as shown in Section 5.1). However, such a study would require a larger statistics and a detailed knowledge of the IceCube effective area. Moreover, the results for annihilating DM have been derived by assuming a particular clumpiness parametrization (described in Section 3.1). However, even though a change in this parametrization is going to slightly affect the allowed range for $\langle\sigma v\rangle$, the qualitatively conclusions remain unchanged.

We conclude claiming that, under the prior of a spectral index in the interval $[2.0, 2.2]$,

the statistical relevance of a two-component flux with respect to a single power-law ranges from 2 to 4σ. By comparing Fig.s 5.6, 5.7 and 5.8 with Fig. 5.11, we note that:

- the decaying models are less constrained than the annihilating ones;

- neutrino (IceCube) and gamma-ray (Fermi-LAT) observations are more in favor of an interpretation of the neutrino low-energy excess in terms of leptonic final states rather than the hadronic ones.

5.2.3 Results for IceCube 6-year HESE data

In this last part of the Chapter, we perform the analysis on the observed neutrino energy spectrum by using the latest IceCube 6-year HESE data, following the statistical procedure adopted for the IceCube 2-year MESE data. The main results of such an analysis are reported in Fig. 5.12 and 5.13. As for the previous analysis, the plots display the number of standard deviations σ in the m_{DM}–τ_{DM} plane for the tow decay channels $\chi \to t\bar{t}$ and $\chi \to \tau^+\tau^-$. The upper and lower panels of both figures refer to an astrophysical power-law with spectral index 2.0 and 2.2, respectively. In the plots, the best-fit values (maximum significance) are represented by white stars (the capital letter "H" stands for 6-year HESE analysis). The new best-fits are compared to the previous results (black dots with the capital letter "M") deduced by IceCube 2-year MESE data. The white solid (dashed) contours delimit the regions in the m_{DM}–τ_{DM} plane where the statistical significance is larger than 3σ (2σ). Independently the decay channel considered, we found the maximal statistical significance at the best-fit to be equal to 3.75σ and 2.60σ in case of spectral index 2.0 and 2.2, respectively.

Moreover, the constraints on decaying DM models according to the latest IceCube observations are shown by the solid red lines. The dashed red lines instead correspond to the constraints deduced by analyzing the IceCube 2-year MESE data. It is worth observing that the IceCube 6-year HESE data bound the possible DM models in a region with $m_{\mathrm{DM}} \geq 100$ TeV. This feature depends on two effects:

- the different energy thresholds for HESE data set (20 TeV) and MESE sample (1 TeV)
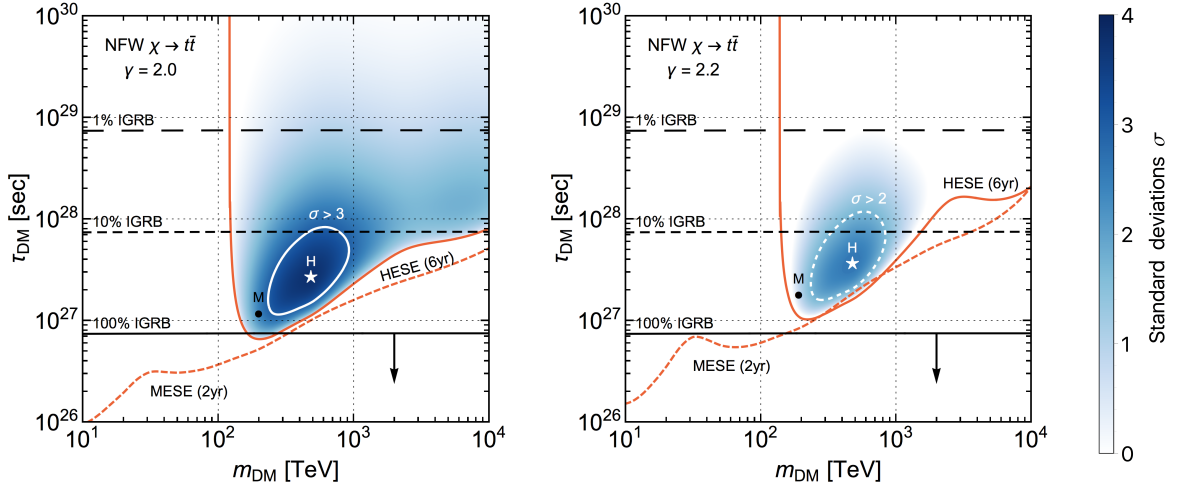
Figure 5.12: Number of standard deviations σ in the m_{DM}–τ_{DM} plane for the decay channel $\chi \to t\bar{t}$, once the spectral index of the astrophysical power-law has been fixed to 2.0 (upper panel) and 2.2 (lower panel). The white contours highlight the regions where the statistical significance is larger than 2σ (dashed line) and 3σ (solid line). The white stars (black dots) correspond to the best-fit values deduced by the IceCube 6-year HESE (2-year MESE) data. The solid (dashed) red lines bound from below the allowed region according to the IceCube 6-year HESE (2-year MESE) data. The black lines refer to different contribution of the DM model to the IGRB measured by Fermi-LAT.

> provide different sensitivity of data and hence of TS for light χ;

- as can be seen from Figure 5.1, the second energy bin from left, corresponding to almost 25–40 TeV, shows a defect in the number of events and thus it disfavors any additional second component contributing to this energy. This pushes the possible DM models to higher masses.

The almost horizontal black lines correspond to the gamma-ray constraints as previously discussed. As for the previous analysis, hadronic channels result to be more in tension with Fermi-LAT observations since they require smaller values for the lifetime τ_{DM} and larger DM masses m_{DM} with respect to the leptonic channels. In particular, we find the best-fit values $m_{\mathrm{DM}} \simeq 500$ TeV and $\tau_{\mathrm{DM}} \simeq 2.77 \times 10^{27}$ sec for m_{DM}–τ_{DM}, while we have $m_{\mathrm{DM}} \simeq 400$ TeV and $\tau_{\mathrm{DM}} \simeq 1.65 \times 10^{28}$ sec for $\chi \to \tau^+\tau^-$. Fig. 5.14 shows the predictions
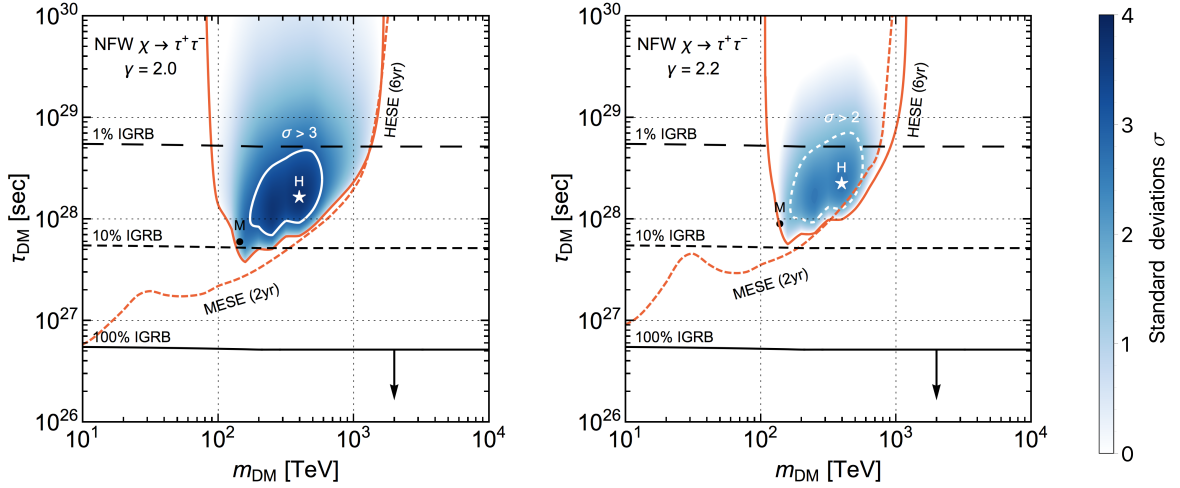
Figure 5.13: Number of standard deviations in σ in the m_{DM}–τ_{DM} plane for the decay channel $\chi \to \tau^+\tau^-$. The description of the plots is the same of Figure 5.12.

of the two-component neutrino flux for the latter case. The conclusions of this statistical analysis confirm the previous results obtained by using the IceCube 2-year MESE data. However, the best-fits for 6-year HESE prefer larger values for m_{DM} even though this could be partially explained in terms of a lower sensitivity of such data set to low energy events.
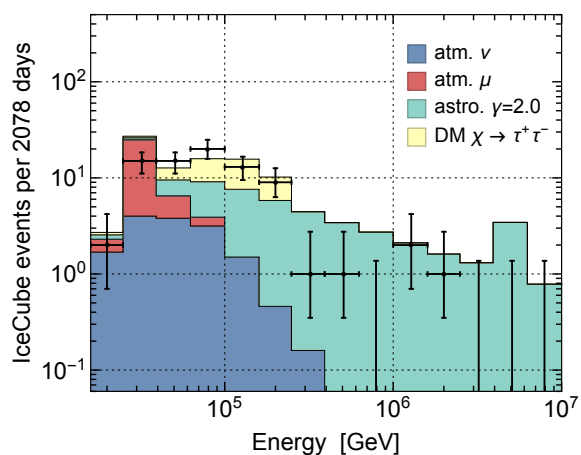
Figure 5.14: Numbers of neutrino events as a function of the neutrino energy after 2078 days of data-taking (HESE sample), for the two-component flux provided in Eq. (5.10). The astrophysical contribution (green color) is a power-law with a spectral index 2.0. The DM contribution (yellow) correspond to the DM model with the decay channel $\chi \to \tau^+\tau^-$ for $m_{\mathrm{DM}} \simeq 400$ TeV and $\tau_{\mathrm{DM}} \simeq 1.65 \times 10^{28}$ sec (best-fit values).

Chapter 6

Model for Decaying Leptophilic Dark Matter

In this last Chapter, we present a model with a DM candidate χ that couples only with the leptons of the Standard Model. We define such a candidate as a *leptophilic* DM particle. In particular, in the model discussed here, DM is unstable and decay through the three-body process $\chi \to \ell^+\ell^-\nu$, which provides an interesting and peculiar signal at Neutrino Telescopes. We show that, in the most minimal version of the model, the same operator mediating the leptophilic three-body decays could at the same be responsible for the DM production in the early Universe by means of the *freeze-in* production mechanism.

The paradigm of decaying DM is in general somewhat unnatural, in the sense that its lifetime has to be at least larger than the age of the Universe ($t_{\mathrm{Universe}} \simeq 4.35 \times 10^{17}\,\mathrm{sec}$) [283]. This unavoidable constraint implies that the DM decay necessarily has to be a suppressed process. Since the decay rate of any particle roughly scales with some power of its mass, we have to find a way to obtain strong suppressions that are required for a DM mass $m_{\mathrm{DM}} \geq 100$ TeV (mass range interesting for IceCube). It is worth observing that such strong suppressions are in general not needed for annihilating DM particles since one can always invoke some conservation law that keeps χ particles stable. The possible ways to suppress the decay rate of DM particles are listed in the following.

- **Small phase space**. This can be achieved by either choosing the mass of the decaying

90

particle to be small or to only allow for final state particles whose sum of masses is nearly identical to the mass of the parent particle. The former is employed, for example, for keV sterile neutrinos [130, 284], while the latter option is for example used to explain the 3.5 keV hint [138, 139] by the decays of excited DM states [285, 286]. However, the suppression due to a small phase space is not a viable option for very heavy DM particles. We remind that very high-energy neutrinos are required in order to account for the IceCube observations.

- **Operators suppressed by Planck-scale mass**. In this case, the resulting interaction (or in this case decay) rates are then usually very small. This occurs, for instance, in processes that may only be induced at very high energies [287], where gravity is expected to break global symmetries [288]. We will show that this suppression is not a viable option in case of a model for a mass $m_{\mathrm{DM}} = \mathcal{O}\left(1\,\mathrm{PeV}\right)$, if one wants to use the same operator for both DM production and indirect detection at Neutrino Telescopes. Moreover, we underline that, unless a full UV-complete theory is specified, an introduction of Planck-scale suppressed operators is not much more than a parametrization of the apparent lack of knowledge.

- **Very tiny couplings**. Once the previous ideas are exhausted, this is the remaining possibility. In particular, very tiny couplings can be regarded as the final generic option since the previous two possibilities either do not work or are just pushing the problem to different scales. Any setting that explain the IceCube data via decaying DM scenario has to be tuned with very tiny couplings, unless unknown exotic high-scale physics is assumed, which may alleviate the tension.

These options represent the only simple ways to suppress the decay rate, because apart from the initial state mass, from the phase space, and from the size of the squared matrix element, there are no other ingredients that one could play with.

The Chapter is divided into three Sections. The first one is devoted to discuss the DM model based on an abelian or non-abelian flavor symmetry. In the second Section, we report the fit of the model deduced by the IceCube 3-year HESE data. In the last Section, we

describe how the DM is produced in the early Universe by means of the freeze-in mechanism and we report our numerical results obtained by solving the Boltzmann equations.

6.1 The model

Let us consider a heavy fermionic DM candidate χ, which is a singlet under the SM gauge group $U_Y(1) \otimes SU_L(2) \otimes SU_C(3)$. Under the requirement of a direct coupling to neutrinos, the simplest operator one can think of is the 4-dimension Yukawa interaction

$$y_\alpha \, \bar{L}_\alpha \tilde{H} \chi \,, \tag{6.1}$$

where α runs over the lepton flavors e, μ, τ. For the sake of simplicity, here we consider only a new fermionic singlet particle. The particle χ has the same quantum number of the right-handed neutrino and the interaction term in Eq. (6.1) is the standard coupling for the type-1 seesaw [131, 132, 133, 134, 135, 136]. Such an operator, whose phenomenological implications are studied in detail in Ref.s [289, 263, 290, 291], is relevant for the IceCube observations if the coupling y_α is very tiny, i.e. $y_\alpha \sim \mathcal{O}(10^{-30})$. Note that, due to the smallness of such a coupling, the Yukawa interaction does not provide any sizable contribution to the mass of light neutrinos. At three level, the decay channels of χ mediated by the operator (6.1) are

$$\chi \to \ell_\alpha^\pm + W^\mp \,, \qquad \chi \to \nu_\alpha + Z \,, \qquad \chi \to \nu_\alpha + H^0 \,, \tag{6.2}$$

with branching ratios equal to 2:1:1. Even though there are channels with primary neutrinos providing a sharp peak in the neutrino flux, the weak gauge bosons and the Higgs allows for an abundant production of heavy quarks. As seen in the previous Chapter, the scenarios with quarks in the final states (hadronic channels) are problematic if one considers the gamma-ray constraints as well. Moreover, in case of PeV DM, the secondary neutrinos produced in the hadronic cascades give an almost flat neutrino flux at lower energies. For $m_{\rm DM} = \mathcal{O}\,(1\,{\rm PeV})$, such a flux could explain the whole diffuse TeV–PeV neutrino flux, leaving no room for a contribution from standard astrophysical sources. We remind that we expect at least an astrophysical neutrino flux behaving as a $E_\nu^{-2.0}$ power-law according to the Waxman-Bahcall bound reported in Eq. (4.14).

Dimensions	Possible allowed operators
4	$\bar{L}\tilde{\phi}\chi$
5	$--$
6	$\bar{L}\ell\,\bar{L}\chi, \quad H^{\dagger}H\bar{L}\tilde{H}\chi, \quad (\tilde{H})^{t}D_{\mu}\tilde{H}\bar{\ell}\gamma^{\mu}\chi,$
	$\bar{Q}d\,\bar{L}\chi, \quad \bar{u}Q\,\bar{L}\chi, \quad \bar{L}d\,\bar{Q}\chi, \quad \bar{u}\gamma_{\mu}d\,\bar{\ell}\gamma^{\mu}\chi,$
	$D^{\mu}\tilde{H}D_{\mu}\bar{L}\chi, \quad D^{\mu}D_{\mu}\tilde{H}\bar{L}\chi,$
	$B_{\mu\nu}\bar{L}\sigma^{\mu\nu}\tilde{H}\chi, \quad W^{a}_{\mu\nu}\bar{L}\sigma^{\mu\nu}\tau^{a}\tilde{H}\chi$

Table 6.1: List of gauge-invariant operators up to dimension-6 for a fermionic singlet DM particle χ. The list is taken from Ref. [292].

In order to improve the need of an unnatural very tiny coupling and to provide a leptophilic operator with no quarks in the final states (IceCube and Fermi-LAT observations are in favor of leptonic final states with respect to hadronic ones), we consider a higher dimension operator having the following characteristics:

1. the DM particle is coupled to the SM particles via a leptophilic coupling;

2. the non-renormalizable interaction provides a lifetime of χ that is suppressed by powers of a scale of new physics;

3. the operator has to allow for a direct coupling to neutrinos providing a primary neutrino flux with energy of the order of the DM mass. Neutrinos at lower energies can be produced in the multi-body decays in such a way that the neutrino flux is also spread to lower energies;

4. for the sake of simplicity, we assume that χ represents the dominating contribution of Cold DM.

Following Ref. [292], in Tab. 6.1 we report the full list of gauge-invariant operators up to dimension-6. In order to simplify the notation, we have omitted the family index for all the

	Leptonic Sector			Scalar Sector	Dark Sector
Field	L_e, ℓ_e	L_μ, ℓ_μ	L_τ, ℓ_τ	H	χ
Charge q_ψ	2	1	4	0	3

Table 6.2: $U_f(1)$ charges q_ψ for a possible realization of a model containing only the operator of Eq. (6.3).

matter fields. Remarkably, one can note that there exists only one operator in this list that satisfies the requirements 1–3. Such a *non-renormalizable lepton portal* operator is given by

$$\frac{y_{\alpha\beta\gamma}}{M_{\text{Pl}}^2} \left(\overline{L_\alpha}\ell_\beta\right)\left(\overline{L_\gamma}\chi\right) + \text{h.c.} \,, \tag{6.3}$$

where $\{\alpha, \beta, \gamma\}$ are flavor indexes that label a total of 27 different operators. The round brackets explicitly indicate the Lorentz contractions. Note that expanding the $SU(2)$ contractions, such an operator always leads to DM decays into two charged leptons and one neutrino. Depending on the flavor indexes, the charged leptons can then possibly decay into secondary neutrinos. At this level, i.e. without specifying the full UV-complete theory, we chose to parametrize the mass scale of new physics in terms of the Planck mass M_{Pl}. The other operators listed in Tab. 6.1 all involve quarks, directly or indirectly through the couplings to the Higgs field or the $U_Y(1)$ and $SU_L(2)$ gauge bosons.

Hence, if one wants to allow for only the operator (6.3) as source of DM decays, we have to invoke some symmetry that forbids the 4-dimensional operator (6.1) and the other 6-dimensional ones. The required selection rule can be obtained by using global flavor symmetries, both Abelian like $U_f(1)$ and non-Abelian like A_4. In the following, we will discuss these two benchmark schemes ($U_f(1)$ or A_4 flavor symmetry) as relevant examples.

6.1.1 Abelian flavor symmetry $U_f(1)$

Let us introduce a new global flavor symmetry that assigns a particular charge to the SM leptons and to the particle χ. We denote with q_ψ the $U_f(1)$ flavor charge of a generic field ψ. With an Abelian flavor symmetry, it is not possible to single out a flavor-diagonal operator in Eq. (6.3). Indeed, in this case both the operators $\bar{L}_\alpha \ell_\alpha \bar{L}_\alpha \chi$ and $\bar{L}_\alpha H \ell_\alpha$ would

be invariant under such a symmetry, implying also the invariance of the term $L_\alpha \tilde{H} \chi$ that has to be forbidden. For a flavor-diagonal operator in Eq. (6.3) we have

$$
\left.
\begin{array}{lll}
\bar{L}_\alpha \ell_\alpha \bar{L}_\alpha \chi & \implies & -2q_{L_\alpha} + q_{\ell_\alpha} + q_\chi = 0 \\
\bar{L}_\alpha H \ell_\alpha & \implies & -q_{L_\alpha} + q_\phi + q_{\ell_\alpha} = 0
\end{array}
\right\}
\implies
-q_{L_\alpha} - q_\phi + q_\chi = 0 \, , \quad (6.4)
$$

relation that inevitably allows for the operator (6.1) in the Lagrangian. This conclusion can be bypassed by introducing the supersymmetry or allowing for a mix of different lepton flavors. In the latter case, a possible realization of a model, which contains only the leptophilic dimension-6 operator (6.3) among the ones listed in Tab. 6.1, is shown in Tab. 6.2. In this case, in addition to the SM interactions, the Lagrangian contains only the following invariant dimension-6 operators

$$
\mathcal{O}_6 = \frac{1}{M_{\rm Pl}^2} \left(y_{\mu e \tau} \, \overline{L_\mu} \ell_e \overline{L_\tau} \chi + y_{\tau e \mu} \overline{L_\tau} \ell_e \overline{L_\mu} \chi + y_{e \mu e} \, \overline{L_e} \ell_\mu \overline{L_e} \chi \right) + \text{h.c.} \, . \qquad (6.5)
$$

These operators provide three different DM decay channels with flavor structure

$$
\{ \alpha, \beta, \gamma \} \equiv \{ \mu, e, \tau \} + \{ \tau, e, \mu \} + \{ e, \mu, e \} \, . \qquad (6.6)
$$

It is worth observing that the charge assignment in Tab. 6.2 is not unique. Different assignments would provide DM decays with a different flavor structure. In principle, a study of the flavor composition of IceCube neutrino data would give useful hints in the definition of the possible flavor charges.

An Abelian flavor symmetry like $U_f(1)$ is a viable symmetry only for Dirac DM particles. Indeed, the requirement of a non-zero charge to χ implies that the DM candidate cannot be a Majorana fermion. For the model with the charge assignment of Tab. 6.2 (hereafter referred as *model 1*), the total decay width of DM is given by

$$
\Gamma_\chi = \tau_\chi^{-1} = \frac{1}{6144 \, \pi^3} \left(2 \left| y_{\mu e \tau} - y_{\tau e \mu} \right|^2 + \left| y_{e \mu e} \right|^2 \right) \frac{m_\chi^5}{M_{\rm Pl}^4} \, , \qquad (6.7)
$$

For the sake of simplicity, in the fit performed with IceCube data we assume the following relation among the three different couplings

$$
\left| y_{\mu e \tau} - y_{\tau e \mu} \right| = \left| y_{e \mu e} \right| \equiv y \, . \qquad (6.8)
$$

We observe that in this model it is also possible to account for the neutrino masses and oscillations parameters. Indeed, the charge assignment provides a flavor structure for the dimension-5 Weinberg operator $\overline{L_\alpha} L_\beta^c \tilde{H} \tilde{H}$ that is equivalent to the so-called B_4 two-zeros texture given in Ref. [293]. Such a texture allows for a fit of the lepton mixing parameters as studied in Ref.s [294, 295].

6.1.2 Non-Abelian flavor symmetry A_4

Another possible realization of our model with only the additional operator (6.3) can be achieved by invoking non-Abelian discrete symmetries [296, 297, 298, 299]. Here, we discuss the case of the A_4 symmetry. Such a symmetry is the group of even permutations of four objects. It can be viewed as the symmetry group of proper rotations leaving invariant a tetrahedron.[1] The group consists of twelve elements and admits four irreducible representations: a triplet $\mathbf{3}$ and three different singlets $\mathbf{1}$, $\mathbf{1}'$ and $\mathbf{1}''$. The multiplication rules of these representations are

$$\mathbf{3} \otimes \mathbf{3} = \mathbf{3}_S \oplus \mathbf{3}_A \oplus \mathbf{1} \oplus \mathbf{1}' \oplus \mathbf{1}'' , \tag{6.9}$$

$$\mathbf{3} \otimes \mathbf{1} = \mathbf{3} \otimes \mathbf{1}' = \mathbf{3} \otimes \mathbf{1}'' = \mathbf{3} , \tag{6.10}$$

$$\mathbf{1}' \otimes \mathbf{1}' = \mathbf{1}'' , \tag{6.11}$$

$$\mathbf{1}'' \otimes \mathbf{1}'' = \mathbf{1}' , \tag{6.12}$$

$$\mathbf{1}' \otimes \mathbf{1}'' = \mathbf{1} , \tag{6.13}$$

---

[1]Such transformations are: eight rotations of 120° around an axis passing through a vertex and a face opposite to the vertex; three rotations around an axis passing through the middle of two edges not belonging to the same face; and the identity.

	Leptonic Sector		Scalar Sector			Dark Sector
Field	L	ℓ	H_1	H_2	H_3	χ
Irreducible Representation	**3**	**3**	**1**	**1'**	**1''**	**1**

Table 6.3: Irreducible representations allocating the fields in case of the non-Abelian A_4 symmetric model. The quarks are all singlets under A_4.

Denoting with a_i and b_i the three components of two triplets, the first of the multiplications rule lead to the following combinations.

$$\mathbf{3}_S = (a_2b_3 + a_3b_2, a_3b_1 + a_1b_3, a_1b_2 + a_2b_1) \,, \tag{6.14}$$

$$\mathbf{3}_A = (a_2b_3 - a_3b_2, a_3b_1 - a_1b_3, a_1b_2 - a_2b_1) \,, \tag{6.15}$$

$$\mathbf{1} = a_1b_1 + a_2b_2 + a_3b_3 \,, \tag{6.16}$$

$$\mathbf{1'} = a_1b_1 + \omega a_2b_2 + \omega^2 a_3b_3 \,, \tag{6.17}$$

$$\mathbf{1''} = a_1b_1 + \omega^2 a_2b_2 + \omega a_3b_3 \,, \tag{6.18}$$

where the phase $\omega = e^{2\pi i/3}$ is such that $\omega^3 = 1$.

A possible realization of the model under consideration is obtained in a framework where the fields transform as irreducible representations of A_4 as reported in Tab. 6.3. In particular, the three left-handed lepton doublets and the three right-handed lepton singlets are allocated into the two A_4 triplets $L = \{(\nu_e, e_L), (\nu_\mu, \mu_L), (\nu_\tau, \tau_L)\}$ and $\ell = \{e_R, \mu_R, \tau_R\}$, respectively. As it will be discussed later, the model also requires three different Higgs-like $SU_L(2)$ doublets H_1, H_2 and H_3 belonging to the A_4 singlets $\mathbf{1}$, $\mathbf{1'}$ and $\mathbf{1''}$, respectively. In the model (hereafter referred as *model 2*), the Lagrangian of the Dark Sector contains the following relevant terms.

$$\mathcal{L} \supset -\frac{1}{2}(m_{\mathrm{DM}}\,\overline{\chi^c}\chi + \mathrm{h.c.}) + \mathcal{O}_6 \,, \tag{6.19}$$

where the first term gives the mass m_{DM} to the field χ, whereas the second one is the lowest oder non-renormalizable operator allowed by the A_4 symmetry. Such an operator corresponds to two Fermi-like decay interactions given by

$$\mathcal{O}_6 = \frac{y_+}{M_{\mathrm{Pl}}^2}\,(\bar{L}\ell)_{\mathbf{3}_S}\bar{L}\,\chi + \frac{y_-}{M_{\mathrm{Pl}}^2}\,(\bar{L}\ell)_{\mathbf{3}_A}\bar{L}\,\chi + \mathrm{h.c.} \,, \tag{6.20}$$

where the notation $(..)_{\mathbf{3}_{S,A}}$ underlines the two possible contractions of two triplets into one triplet representation according to Eq.s (6.14) and (6.15). Such an operator has the same properties of the one given in Eq. (6.3). We note that the A_4 symmetry also significantly simplifies the flavor structure allowing for two independent couplings, namely y_+ and y_-, only. By expanding the operator (6.20) using the relations (6.14), (6.15) and (6.16), we obtain

$$
\begin{aligned}
\mathcal{O}_6 \;=\; & \sum_{\pm} \frac{y_\pm}{M_{\rm Pl}^2} \left[(\bar{\nu}_\tau \mu_R \pm \bar{\nu}_\mu \tau_R) \bar{e}_L \chi - (\bar{\tau}_L \mu_R \pm \bar{\mu}_L \tau_R) \bar{\nu}_e \chi \right. \\
& + (\bar{\nu}_e \tau_R \pm \bar{\nu}_\tau e_R) \bar{\mu}_L \chi - (\bar{e}_L \tau_R \pm \bar{\tau}_L e_R) \bar{\nu}_\mu \chi \\
& \left. + (\bar{\nu}_\mu e_R \pm \bar{\nu}_e \mu_R) \bar{\tau}_L \chi - (\bar{\mu}_L e_R \pm \bar{e}_L \mu_R) \bar{\nu}_\tau \chi \right] + \text{h.c.} \, .
\end{aligned}
\tag{6.21}
$$

These operators allow for six different decay channels of DM particles with branching ratio $1/6$ and with flavor structure $\{e, \mu, \tau\}$ plus its cyclic permutations. The total decay with is therefore

$$
\Gamma_\chi = \tau_\chi^{-1} = \frac{1}{1024\,\pi^3} \left(|y_+|^2 + 3\,|y_-|^2 \right) \frac{m_\chi^5}{M_{\rm Pl}^4} \, ,
\tag{6.22}
$$

For the sake of simplicity, we also assume the equality

$$
|y_+| = |y_-| \equiv y \, .
\tag{6.23}
$$

The introduction of A_4 symmetry requires a further modification concerning the Yukawa interactions in the leptonic sector. In the model, the charged lepton and light neutrino masses arise from the symmetry-invariant operators [292]

$$
\mathcal{L} \supset - \sum_{i=1,2,3} (y_e)_i \, \overline{L} H_i \ell + \sum_{i,j=1,2,3} (y_\nu)_{ij} \, \overline{L^c} H_i^{c*} H_j^{c\dagger} L + \text{h.c.} \, .
\tag{6.24}
$$

Once the three Higgs fields develop vacuum expectations values $\langle H_i \rangle = \left(0, v_i/\sqrt{2}\right)^T$, the lepton mass matrices are diagonal. In particular, they take the forms

$$
M_e = \begin{pmatrix} m_e & 0 & 0 \\ 0 & m_\mu & 0 \\ 0 & 0 & m_\tau \end{pmatrix}, \quad \text{and} \quad M_\nu = \begin{pmatrix} m_1 & 0 & 0 \\ 0 & m_2 & 0 \\ 0 & 0 & m_3 \end{pmatrix},
\tag{6.25}
$$

where the entries of M_e and M_ν are given by particular combinations of the three vacuum expectation values, the couplings $(y_e)_i$ and $(y_\nu)_{ij}$, and the phase ω. Since the matrices

are diagonal, the model does not allow for the lepton mixing that is however observed in several experiments. The neutrino oscillation parameters can be originated by introducing an extra Higgs-like field belonging to a A_4 triplet or a $SU_L(2)$ triplet scalar [292]. These new fields provide new channels for DM decays that have to be suppressed by invoking new symmetries (like Z_2) or by assuming very small couplings (compared to y_+ and y_-). However, the fit of the neutrino oscillation parameters in the framework of the A_4 model discussed here is not the topic of the thesis.

6.2   Fit with IceCube 3-year HESE data

Let us now constrain the two leptophilic models (*model 1* and *model 2* for $U_f(1)$ and A_4 symmetries, respectively) based on the operator given in Eq. (6.3). As for the previous analyses, we consider a two-component neutrino flux described by Eq. (5.10), where one contribution comes from astrophysical sources and the other one is originated by DM decays induced by the operators (6.5) (model 1) and (6.20) (model 2). The astrophysical neutrino flux is parametrized either by an unbroken power-law (4.10) (UPL) or by a broken power-law (4.12) (BPL). In case of the BPL parametrization, we fix the value of E_ν^{max} to be equal to 125 TeV according to the prediction of extragalactic SNRs [211]. Moreover, we restricted the spectral index to the range $\gamma \in [2,3]$. This allows us to cover a wide range of accelerator mechanisms related to the different astrophysical sources (*p-p* and *p-γ* processes). In this analysis, we focus on the scenario where the DM signal is mostly concentrated at very high energies, namely the three PeV neutrinos are related to DM decays. Hence, we consider DM masses in a range [1 PeV,10 PeV]. The peculiar features of the decay channels considered (peaked and spread flux due to primary neutrinos produced in the three-body decays, with sharp cut-off at $E_\nu = m_\chi/2$) are well in agreement with the IceCube observations at PeV energy scale.

The fit on the IceCube 3-year HESE data [238] has been performed by maximizing the multi-Poisson likelihood (4.18). We find the best-fit values in correspondence of $m_\chi = 5.0$ PeV, independently of the model adopted, and $\gamma = 3.0$ and $\gamma = 2.0$ for UPL and BPL cases, respectively. The marginalized 95% intervals for the parameters of the fit

DM Model	Astrophysical flux	$y\,[10^{-5}]$	$J_0\,[10^{-8}\,\mathrm{GeV/cm^2/s/sr}]$	χ^2/dof
model 1	UPL	$1.0^{+0.7}_{-0.7}$	$0.8^{+1.0}_{-0.5}$	$10.3/12$
	BPL	$1.1^{+0.6}_{-0.5}$	$2.5^{+2.8}_{-2.1}$	$9.2/12$
model 2	UPL	$0.35^{+0.21}_{-0.21}$	$0.8^{+1.0}_{-0.5}$	$10.7/12$
	BPL	$0.37^{+0.17}_{-0.16}$	$2.4^{+2.8}_{-2.0}$	$9.6/12$

Table 6.4: Marginalized 95% C.L. for the coupling y and the astrophysical flux normalization $J_0 = \Phi^0_{\mathrm{astro}} \times (10^5\,\mathrm{GeV})^2$ for all the scenarios analyzed. The last column reports the values of the reduced χ^2.

(DM-SM coupling y and the normalization of the astrophysical flux expressed in terms of $J_0 = \Phi^0_{\mathrm{astro}} \times (10^5\,\mathrm{GeV})^2$) are reported in Tab. 6.4 for all the cases considered. It is worth observing that the IceCube data slightly prefer the BPL scheme with respect to the UPL one, providing the former smaller values for reduced χ^2 than the latter. However, the two astrophysical models essentially have similar features at the level of produced neutrino flux, and a significant difference cannot be appreciated. We highlight that in each case a non-vanishing contribution from DM decays is required at 2σ level. In other words, the coupling y is not compatible with zero whiting 2σ. This is mainly due to the presence of the sharp cut-off in the neutrino data at high energy. In each case, the total energy injected by DM decay in the electromagnetic sector is smaller than the bound provided by Fermi-LAT experiment [216], as we already expected in case of leptophilic decay channels.

In the upper panels of Fig. 6.1 they are reported the number of neutrino events for two-component neutrino flux for the model 1 in case of the two different parameterizations of the astrophysical component. The lower panels, instead, show the 68% C.L. (dashed) and 95% C.L. (solid) contours of the marginalized likelihood in the y–J_0 plane. The crosses represent the best-fit points. The same plots for the fit of the model 2 based on the A_4 symmetry are reported in Fig. 6.2. It is worth observing that there is no significant difference between
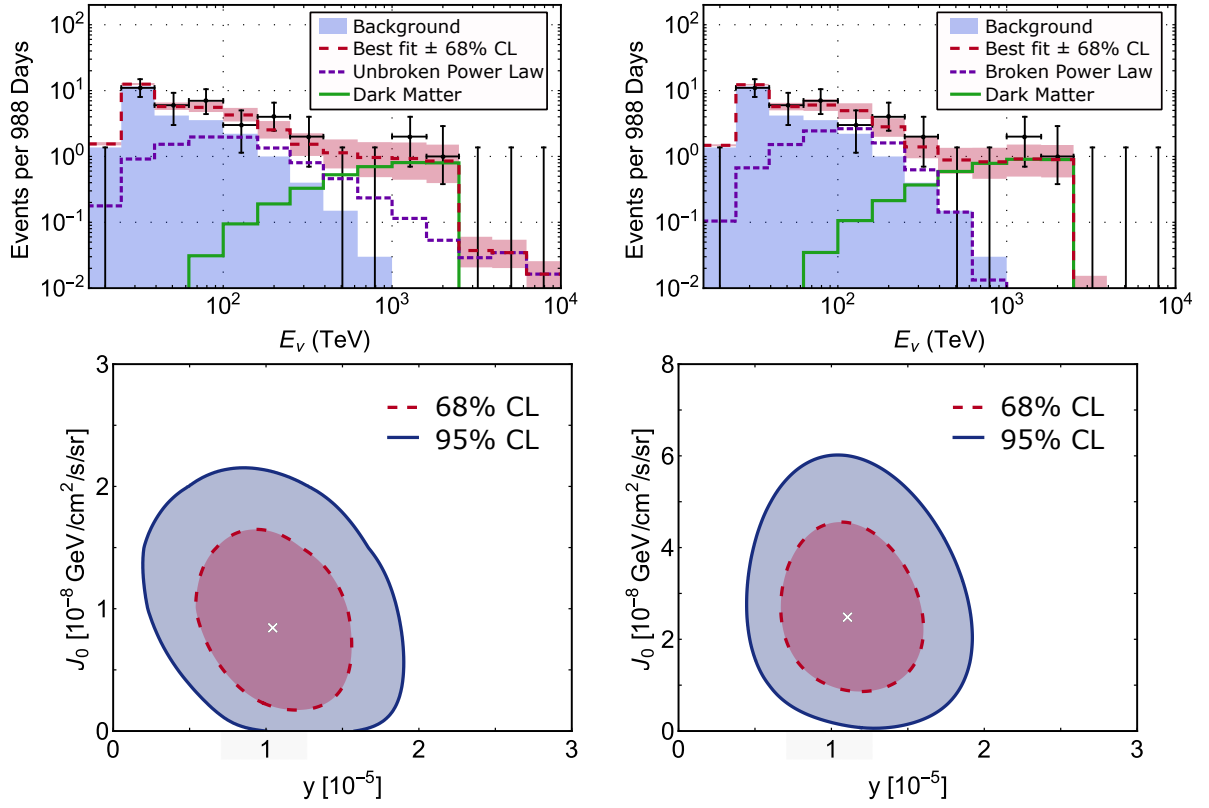
Figure 6.1: Results for the fit of the two-component neutrino flux for the model 1 and the two astrophysical parameterizations: the unbroken power-law (left panels) and the broken one (right panels). In the upper panels (neutrino energy spectrum), the red (long-dashed) line is the best-fit, and its band represents the 68% C.L. resulting from the fit. The purple (dashed) and green (solid) lines are the astrophysical and DM contributions, respectively. The black points are the IceCube 3-year HESE data with the blue regions showing the upper limit for the atmospheric background. The lower panels show the 68% C.L. (dashed) and 95% C.L. (solid) contours for the two parameters y and $J_0 = \Phi^0_{\text{astro}} \times (10^5 \, \text{GeV})^2$.

the two models. Indeed, both two models predict the observation of neutrinos in the energy range [0.3 PeV, 1.0 PeV] and a sharp cut-off at the energy of few PeV in correspondence of $m_\chi/2$. Since the galactic and extragalactic components of the DM neutrino flux are of the same order of magnitude (roughly 2/3 and 1/3 respectively), we expect an almost isotropic neutrino flux with a significant level of anisotropy near the galactic center.

In order to better understand the similarities of the two models, we also characterized
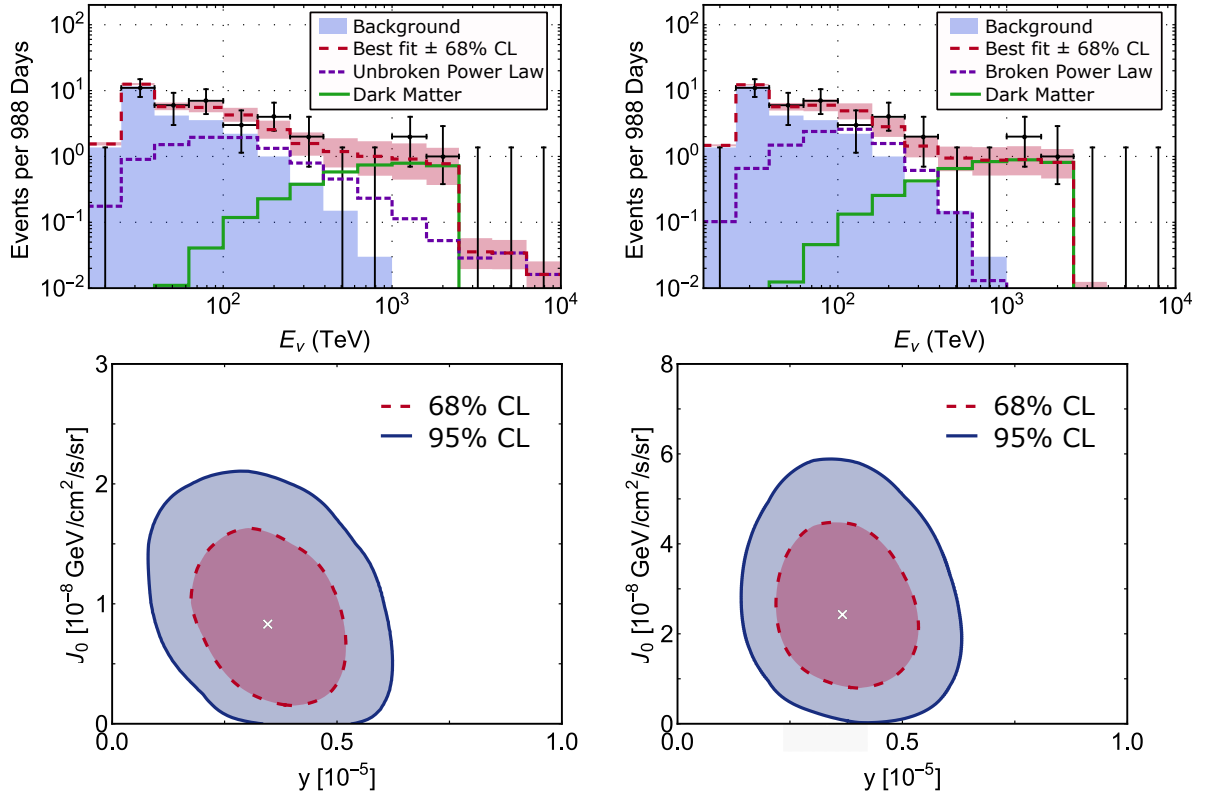
Figure 6.2: The description is the same of Fig. 6.1, but for the case of model 2.

two different realizations of the operator of Eq. (6.3) where only one coupling is non-zero. In particular, we study the couplings with flavors $\{\alpha, \beta, \gamma\} \equiv \{e, e, e\}$ and $\{\alpha, \beta, \gamma\} \equiv \{\tau, \tau, \tau\}$, since they represent two extreme cases with the minimum and maximum production of secondary neutrinos, respectively. In the left panel of Fig. 6.3 we show the flavor compositions at the Earth of the DM neutrino flux for model 1 and 2, and the two fully diagonal cases (e, e, e) and (τ, τ, τ) as well. In the plot, the black dot is the best-fit of the IceCube flavor analysis [300]. Only the diagonal case (e, e, e) leads at Earth to the flavor composition $(f_e : f_\mu : f_\tau)_\oplus \approx (0.55 : 0.19 : 0.26)$, while the other scenarios correspond to $(f_e : f_\mu : f_\tau)_\oplus \approx (1/3 : 1/3 : 1/3)$. In the right panel of Fig. 6.3 one can see that the DM neutrino flux is not appreciably affected by the choice of the flavor structure of the operator (6.3).
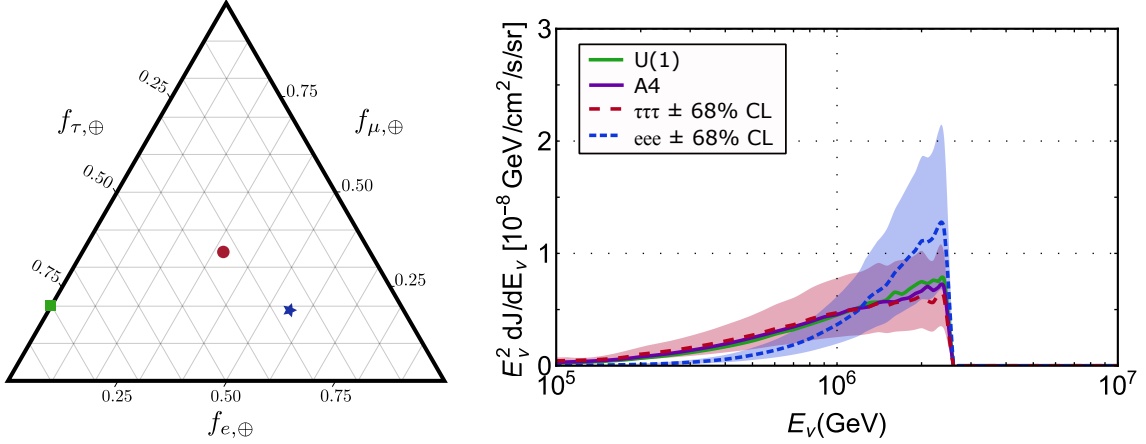
Figure 6.3: *Left*: Flavor compositions at Earth of the different DM models. Model 1, model 2 and the (τ, τ, τ) case are represented by the red disk, whereas the blue star stands for the (e, e, e) case. The green square shows the best-fit of the IceCube analysis on neutrino flavors [300]. *Right*: DM neutrino flux for model 1 (green, solid), model 2 (purple, solid), (e, e, e) (blue, dashed), and (τ, τ, τ) (red, long-dashed). The two 68 % C.L. bands refer to the two cases (e, e, e) and (τ, τ, τ).

6.3   Dark Matter production

Let us now discuss how these very heavy DM particles can be produced in the early Universe. The standard production mechanism of the thermal freeze-out [120, 121, 122] does not work in the case at hand for two reasons:

- the interaction strength required to produce DM would be so large that the DM decay would proceed much too fast;

- the DM mass is so large that the particle would be kinematically not accessible at too early times, implying an overclose the Universe.

On the other hand, the production mechanism of *freeze-in* from the thermal bath is a very good alternative [117]. In such a case, the interactions of the DM particles are so feeble that they never reach the thermal equilibrium with the plasma. The DM particles are instead gradually produced at temperatures $T \gg m_\chi$ from the thermal bath, and

simply remain present in the Universe because the rate of the back-reactions is too small or their decays proceed too slowly. A sizable DM abundance can be built up until $T \sim m_\chi$, temperature at which the DM particles become kinematically hard to access. The DM candidates that are produced through the freeze-in mechanism are in general called 'Feebly Interacting Massive Particles" (FIMPs). It is worth underlining that such a mechanism provides a *non-thermal* spectrum [118]. However, in case of very heavy DM particles, their distribution is peaked towards non-relativistic velocities (cold DM), independently from the details of the spectrum. The freeze-in production mechanism of DM particles providing a signal at IceCube is already proposed in Ref.s [301, 302, 303]. However, differently from Ref. [301] which investigates a full model based on left-right symmetry, we characterize the most minimal framework where the same operators relevant for the DM production are responsible for its indirect detection at Neutrino Telescopes.

In order to compute the DM production accurately, we need to find a viable UV-completion behind the effective operator given in Eq. (6.3). Hence, we introduce an electrically charged and $SU(2)_L$ singlet scalar S^+. This new scalar features a (potentially) lepton number violating coupling

$$\lambda_{\alpha\beta}\overline{L_\alpha^c}i\sigma_2 L_\beta S^+ + \text{h.c.} . \tag{6.26}$$

Such a coupling is similar to the one adopted in the Zee-Babu model [304, 305, 306].[2] Furthermore, the new particle $S^\pm$ can couple to the DM particle χ according to the operator

$$\lambda'_\gamma\overline{\ell_\gamma}\chi S^- + \text{h.c.} . \tag{6.27}$$

Thus, for a very heavy particle $S^\pm$ of mass M_S, the following effective operator is generated once the charged scalar is integrated out.

$$\frac{\lambda_{\alpha\beta}\lambda'_\gamma}{M_S^2}\left(\overline{L_\alpha^c}i\sigma_2 L_\beta\right)\left(\overline{\ell_\gamma}\chi\right) + \text{h.c.} . \tag{6.28}$$

---

[2]The Zee-Babu model was introduced to explain the smallness of neutrino masses, which are generated only at 2-loop level. This model contains two $SU(2)$ singlet scalars, one of which is doubly charged while the other one carries a single electric charge. The latter carries the same quantum numbers as S^+ in Eq. (6.26). This model is particularly interesting in what concerns its lepton flavor violation [307] and collider phenomenology [308, 309], which is linked to the light neutrino masses [310]. Note that, differently from our setup, the Zee-Babu model does not contain total singlet fermion fields, although it can be extended to accommodate for a DM candidate [311].

Such an operator is phenomenologically equivalent to the one provided in Eq. (6.3) with the relation

$$\frac{\lambda_{\alpha\beta}\lambda'_{\gamma}}{M_S^2} \quad \longleftrightarrow \quad \frac{y_{\alpha\beta\gamma}}{M_{\rm Pl}^2}. \tag{6.29}$$

In order to forbid the Yukawa-like interaction of Eq. (6.1) we can invoke the A_4 symmetry, assuming that the $S^{\pm}$ belongs to the triplet irreducible representation of the discrete symmetry, namely $S^+ = (S_1^+, S_2^+, S_3^+) \sim \mathbf{3}$. Under this assignment, the operator $\overline{L}H_{(1,2,3)}\chi$ is forbidden at tree-level, because it would transform as $\mathbf{3} \otimes (\mathbf{1}, \mathbf{1}', \mathbf{1}'') \otimes \mathbf{1} \not\supset \mathbf{1}$, while $\left(\overline{(L)^c}i\sigma_2 L\right)\left(\overline{\ell}\chi\right) \sim (\mathbf{3} \otimes \mathbf{3}) \otimes (\mathbf{3} \otimes \mathbf{1}) \supset \mathbf{3} \otimes \mathbf{3} \supset \mathbf{1}$. However, once the vacuum expectation values $\langle H_{2,3}\rangle$ break the A_4 symmetry, the dimension-4 operator $\overline{L}H_{(1,2,3)}\chi$ is generated at 1-loop level by gluing together the vertexes $\overline{\ell}\chi S$, $\overline{L}H\ell$, and $\overline{(L)^c}LS$. Then, the resulting dimension-4 operator only arises at one-loop level and it is suppressed by being proportional to the product of three tiny couplings, whereas the operator (6.28) is only suppressed $\lambda\lambda'$.

Given the operators of Eq.s (6.26) and (6.27) that depends on two masses (m_χ and M_S) and on two couplings ($\lambda_{\alpha\beta}$ and λ'_γ), we now report all the processes that are responsible for the production and the decay of DM particles.

6.3.1 The relevant processes for production and decay

There exist four different classes of processes (see Fig. 6.4 for Feynman diagrams of the last three processes are depicted explicitly, while S-decay would simply correspond to the "right half" of the leftmost diagram) that provide a contribution to the DM production in the early Universe:

- *decays of S particles*, $S^{\pm} \to \ell^{\pm}\chi$, which are in thermal equilibrium with the thermal bath due to the hypercharge interactions. These processes are proportional to $\left|\lambda'_\gamma\right|^2$;

- *s-channel* processes like $\nu_\alpha^c + \overline{\ell_\beta} \to \overline{\ell_\gamma} + \chi$, whose squared matrix elements are proportional to $4\left|\lambda_{\alpha\beta}\lambda'_\gamma\right|^2$;

- *t-channel* processes like $\nu_\alpha^c + \ell_\gamma \to \ell_\beta + \chi$ and $\overline{\ell_\beta} + \ell_\gamma \to \overline{\nu_\alpha^c} + \chi$, whose squared matrix elements are again proportional to $4\left|\lambda_{\alpha\beta}\lambda'_\gamma\right|^2$;

(a) *s*-channel   (b) *t*-channel   (c) Annihilation
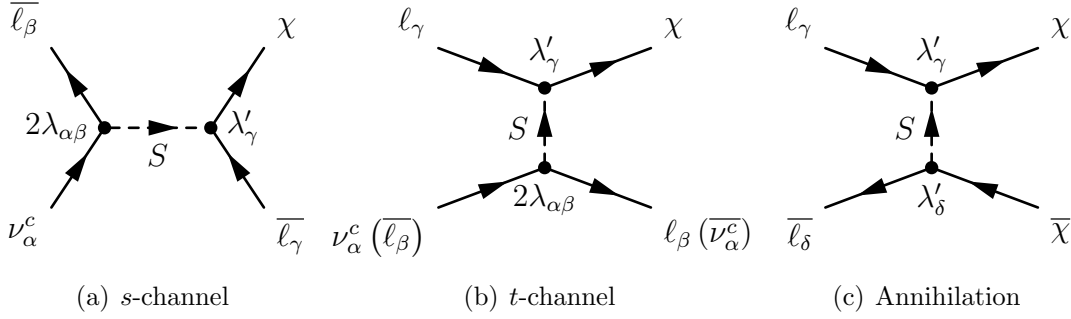
Figure 6.4: Three of the four Feynman diagrams responsible for the DM production.

- *annihilation* processes like $\ell_\gamma + \overline{\ell_\delta} \to \chi + \overline{\chi}$, whose squared amplitudes are weighted by $\left| \lambda'_\gamma \lambda'_\delta \right|^2$.

It is worth noticing that the coupling $\lambda_{\alpha\beta}$ is anti-symmetric in α and β, due to the structure of the operator in Eq. (6.26), while a factor of 2 arises from the singlet combination of two $SU(2)$ doublets. We have 18 different flavor combinations for the *s*-channel processes and for the *t*-channel ones, while the number of different flavor annihilation processes is 9.

Since the scalar particles S carry a hypercharge equal to unity, they can interact with the SM particles through the hypercharge interactions mediated by the $U(1)_Y$ gauge boson B_μ. Due to the strength of the hypercharge interactions, the S particles quickly reach the thermal equilibrium and follow a thermal distribution. Once the scalars decouple from the thermal bath and freeze-out, they can decay to SM particles or DM particles, providing a contribution to the DM relic abundance.

Indeed, in our setting the scalar $S^\pm$ has at least two decay channels,

$$S^\pm \to \ell_\alpha^\pm + \nu_\beta \; (\overline{\nu}_\beta) \qquad \text{and} \qquad S^\pm \to \ell_\gamma^\pm + \chi \; (\overline{\chi}) \quad [\text{if } M_S > \chi] , \qquad (6.30)$$

where the second channel is of course only accessible if the mass of $S^\pm$ is larger than the sum of the mass of all its decay products. Even though the scalar particles S^+ can also decay into further (e.g. non-SM) particles, here we focus our attention only on the most minimal setting provided by Eq.s (6.28), (6.26), and (6.27). In this case, the total decay width Γ_S of S particles for $M_S > m_\chi$, is equal to

$$\Gamma_S = \Gamma_{S \to \ell\nu} + \Gamma_{S \to \ell\chi} , \qquad (6.31)$$

where

$$\Gamma_{S \to \ell \nu} = \frac{1}{2\pi} \left(\sum_{\alpha=e,\mu,\tau} \sum_{\beta \neq \alpha} |\lambda_{\alpha\beta}|^2 \right) M_S, \tag{6.32}$$

$$\Gamma_{S \to \ell \chi} = \frac{1}{8\pi} \left(\sum_{\gamma=e,\mu,\tau} |\lambda'_\gamma|^2 \right) \frac{\left(M_S^2 - m_\chi^2 \right)^2}{M_S \left(M_S^2 + m_\chi^2 \right)}. \tag{6.33}$$

In order to take into account the contribution of S decays, we have to solve the Boltzmann equation for S particles. It has the form

$$\frac{dY_S}{dT} = \frac{\mathfrak{s} \langle \sigma v \rangle_{\text{hyper.}}}{T \, \mathcal{H}} \left[Y_S^2 - (Y_S^{\text{eq}})^2 \right] + \frac{\langle \Gamma \rangle_{S \to \ell \nu}}{T \, \mathcal{H}} \left[Y_S - Y_S^{\text{eq}} \right] + \frac{\langle \Gamma \rangle_{S \to \ell \chi}}{T \, \mathcal{H}} Y_S, \tag{6.34}$$

where Y^{eq} is the equilibrium yield of S particles. The first term in the right-hand side of the expression is related to the hypercharge processes $S^+ S^- \leftrightarrow BB$ and $S^+ S^- \leftrightarrow f\bar{f}$ (f stands for any SM particle), and it depends on the thermally averaged cross-section

$$\langle \sigma v \rangle_{\text{hyper.}} = \frac{2\pi \alpha_y^2}{M_S^2} \left[\frac{y_S^2 \left(\sum_f n_f y_f^2 \right)}{16} + 4 y_S^4 \right] \left[\frac{K_1 \left(M_S/T \right)}{K_2 \left(M_S/T \right)} \right]^2, \tag{6.35}$$

where $\alpha_y^{-1} = 59.008$ is the hypercharge gauge coupling at the electroweak scale,[3] the quantity y_f is the hypercharge of the SM multiplet f ($y_S = 1$), and n_f is its multiplicity under the SM gauge group (e.g., $n_u = 3$ for an up-quark u or $n_e = 1$ for an electron e^-). Moreover, the functions K_1 and K_2 are the first and second modified Bessel functions, respectively. The second and third terms on the right-hand side of Eq. (6.34) correspond instead to the processes $S^\pm \leftrightarrow \ell^\pm \nu$ and $S^\pm \to \ell^\pm \chi$, respectively.[4] In particular, we have

$$\langle \Gamma \rangle_{S \to \ell \nu} = \frac{K_1 \left(M_S/T \right)}{K_2 \left(M_S/T \right)} \Gamma_{S \to \ell \nu} \quad \text{and} \quad \langle \Gamma \rangle_{S \to \ell \chi} = \frac{K_1 \left(M_S/T \right)}{K_2 \left(M_S/T \right)} \Gamma_{S \to \ell \chi}. \tag{6.36}$$

Therefore, the Boltzmann equation for the DM particles consists of four terms. It is given by

$$\frac{dY_\chi}{dT} = \left. \frac{dY_\chi}{dT} \right|_{S \text{ dec.}} + \left. \frac{dY_\chi}{dT} \right|_{s\text{-ch.}} + \left. \frac{dY_\chi}{dT} \right|_{t\text{-ch.}} + \left. \frac{dY_\chi}{dT} \right|_{\text{annih.}}, \tag{6.37}$$

---

[3]Considering the running of the gauge coupling corresponds to a rescaling of the new couplings involved in DM production.

[4]We do not consider the inverse decay process $\ell^\pm \chi \to S^\pm$, since the number density of DM particles is negligible in the early Universe due to the feebleness of couplings involved.

where the four terms correspond to the four different classes of processes previously listed. The first term is given by

$$\left.\frac{\mathrm{d}Y_\chi}{\mathrm{d}T}\right|_{S\,\mathrm{dec.}} = -\frac{\langle\Gamma\rangle_{S\to\ell\chi}}{T\,\mathcal{H}}Y_S\,, \tag{6.38}$$

while the other three terms take the form

$$\left.\frac{\mathrm{d}Y_\chi}{\mathrm{d}T}\right|_i = -\frac{1}{512\pi^6\mathcal{H}\mathfrak{s}}\int ds\,d\Omega\,\frac{W_i}{\sqrt{s}}K_1\left(\frac{\sqrt{s}}{T}\right)\,. \tag{6.39}$$

For each process the quantities W_i are equal to

$$W_{\text{s-ch.}} = \sum_{\alpha,\gamma=e,\mu,\tau}\sum_{\beta\neq\alpha}W_{\nu_\alpha^c\overline{\ell_\beta}\to\overline{\ell_\gamma}\chi}\,, \tag{6.40}$$

$$W_{\text{t-ch.}} = \sum_{\alpha,\gamma=e,\mu,\tau}\sum_{\beta\neq\alpha}\left[W_{\nu_\alpha^c\ell_\gamma\to\ell_\beta\chi}+W_{\overline{\ell_\beta}\ell_\gamma\to\overline{\nu_\alpha^c}\chi}\right]\,, \tag{6.41}$$

$$W_{\text{annih.}} = \sum_{\gamma,\delta=e,\mu,\tau}W_{\ell_\gamma\overline{\ell_\delta}\to\chi\overline{\chi}}\,. \tag{6.42}$$

The functions $W_{ij\to kl}$ in these expressions are given by

$$W_{ij\to kl} = g_i g_j P_{ij}P_{kl}\,|\mathcal{M}|^2_{ij\to kl}\,, \tag{6.43}$$

where the squared matrix element $|\mathcal{M}|^2$ is summed over initial and final spin degrees of freedom g and averaged over initial ones, and

$$P_{ij} = \frac{[s-(m_i+m_j)^2]^{1/2}\,[s-(m_i-m_j)^2]^{1/2}}{2\sqrt{s}}\,, \tag{6.44}$$

where s is the centre-of-mass energy and m_i is the mass of particle i. Under the reasonable approximation of massless in- and out-going SM particles, denoting with θ the scattering angle we have

$$|\mathcal{M}|^2_{\nu_\alpha^c\overline{\ell_\beta}\to\overline{\ell_\gamma}\chi} = \frac{\left|\lambda_{\alpha\beta}\lambda_\gamma'\right|^2}{4}\frac{s\left(s-m_\chi^2\right)}{\left(s-M_S^2\right)^2}\,, \tag{6.45}$$

$$|\mathcal{M}|^2_{\nu_\alpha^c\ell_\gamma\to\ell_\beta\chi} = \frac{\left|\lambda_{\alpha\beta}\lambda_\gamma'\right|^2}{4}\frac{\left(s-m_\chi^2\right)\left[s\left(1-\cos\theta\right)+m_\chi^2\left(1+\cos\theta\right)\right]\left(1-\cos\theta\right)}{\left[\left(s-m_\chi^2\right)\left(1-\cos\theta\right)+2M_S^2\right]^2}\,, \tag{6.46}$$

$$|\mathcal{M}|^2_{\overline{\ell_\beta}\ell_\gamma\to\overline{\nu_\alpha^c}\chi} = |\mathcal{M}|^2_{\nu_\alpha^c\ell_\gamma\to\ell_\beta\chi}\,, \tag{6.47}$$

$$|\mathcal{M}|^2_{\ell_\gamma\overline{\ell_\delta}\to\chi\overline{\chi}} = \frac{\left|\lambda_\gamma'\lambda_\delta'\right|^2}{4}\frac{s\left[s\left(1+\cos^2\theta\right)-4m_\chi^2\cos^2\theta-2\sqrt{s\left(s-m_\chi^2\right)}\cos\theta\right]}{\left[s-\sqrt{s\left(s-m_\chi^2\right)}\cos\theta+2\left(M_S^2-m_\chi^2\right)\right]^2}\,. \tag{6.48}$$

(a) $M_S < m_\chi$ (b) $M_S > m_\chi$ (off-shell for $M_S < m_\chi$)

Figure 6.5: DM decay channels due to the coupling leading to the effective operator (6.28).

The DM relic abundance is then obtained by plugging Eq. (6.37) into Eq. (2.9) and numerically performing the integral over x. As will be shown later, the contribution to the DM relic abundance from the S decays is the dominant one in the region $M_S > m_\chi$. Depending on the strength of the quantities reported in Eqs. (6.35) and (6.36), the S particles can freeze-out from the thermal bath or freeze-in at a temperature $T = T^*$. Therefore, if the decays of scalar mediators become efficient ($\langle \Gamma \rangle_S > \mathcal{H}$) for $T \gg T^*$, by taking $Y_S^{\mathrm{eq}} \sim 0$ in Eq. (6.34) and using Eq. (6.38), one can obtain the following analytically approximated expression for the DM relic abundance.

$$\Omega_{\mathrm{DM}} h^2 \big|_{S \text{ dec.}} \simeq \frac{2 m_\chi \mathfrak{s}_0}{\rho_{\mathrm{crit}}/h^2} \frac{\Gamma_{S \to \ell \chi}}{\Gamma_S} Y_S (T^*) . \tag{6.49}$$

The s-channel processes, instead, provide a sub-dominant contribution, while the contributions of the other two processes is negligible. In case of s-channel processes, by using the narrow width approximation at the resonance $T \approx M_S$, one gets the following analytical expression for its contribution to the relic abundance of χ particles.

$$\frac{\Omega_{\mathrm{DM}} h^2 \big|_{s\text{-ch.}}}{0.1188} = \begin{cases} \left(\frac{106.75}{g_*}\right)^{3/2} \left(\frac{\sum_{\alpha,\gamma=e,\mu,\tau} \sum_{\beta \neq \alpha} |\lambda_{\alpha\beta} \lambda'_\gamma|^2}{1.10 \times 10^{-21}}\right) & \text{for } M_S < m_\chi , \\[3ex] \left(\frac{106.75}{g_*}\right)^{3/2} \left(\frac{\sum_{\alpha,\gamma=e,\mu,\tau} \sum_{\beta \neq \alpha} |\lambda_{\alpha\beta} \lambda'_\gamma|^2}{3.72 \times 10^{-23}}\right) \frac{\left(M_S^2 - m_\chi^2\right)^2}{M_S^4} \frac{m_\chi}{\Gamma_S} & \text{for } M_S > m_\chi , \end{cases} \tag{6.50}$$

where Γ_S is the total decay width of S particles and it is provided in Eq. (6.31). In our setting, the χ particles decay through the processes depicted in Fig. 6.5, for both cases

where $M_S < m_\chi$ and $M_S > m_\chi$. The total decay width of χ particles is therefore given by

$$
\Gamma_\chi = \begin{cases} \sum_{\gamma=e,\mu,\tau} \frac{|\lambda'_\gamma|^2}{16\pi} m_\chi & \text{for } M_S \ll m_\chi, \\[3mm] \sum_{\alpha,\gamma=e,\mu,\tau} \sum_{\beta\neq\alpha} \frac{|\lambda_{\alpha\beta}\lambda'_\gamma|^2}{1536\pi^3} \frac{m_\chi^5}{M_S^4} & \text{for } M_S \gg m_\chi. \end{cases}
\tag{6.51}
$$

All the previous expressions have been evaluated in case of Dirac DM particles, but the final results does not change for Majorana particles.

In the numerical analysis we will present later, for the sake of simplicity we assume that all the couplings are of the same order of magnitude, independently of the flavor structure. This means that

$$
\lambda_{\alpha\beta} \equiv \lambda \qquad \text{and} \qquad \lambda'_\gamma \equiv \lambda'.
\tag{6.52}
$$

If this relation is only approximately fulfilled, each process with a different flavor structure would lead to a different contribution to the DM relic abundance. In particular, in the case of large hierarchies among the couplings $\lambda_{\alpha\beta}$, only the processes proportional to larger couplings would be significant for DM production. On the other hand, we have seen in Fig. 6.3 that, due to neutrino oscillations, the IceCube observations are not very sensitive to different flavor structures of DM decays, except for the case where $\chi \to e^+ e^- \nu_e$ is the only allowed decay channel.

Under the reasonable assumptions of equality among the couplings, we will show in the next section that the observed DM relic abundance is obtained if $\lambda \gg \lambda'$. By using this relation, from Eq. (6.49) we obtain

$$
\Omega_{\text{DM}} h^2 \big|_{S \text{ dec.}} = 0.1188 \left(\frac{|\lambda'|/|\lambda|}{4.2 \times 10^{-8}} \right)^2 \left(\frac{m_\chi}{1 \text{ PeV}} \right) \frac{(M_S^2 - m_\chi^2)^2}{M_S^4} Y_S(T^*).
\tag{6.53}
$$

This quantity depends on the ratio between the two couplings λ and λ', being the contribution of Eq. (6.49) proportional to the branching ratio $\Gamma_{S \to \ell\chi}/\Gamma_S$. On the other hand, the s-channel contribution is solely proportional to the coupling λ' and, for $M_S > m_\chi$, it is given by

$$
\Omega_{\text{DM}} h^2 \big|_{s\text{-ch.}} = 0.1188 \left(\frac{106.75}{g_*} \right)^{3/2} \left(\frac{|\lambda'|}{1.0 \times 10^{-12}} \right)^2 \frac{m_\chi}{M_S} \frac{(M_S^2 - m_\chi^2)^2}{M_S^4}.
\tag{6.54}
$$

6.3.2 Numerical results

Let us now show that in our minimal setting the operators of Eq.s (6.26), (6.27), and (6.28) are able to account for the DM production in the early Universe and to provide a detectable signal at the IceCube Neutrino Telescopes. In particular, few constraints have to be fulfilled by varying the parameters of the setting:

- the model has to provide the correct observed DM relic abundance [85]

$$\Omega_{\text{DM}} h^2 = \Omega_{\text{DM}} h^2 \big|_{\text{obs}} = 0.1188 \pm 0.0010 \, ; \tag{6.55}$$

- the DM lifetime has to be larger than at least the age of the Universe

$$\tau_\chi \geq t_{\text{Universe}} \simeq 4.35 \times 10^{17} \, \text{sec} \, ; \tag{6.56}$$

- according to the results obtained by fitting the IceCube 3-year HESE data we fix the DM mass and lifetime to be equal to

$$m_\chi = 5 \, \text{PeV} \qquad \text{and} \qquad \tau_\chi = 10^{28} \, \text{sec} \, . \tag{6.57}$$

We note that in general the IceCube constraints on decaying DM scenarios are model-dependent, since the neutrino spectrum depends on the DM decay channels. However, the IceCube spectrum sets a lower bound on the DM lifetime of the order of 10^{28} sec, which is approximately model-independent. The reaming free parameters of such a numerical analysis are the mass of the charged scalar M_S and the two couplings λ and λ'. Moreover, we assume that the reheating temperature is above the mediator mass M_S.

In Fig. 6.6 we report the contributions of the four different classes of processes involved in the DM production as a function of the charged scalar mass M_S. For each value of M_S, the couplings λ and λ' are chosen in such a way that $\tau_\chi = 10^{28}$ sec and the sum of all the contributions (lines) satisfies the relation of Eq. (6.55). In the plot, the purple region on the left ($M_S \leq m_\chi$) is not allowed according to the requirement of Eq. (6.57). On the other side, the purple region on the right ($M_S > M_{\text{Planck}}$) represents the bound related to the Planck mass. The whole treatment is indeed valid for sub-Planckian scales only. The green
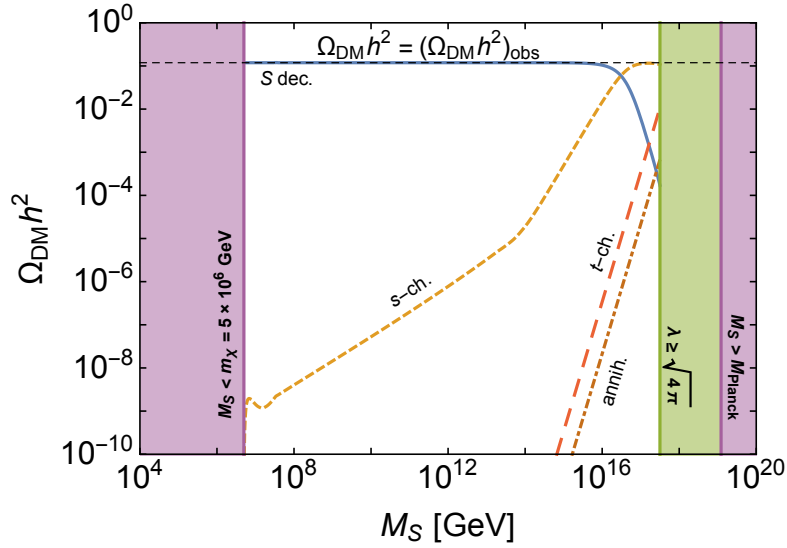
Figure 6.6: Contributions to the DM relic abundance as a function of the mass M_S. For each value of M_S, the couplings λ and λ' satisfy the conditions $\Omega_{\mathrm{DM}}h^2 = \Omega_{\mathrm{DM}}h^2|_{\mathrm{obs}}$ and $\tau_\chi = 10^{28}$ sec for $m_\chi = 5$ PeV.

region displays the choices of parameters where accouing for the observed DM abundance would require a non-perturbative coupling λ (i.e., larger than $\sqrt{4\pi}$). When all constraints are satisfied, we observe that there exist two different regimes:

- for $M_S \lesssim 10^{15}$ GeV, the decays of thermal scalar particles provide the main contribution;

- for $M_S \gtrsim 10^{15}$ GeV, there is a small region in which the s-channel processes dominate.

Hence, we have that for small values of M_S, the DM relic abundance is approximately given by Eq. (6.53), while for very large scalar masses it is provided by Eq. (6.54). The other two contributions (t-channel and annihilation processes) are always negligible with respect to the previous ones.

In the left panel of Fig. 6.7, they are reported the yields Y_S and Y_χ as a function of the variable $x = M_S/T$. The correct DM relic abundance is obtained by considering $M_S = 10^{10}$ GeV and by fixing the couplings λ and λ' to 1.0×10^{-10} and 1.3×10^{-15}, respectively. For any initial distribution, the S particles quickly reach the thermal equilibrium, implying
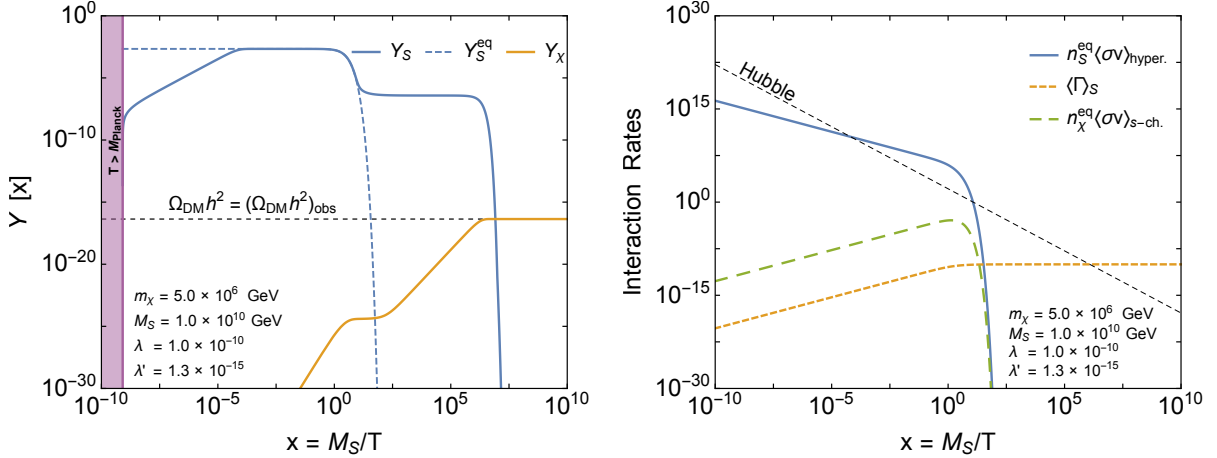
Figure 6.7: *Left*: yields of the S and χ particles as a function of the auxiliary variable $x = M_S/T$. *Right*: interaction rates of different processes involved in the Boltzmann equations (6.34) and (6.37). In both panels, the showed quantities are evaluated for $M_S = 1.0 \times 10^{10}$ GeV, $\lambda = 1.0 \times 10^{-10}$, and $\lambda' = 1.3 \times 10^{-15}$.

that the yield Y_S follows the equilibrium distribution Y_S^{eq} (dashed blue line in the plot). As the temperature decreases and the quantity x reaches approximately the value 10, the S scalars freeze-out from the thermal bath. Then, at very low temperatures $T \sim T_{\text{dec.}}$, they decay into SM and DM particles as soon as the decay rate becomes efficient ($\langle \Gamma \rangle_S > \mathcal{H}$). On the other hand, DM particles *freeze-in* at $T = T_{\text{dec.}}$, meaning that the yield Y_χ increases as the temperature of the bath decreases and becomes a constant for $T \leq T_{\text{dec.}}$.

The interaction rates $n^{\text{eq}} \langle \sigma v \rangle$ and $\langle \Gamma \rangle$ as functions of the auxiliary variable x are depicted in the right panel of Fig. 6.7. We remind that when an interaction rate is larger than the Hubble parameter $\mathcal{H}$ (dashed black line in the plot), the corresponding processes are efficient. Therefore, the hypercharge interactions (solid blue line) are able to couple the S particles with the thermal bath. By comparing the two plots in Fig. 6.7, we note that the region where $n_S^{\text{eq}} \langle \sigma v \rangle_{\text{hyper.}} \geq \mathcal{H}$ corresponds to the one where $Y_S = Y_S^{\text{eq}}$, and that the scalar particles decouple from the thermal bath when the interaction rate equals the Hubble parameter. Moreover, the plot shows also that the S decays occur once $\langle \Gamma \rangle_S \approx \mathcal{H}$. The interaction rate of s-channel processes is never larger than the Hubble parameter $\mathcal{H}$,
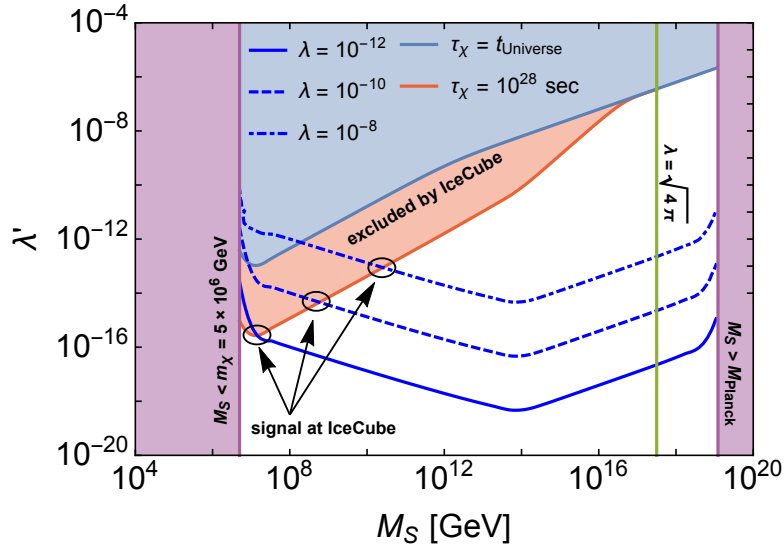
Figure 6.8: Allowed region of the parameter space. The excluded regions are related to the constraints coming from the age of the Universe (light blue), the IceCube data (red), and the Planck and DM mass (purple). The solid red line corresponds to $\tau_\chi = 10^{28}$ sec. The solid green line bounds from below the allowed values of M_S due to λ being non-perturbative in case of $\tau_\chi = 10^{28}$ sec. The blue lines display fixed values for the coupling λ. The intersections (circles) between the red line and the blue lines provide the values of M_S, λ and λ' that provide a correct DM production and an detectable signal at the IceCube Observatory.

implying that the DM particles indeed never reach the thermal equilibrium with the thermal bath. In particular, it firstly increases as T decreases for $T > M_S$ and then rapidly falls off. Note that the s-channel contribution corresponds to the first step in the behavior of the yield Y_χ. Moreover, one can observe that according to Fig. 6.6 the t-channel and annihilation processes are negligible with this choice of parameters. Furthermore, the DM particles freeze-in when $\langle \Gamma \rangle_S = \mathcal{H}$ occurring at $T = T_{\text{dec.}}$.

Fig. 6.8 shows the main result of this numerical analysis in the M_S–λ' plane. The three lines shown explicitly are related to different values of the coupling λ. The blue (red) region is excluded since $\tau_\chi < t_{\text{Universe}}$ ($\tau_\chi < 10^{28}$ sec). The solid red line corresponds to the relations given by Eq. (6.57). It is worth noting that IceCube data provide the most

stringent constraint on models for very heavy DM particles. The purple regions show the bounds related to the DM mass (left) and Planck mass (right), as already discussed. Thus, only the white region in the plot is allowed. The choices of parameters belonging to such a region provide viable DM production and a compatible signal with the IceCube observations.

It is worth underlining that only the values of M_S and λ' surrounding to the solid red line ($\tau_\chi = 10^{28}$ sec) are compatible with both fitting the PeV neutrinos and the DM production. The intersections (marked by the black circles) of the blue lines (i.e., the lines with given λ) with the red one provide the corresponding required values for the coupling λ. As can be seen in Fig. 6.8, the coupling λ' is smaller than λ according to Eq. (6.53). In particular, the requirement of perturbative coupling (green line in the plot) provides an *upper* bound on the scalar mass M_S and on the couplings λ' and λ. A *lower* bound for the values of the two couplings is instead obtained in correspondence of $M_S = 1.3 \times 10^7$ GeV where a minimum in λ' is shown in the plot. In the region $m_\chi \leq M_S \leq 1.3 \times 10^7$ GeV, the couplings indeed are larger than their minimum values due to the fact that the expression of Eq. (6.53) is proportional to the difference $(M_S - m_\chi)$. Thus, we find the following bounds:

- Upper bound $M_S \leq 3.2 \times 10^{17}$ GeV and $\lambda' \leq 3.4 \times 10^{-7}$, according to $\lambda \leq \sqrt{4\pi}$;

- Lower bound $\lambda' \gtrsim 2.7 \times 10^{-16}$ at $M_S = 1.3 \times 10^7$ GeV.

- Lower bound $\lambda \gtrsim 1.0 \times 10^{-13}$ for $M_S \to m_\chi$.

These bounds delimit the region of the three parameters M_S, λ, and λ', whose values are compatible at the same time with the DM production and a positive IceCube signal at PeV energy. Hence, when interpreting the high-energy neutrino events observed at IceCube Telescope as stemming from DM decay, no complicated new physics is required. Instead, a few simple additions to the Standard Model suffice to not only bring all the bounds in agreement but to also provide a potentially testable parameter space left to explore.

Finally, in Fig. 6.9, we illustrate the effect of Neutrino Telescope like IceCube on the parameter space. For a coupling $\lambda = 1.0 \times 10^{-10}$, we show the m_χ–M_S plane with λ' color-coded, with the different bounds on the DM lifetime. Most of the plane is, however, already
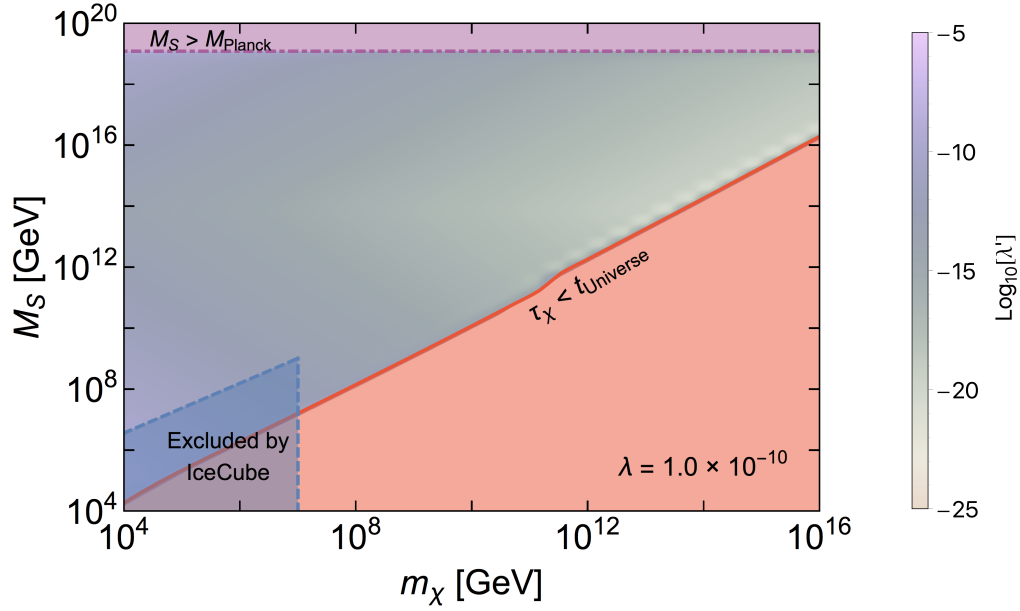
Figure 6.9: Illustration of the impact of Neutrino Telescopes like the IceCube experiments, shown for the example of $\lambda = 10^{-10}$. The red region is excluded because of $\tau_\chi < t_{\text{Universe}}$.

excluded by the requirement $m_\chi < M_S$. The IceCube bound can be avoided for large enough M_S or small enough λ', both providing a small decay rate. It is worth observing that there exist further constraints coming from cosmological arguments like reionization [312], which are strongly model-dependent, and from other astrophysical indirect signals like gamma-rays (see for instance Ref.s [277, 278]), that are not shown here.

Conclusions

Although the existence of dark matter is strongly suggested by several gravitational phenomena, we still know a very few about its nature. Among the numerous models proposed to allocate viable dark matter candidates, the most promising WIMP paradigm starts to be very constrained by all direct, indirect and colliders searches, especially focused on the GeV–TeV energy range. On the other hand, modern Neutrino and Gamma-ray telescopes are collecting new data that can potentially shed light on the nature of dark matter. Indeed, the latest astrophysical observations of high-energy neutrinos and gamma-rays provide the only viable way to look for alternatives to WIMPs having a mass larger than the TeV energy scale. The measurement of the diffuse TeV–PeV neutrino flux by the IceCube and ANTARES Neutrino Telescopes has trigged a huge debate in the scientific community about an intriguing relation between the origin of such high energy neutrinos and dark matter. Indeed, through its decays or annihilations, dark matter can provide a detectable contribution to the observed neutrino flux.

The aim of the thesis is to analyze the current neutrino and gamma-ray data in order to infer the properties of dark matter particles. In particular, we have focused on the 2–3σ low-energy excess (10–100 TeV) shown in the diffuse neutrino flux. Such an excess arises once a hard astrophysical power-law is considered, in agreement with gamma-rays and up-going muon neutrinos observations. The excess have been statistically characterized by using different IceCube data samples (MESE and HESE). Moreover, we have found that the tension with the single power-law assumption is strengthened once the latest IceCube data are combined with the ANTARES ones. This result strongly suggests that the diffuse neutrino flux has to be explained in terms of two different components.

Hence, we have deeply analyzed the scenario where the low-energy excess is due to dark matter. For this purpose, we have phenomenologically considered different models where dark matter particles decay or annihilate into leptonic or hadronic final states. In order to determine the statistical relevance of such a scenario, we have performed analyses on both the angular distribution and the energy spectrum of neutrinos observed by the IceCube telescope. The dark matter models are further constrained once the prediction for the flux of gamma-rays is compared with the corresponding measurements. In particular, we have found that the decaying models result to be less constrained than the annihilating ones, and the leptonic final states are favoured with respect to the hadronic ones, since they provide a smaller contribution to the gamma-ray flux. This result underlines the importance of multi-messenger analyses that at the same time take into account the prediction of both neutrino and gamma-ray fluxes produced by dark matter.

We have also examined an extension of the Standard Model, based on flavor symmetries, where a leptophilic dark matter candidate is predicted to have an observable signal at IceCube. The parameters of the model have been fitted to account for the three PeV neutrinos observed by IceCube. Moreover, in this theoretical framework, by solving the Boltzmann equations we have shown that the freeze-in mechanism is a viable mechanism to produce such very heavy dark matter particles in the early Universe. In particular, we have found that the same operator mediating dark matter decays into neutrinos is responsible for dark matter production. In such a way, we have provided the most minimal scenario allocating a dark matter candidate whose signal can be observed at IceCube.

Bibliography

[1] Sofiane M. Boucenna, Marco Chianese, Gianpiero Mangano, Gennaro Miele, Stefano Morisi, Ofelia Pisanti, and Edoardo Vitagliano. Decaying Leptophilic Dark Matter at IceCube. *JCAP*, 1512(12):055, 2015.

[2] Marco Chianese, Gennaro Miele, Stefano Morisi, and Edoardo Vitagliano. Low energy IceCube data and a possible Dark Matter related excess. *Phys. Lett.*, B757:251–256, 2016.

[3] Marco Chianese and Alexander Merle. A Consistent Theory of Decaying Dark Matter Connecting IceCube to the Sesame Street. *JCAP*, 1704(04):017, 2017.

[4] M. Chianese, G. Miele, and S. Morisi. Dark Matter interpretation of low energy IceCube MESE excess. *JCAP*, 1701(01):007, 2017.

[5] Marco Chianese, Rosa Mele, Gennaro Miele, Pasquale Migliozzi, and Stefano Morisi. Use of ANTARES and IceCube data to constrain single power-law neutrino flux. 2017.

[6] Marco Chianese, Gennaro Miele, and Stefano Morisi. Interpreting IceCube 6-year HESE data as an evidence for hundred TeV decaying Dark Matter. *Phys. Lett.*, B773:591, 2017.

[7] Zurab Berezhiani, Marco Chianese, Gennaro Miele, and Stefano Morisi. Chances for SUSY-GUT in the LHC Epoch. *JHEP*, 08:083, 2015.

[8] F. Buccella, M. Chianese, G. Mangano, G. Miele, S. Morisi, and P. Santorelli. A neutrino mass-mixing sum rule from SO(10) and neutrinoless double beta decay. *JHEP*, 04:004, 2017.

[9] Marco Chianese, Elisabetta Di Grezia, Mattia Manfredonia, and Gennaro Miele. Characterising exotic matter driving wormholes. *Eur. Phys. J. Plus*, 132(4):164, 2017.

[10] S. L. Glashow. Partial Symmetries of Weak Interactions. *Nucl. Phys.*, 22:579–588, 1961.

[11] Steven Weinberg. A Model of Leptons. *Phys. Rev. Lett.*, 19:1264–1266, 1967.

[12] Abdus Salam. Weak and Electromagnetic Interactions. *Conf. Proc.*, C680519:367–377, 1968.

[13] David J. Gross and Frank Wilczek. Ultraviolet Behavior of Nonabelian Gauge Theories. *Phys. Rev. Lett.*, 30:1343–1346, 1973.

[14] H. David Politzer. Reliable Perturbative Results for Strong Interactions? *Phys. Rev. Lett.*, 30:1346–1349, 1973.

[15] Steven Weinberg. Nonabelian Gauge Theories of the Strong Interactions. *Phys. Rev. Lett.*, 31:494–497, 1973.

[16] H. Fritzsch, Murray Gell-Mann, and H. Leutwyler. Advantages of the Color Octet Gluon Picture. *Phys. Lett.*, 47B:365–368, 1973.

[17] Peter W. Higgs. Broken symmetries, massless particles and gauge fields. *Phys. Lett.*, 12:132–133, 1964.

[18] F. Englert and R. Brout. Broken Symmetry and the Mass of Gauge Vector Mesons. *Phys. Rev. Lett.*, 13:321–323, 1964.

[19] G. S. Guralnik, C. R. Hagen, and T. W. B. Kibble. Global Conservation Laws and Massless Particles. *Phys. Rev. Lett.*, 13:585–587, 1964.

[20] Georges Aad et al. Observation of a new particle in the search for the Standard Model Higgs boson with the ATLAS detector at the LHC. *Phys. Lett.*, B716:1–29, 2012.

[21] Serguei Chatrchyan et al. Observation of a new boson at a mass of 125 GeV with the CMS experiment at the LHC. *Phys. Lett.*, B716:30–61, 2012.

[22] Chen-Ning Yang and Robert L. Mills. Conservation of Isotopic Spin and Isotopic Gauge Invariance. *Phys. Rev.*, 96:191–195, 1954.

[23] Abdus Salam and John Clive Ward. Electromagnetic and weak interactions. *Phys. Lett.*, 13:168–171, 1964.

[24] Gerard 't Hooft and M. J. G. Veltman. Regularization and Renormalization of Gauge Fields. *Nucl. Phys.*, B44:189–213, 1972.

[25] Yoichiro Nambu. Quasiparticles and Gauge Invariance in the Theory of Superconductivity. *Phys. Rev.*, 117:648–663, 1960.

[26] J. Goldstone. Field Theories with Superconductor Solutions. *Nuovo Cim.*, 19:154–164, 1961.

[27] Jeffrey Goldstone, Abdus Salam, and Steven Weinberg. Broken Symmetries. *Phys. Rev.*, 127:965–970, 1962.

[28] C. Patrignani et al. Review of Particle Physics. *Chin. Phys.*, C40(10):100001, 2016.

[29] Nicola Cabibbo. Unitary Symmetry and Leptonic Decays. *Phys. Rev. Lett.*, 10:531–533, 1963. [,648(1963)].

[30] Makoto Kobayashi and Toshihide Maskawa. CP Violation in the Renormalizable Theory of Weak Interaction. *Prog. Theor. Phys.*, 49:652–657, 1973.

[31] Jogesh C. Pati and Abdus Salam. Unified Lepton-Hadron Symmetry and a Gauge Theory of the Basic Interactions. *Phys. Rev.*, D8:1240–1251, 1973.

[32] Jogesh C. Pati and Abdus Salam. Lepton Number as the Fourth Color. *Phys. Rev.*, D10:275–289, 1974. [Erratum: Phys. Rev.D11,703(1975)].

[33] H. Georgi and S. L. Glashow. Unity of All Elementary Particle Forces. *Phys. Rev. Lett.*, 32:438–441, 1974.

[34] Howard Georgi. The State of the Art—Gauge Theories. *AIP Conf. Proc.*, 23:575–582, 1975.

[35] Harald Fritzsch and Peter Minkowski. Unified Interactions of Leptons and Hadrons. *Annals Phys.*, 93:193–266, 1975.

[36] Nima Arkani-Hamed, Andrew G. Cohen, and Howard Georgi. Electroweak symmetry breaking from dimensional deconstruction. *Phys. Lett.*, B513:232–240, 2001.

[37] Lisa Randall and Raman Sundrum. A Large mass hierarchy from a small extra dimension. *Phys. Rev. Lett.*, 83:3370–3373, 1999.

[38] Pierre Fayet. Supersymmetry and Weak, Electromagnetic and Strong Interactions. *Phys. Lett.*, 64B:159, 1976.

[39] Pierre Fayet. Spontaneously Broken Supersymmetric Theories of Weak, Electromagnetic and Strong Interactions. *Phys. Lett.*, 69B:489, 1977.

[40] Glennys R. Farrar and Pierre Fayet. Phenomenology of the Production, Decay, and Detection of New Hadronic States Associated with Supersymmetry. *Phys. Lett.*, 76B:575–579, 1978.

[41] Pierre Fayet. Relations Between the Masses of the Superpartners of Leptons and Quarks, the Goldstino Couplings and the Neutral Currents. *Phys. Lett.*, 84B:416, 1979.

[42] Sacha Davidson, Enrico Nardi, and Yosef Nir. Leptogenesis. *Phys. Rept.*, 466:105–177, 2008.

[43] B. Pontecorvo. Neutrino Experiments and the Problem of Conservation of Leptonic Charge. *Sov. Phys. JETP*, 26:984–988, 1968. [Zh. Eksp. Teor. Fiz.53,1717(1967)].

[44] B. Pontecorvo. Mesonium and anti-mesonium. *Sov. Phys. JETP*, 6:429, 1957. [Zh. Eksp. Teor. Fiz.33,549(1957)].

[45] B. Pontecorvo. Inverse beta processes and nonconservation of lepton charge. *Sov. Phys. JETP*, 7:172–173, 1958. [Zh. Eksp. Teor. Fiz.34,247(1957)].

[46] Ziro Maki, Masami Nakagawa, and Shoichi Sakata. Remarks on the unified model of elementary particles. *Prog. Theor. Phys.*, 28:870–880, 1962.

[47] W. Rodejohann and J. W. F. Valle. Symmetrical Parametrizations of the Lepton Mixing Matrix. *Phys. Rev.*, D84:073011, 2011.

[48] B. T. Cleveland, Timothy Daily, Raymond Davis, Jr., James R. Distel, Kenneth Lande, C. K. Lee, Paul S. Wildenhain, and Jack Ullman. Measurement of the solar electron neutrino flux with the Homestake chlorine detector. *Astrophys. J.*, 496:505–526, 1998.

[49] Y. Fukuda et al. Solar neutrino data covering solar cycle 22. *Phys. Rev. Lett.*, 77:1683–1686, 1996.

[50] J. N. Abdurashitov et al. Measurement of the solar neutrino capture rate with gallium metal. III: Results for the 2002–2007 data-taking period. *Phys. Rev.*, C80:015807, 2009.

[51] P. Anselmann et al. Solar neutrinos observed by GALLEX at Gran Sasso. *Phys. Lett.*, B285:376–389, 1992.

[52] W. Hampel et al. GALLEX solar neutrino observations: Results for GALLEX IV. *Phys. Lett.*, B447:127–133, 1999.

[53] M. Altmann et al. Complete results for five years of GNO solar neutrino observations. *Phys. Lett.*, B616:174–190, 2005.

[54] S. Fukuda et al. Determination of solar neutrino oscillation parameters using 1496 days of Super-Kamiokande I data. *Phys. Lett.*, B539:179–187, 2002.

[55] Q. R. Ahmad et al. Measurement of the rate of $\nu_e + d \rightarrow p + p + e^-$ interactions produced by ^8B solar neutrinos at the Sudbury Neutrino Observatory. *Phys. Rev. Lett.*, 87:071301, 2001.

[56] Q. R. Ahmad et al. Direct evidence for neutrino flavor transformation from neutral current interactions in the Sudbury Neutrino Observatory. *Phys. Rev. Lett.*, 89:011301, 2002.

[57] K. Eguchi et al. First results from KamLAND: Evidence for reactor anti-neutrino disappearance. *Phys. Rev. Lett.*, 90:021802, 2003.

[58] T. Araki et al. Measurement of neutrino oscillation with KamLAND: Evidence of spectral distortion. *Phys. Rev. Lett.*, 94:081801, 2005.

[59] Y. Abe et al. Indication of Reactor $\bar{\nu}_e$ Disappearance in the Double Chooz Experiment. *Phys. Rev. Lett.*, 108:131801, 2012.

[60] F. P. An et al. Observation of electron-antineutrino disappearance at Daya Bay. *Phys. Rev. Lett.*, 108:171803, 2012.

[61] F. P. An et al. Improved Measurement of Electron Antineutrino Disappearance at Daya Bay. *Chin. Phys.*, C37:011001, 2013.

[62] F. P. An et al. Spectral measurement of electron antineutrino oscillation amplitude and frequency at Daya Bay. *Phys. Rev. Lett.*, 112:061801, 2014.

[63] J. K. Ahn et al. Observation of Reactor Electron Antineutrino Disappearance in the RENO Experiment. *Phys. Rev. Lett.*, 108:191802, 2012.

[64] Y. Fukuda et al. Evidence for oscillation of atmospheric neutrinos. *Phys. Rev. Lett.*, 81:1562–1567, 1998.

[65] Y. Ashie et al. Evidence for an oscillatory signature in atmospheric neutrino oscillation. *Phys. Rev. Lett.*, 93:101801, 2004.

[66] M. H. Ahn et al. Measurement of Neutrino Oscillation by the K2K Experiment. *Phys. Rev.*, D74:072003, 2006.

[67] D. G. Michael et al. Observation of muon neutrino disappearance with the MINOS detectors and the NuMI neutrino beam. *Phys. Rev. Lett.*, 97:191801, 2006.

[68] P. Adamson et al. Measurement of Neutrino Oscillations with the MINOS Detectors in the NuMI Beam. *Phys. Rev. Lett.*, 101:131802, 2008.

[69] P. Adamson et al. Measurement of the Neutrino Mass Splitting and Flavor Mixing by MINOS. *Phys. Rev. Lett.*, 106:181801, 2011.

[70] K. Abe et al. First Muon-Neutrino Disappearance Study with an Off-Axis Beam. *Phys. Rev.*, D85:031103, 2012.

[71] K. Abe et al. Measurement of Neutrino Oscillation Parameters from Muon Neutrino Disappearance with an Off-axis Beam. *Phys. Rev. Lett.*, 111(21):211803, 2013.

[72] K. Abe et al. Indication of Electron Neutrino Appearance from an Accelerator-produced Off-axis Muon Neutrino Beam. *Phys. Rev. Lett.*, 107:041801, 2011.

[73] K. Abe et al. Evidence of Electron Neutrino Appearance in a Muon Neutrino Beam. *Phys. Rev.*, D88(3):032002, 2013.

[74] P. Adamson et al. Improved search for muon-neutrino to electron-neutrino oscillations in MINOS. *Phys. Rev. Lett.*, 107:181802, 2011.

[75] Y. Abe et al. Reactor electron antineutrino disappearance in the Double Chooz experiment. *Phys. Rev.*, D86:052008, 2012.

[76] K. Abe et al. Measurement of neutrino and antineutrino oscillations by the T2K experiment including a new additional sample of ν_e interactions at the far detector. 2017.

[77] J. Schechter and J. W. F. Valle. Neutrinoless Double beta Decay in SU(2) x U(1) Theories. *Phys. Rev.*, D25:2951, 1982.

[78] V. N. Aseev et al. An upper limit on electron antineutrino mass from Troitsk experiment. *Phys. Rev.*, D84:112003, 2011.

[79] Ch. Kraus et al. Final results from phase II of the Mainz neutrino mass search in tritium beta decay. *Eur. Phys. J.*, C40:447–468, 2005.

[80] M. Agostini et al. Results on Neutrinoless Double-β Decay of ^{76}Ge from Phase I of the GERDA Experiment. *Phys. Rev. Lett.*, 111(12):122503, 2013.

[81] C. Alduino et al. Analysis techniques for the evaluation of the neutrinoless double-β decay lifetime in ^{130}Te with the CUORE-0 detector. *Phys. Rev.*, C93(4):045503, 2016.

[82] J. B. Albert et al. Search for Majorana neutrinos with the first two years of EXO-200 data. *Nature*, 510:229–234, 2014.

[83] A. Gando et al. Search for Majorana Neutrinos near the Inverted Mass Hierarchy Region with KamLAND-Zen. *Phys. Rev. Lett.*, 117(8):082503, 2016. [Addendum: Phys. Rev. Lett.117,no.10,109903(2016)].

[84] R. Arnold et al. Results of the search for neutrinoless double-β decay in ^{100}Mo with the NEMO-3 experiment. *Phys. Rev.*, D92(7):072011, 2015.

[85] P. A. R. Ade et al. Planck 2015 results. XIII. Cosmological parameters. *Astron. Astrophys.*, 594:A13, 2016.

[86] Francesco Capozzi, Eleonora Di Valentino, Eligio Lisi, Antonio Marrone, Alessandro Melchiorri, and Antonio Palazzo. Global constraints on absolute neutrino masses and their ordering. *Phys. Rev.*, D95(9):096014, 2017.

[87] P. F. de Salas, D. V. Forero, C. A. Ternes, M. Tortola, and J. W. F. Valle. Status of neutrino oscillations 2017. 2017.

[88] Ivan Esteban, M. C. Gonzalez-Garcia, Michele Maltoni, Ivan Martinez-Soler, and Thomas Schwetz. Updated fit to three neutrino mixing: exploring the accelerator-reactor complementarity. *JHEP*, 01:087, 2017.

[89] F. Zwicky. Die Rotverschiebung von extragalaktischen Nebeln. *Helv. Phys. Acta*, 6:110–127, 1933. [Gen. Rel. Grav.41,207(2009)].

[90] F. Zwicky. On the Masses of Nebulae and of Clusters of Nebulae. *Astrophys. J.*, 86:217–246, 1937.

[91] Vera C. Rubin and W. Kent Ford, Jr. Rotation of the Andromeda Nebula from a Spectroscopic Survey of Emission Regions. *Astrophys. J.*, 159:379–403, 1970.

[92] Gianfranco Bertone, Dan Hooper, and Joseph Silk. Particle dark matter: Evidence, candidates and constraints. *Phys. Rept.*, 405:279–390, 2005.

[93] Dan Hooper. Particle Dark Matter. In *Proceedings of Theoretical Advanced Study Institute in Elementary Particle Physics on The dawn of the LHC era (TASI 2008): Boulder, USA, June 2-27, 2008*, pages 709–764, 2010.

[94] Stefano Profumo. Astrophysical Probes of Dark Matter. In *Proceedings, Theoretical Advanced Study Institute in Elementary Particle Physics: Searching for New Physics at Small and Large Scales (TASI 2012): Boulder, Colorado, June 4-29, 2012*, pages 143–189, 2013.

[95] Henk Hoekstra, Howard Yee, and Mike Gladders. Current status of weak gravitational lensing. *New Astron. Rev.*, 46:767–781, 2002.

[96] R. Benton Metcalf, Leonidas A. Moustakas, Andrew J. Bunker, and Ian R. Parry. Spectroscopic gravitational lensing and limits on the dark matter substructure in Q2237+0305. *Astrophys. J.*, 607:43–59, 2004.

[97] Leonidas A. Moustakas and R. Benton Metcalf. Detecting dark matter substructure spectroscopically in strong gravitational lenses. *Mon. Not. Roy. Astron. Soc.*, 339:607, 2003.

[98] Douglas Clowe, Marusa Bradac, Anthony H. Gonzalez, Maxim Markevitch, Scott W. Randall, Christine Jones, and Dennis Zaritsky. A direct empirical proof of the existence of dark matter. *Astrophys. J.*, 648:L109–L113, 2006.

[99] M. Milgrom. A Modification of the Newtonian dynamics as a possible alternative to the hidden mass hypothesis. *Astrophys. J.*, 270:365–370, 1983.

[100] A. De Rujula, S. L. Glashow, and U. Sarid. CHARGED DARK MATTER. *Nucl. Phys.*, B333:173–194, 1990.

[101] Savas Dimopoulos, David Eichler, Rahim Esmailzadeh, and Glenn D. Starkman. Getting a Charge Out of Dark Matter. *Phys. Rev.*, D41:2388, 1990.

[102] Glenn D. Starkman, Andrew Gould, Rahim Esmailzadeh, and Savas Dimopoulos. Opening the Window on Strongly Interacting Dark Matter. *Phys. Rev.*, D41:3594, 1990.

[103] Sacha Davidson, Steen Hannestad, and Georg Raffelt. Updated bounds on millicharged particles. *JHEP*, 05:003, 2000.

[104] Chaïmae El Aisati, Thomas Hambye, and Tiziana Scarnà. Can a millicharged dark matter particle emit an observable gamma-ray line? *JHEP*, 08:133, 2014.

[105] Alejandro Ibarra and David Tran. Decaying Dark Matter and the PAMELA Anomaly. *JCAP*, 0902:021, 2009.

[106] Alejandro Ibarra, David Tran, and Christoph Weniger. Decaying Dark Matter in Light of the PAMELA and Fermi LAT Data. *JCAP*, 1001:009, 2010.

[107] Xiaoyuan Huang, Gilles Vertongen, and Christoph Weniger. Probing Dark Matter Decay and Annihilation with Fermi LAT Observations of Nearby Galaxy Clusters. *JCAP*, 1201:042, 2012.

[108] Arman Esmaili, Alejandro Ibarra, and Orlando L. G. Peres. Probing the stability of superheavy dark matter particles with high-energy neutrinos. *JCAP*, 1211:034, 2012.

[109] Max Tegmark et al. The 3-D power spectrum of galaxies from the SDSS. *Astrophys. J.*, 606:702–740, 2004.

[110] P. J. E. Peebles. Large scale background temperature and mass fluctuations due to scale invariant primeval perturbations. *Astrophys. J.*, 263:L1–L5, 1982.

[111] George R. Blumenthal, S. M. Faber, Joel R. Primack, and Martin J. Rees. Formation of Galaxies and Large Scale Structure with Cold Dark Matter. *Nature*, 311:517–525, 1984.

[112] Jesper Sommer-Larsen and Alexandre Dolgov. Formation of disk galaxies: warm dark matter and the angular momentum problem. *Astrophys. J.*, 551:608–623, 2001.

[113] Paul Bode, Jeremiah P. Ostriker, and Neil Turok. Halo formation in warm dark matter models. *Astrophys. J.*, 556:93–107, 2001.

[114] Keith A. Olive, Gary Steigman, and Terry P. Walker. Primordial nucleosynthesis: Theory and observations. *Phys. Rept.*, 333:389–407, 2000.

[115] David N. Spergel and Paul J. Steinhardt. Observational evidence for selfinteracting cold dark matter. *Phys. Rev. Lett.*, 84:3760–3763, 2000.

[116] Oleg Y. Gnedin and Jeremiah P. Ostriker. Destruction of the galactic globular cluster system. *Astrophys. J.*, 474:223, 1997.

[117] Lawrence J. Hall, Karsten Jedamzik, John March-Russell, and Stephen M. West. Freeze-In Production of FIMP Dark Matter. *JHEP*, 03:080, 2010.

[118] Alexander Merle, Aurel Schneider, and Maximilian Totzauer. Dodelson-Widrow Production of Sterile Neutrino Dark Matter with Non-Trivial Initial Abundance. *JCAP*, 1604(04):003, 2016.

[119] Michael S. Turner. Coherent Scalar Field Oscillations in an Expanding Universe. *Phys. Rev.*, D28:1243, 1983.

[120] Benjamin W. Lee and Steven Weinberg. Cosmological Lower Bound on Heavy Neutrino Masses. *Phys. Rev. Lett.*, 39:165–168, 1977.

[121] Jeremy Bernstein, Lowell S. Brown, and Gerald Feinberg. The Cosmological Heavy Neutrino Problem Revisited. *Phys. Rev.*, D32:3261, 1985.

[122] Paolo Gondolo and Graciela Gelmini. Cosmic abundances of stable particles: Improved analysis. *Nucl. Phys.*, B360:145–179, 1991.

[123] R. D. Peccei and Helen R. Quinn. CP Conservation in the Presence of Instantons. *Phys. Rev. Lett.*, 38:1440–1443, 1977.

[124] R. D. Peccei and Helen R. Quinn. Constraints Imposed by CP Conservation in the Presence of Instantons. *Phys. Rev.*, D16:1791–1797, 1977.

[125] Steven Weinberg. A New Light Boson? *Phys. Rev. Lett.*, 40:223–226, 1978.

[126] Frank Wilczek. Problem of Strong p and t Invariance in the Presence of Instantons. *Phys. Rev. Lett.*, 40:279–282, 1978.

[127] Hai-Yang Cheng. The Strong CP Problem Revisited. *Phys. Rept.*, 158:1, 1988.

[128] Jihn E. Kim. Light Pseudoscalars, Particle Physics and Cosmology. *Phys. Rept.*, 150:1–177, 1987.

[129] Michael S. Turner. Windows on the Axion. *Phys. Rept.*, 197:67–97, 1990.

[130] M. Drewes et al. A White Paper on keV Sterile Neutrino Dark Matter. *JCAP*, 1701(01):025, 2017.

[131] Peter Minkowski. $\mu \to e\gamma$ at a Rate of One Out of 10^9 Muon Decays? *Phys. Lett.*, 67B:421–428, 1977.

[132] Tsutomu Yanagida. HORIZONTAL SYMMETRY AND MASSES OF NEUTRINOS. *Conf. Proc.*, C7902131:95–99, 1979.

[133] Murray Gell-Mann, Pierre Ramond, and Richard Slansky. Complex Spinors and Unified Theories. *Conf. Proc.*, C790927:315–321, 1979.

[134] J. Schechter and J. W. F. Valle. Neutrino Masses in SU(2) x U(1) Theories. *Phys. Rev.*, D22:2227, 1980.

[135] Rabindra N. Mohapatra and Goran Senjanovic. Neutrino Mass and Spontaneous Parity Violation. *Phys. Rev. Lett.*, 44:912, 1980.

[136] J. Schechter and J. W. F. Valle. Neutrino Decay and Spontaneous Violation of Lepton Number. *Phys. Rev.*, D25:774, 1982.

[137] Scott Dodelson and Lawrence M. Widrow. Sterile-neutrinos as dark matter. *Phys. Rev. Lett.*, 72:17–20, 1994.

[138] Esra Bulbul, Maxim Markevitch, Adam Foster, Randall K. Smith, Michael Loewen-stein, and Scott W. Randall. Detection of An Unidentified Emission Line in the Stacked X-ray spectrum of Galaxy Clusters. *Astrophys. J.*, 789:13, 2014.

[139] Alexey Boyarsky, Oleg Ruchayskiy, Dmytro Iakubovskyi, and Jeroen Franse. Unidentified Line in X-Ray Spectra of the Andromeda Galaxy and Perseus Galaxy Cluster. *Phys. Rev. Lett.*, 113:251301, 2014.

[140] Takehiko Asaka, Steve Blanchet, and Mikhail Shaposhnikov. The nuMSM, dark matter and neutrino masses. *Phys. Lett.*, B631:151–156, 2005.

[141] Riccardo Catena and Piero Ullio. A novel determination of the local dark matter density. *JCAP*, 1008:004, 2010.

[142] Mark W. Goodman and Edward Witten. Detectability of Certain Dark Matter Candidates. *Phys. Rev.*, D31:3059, 1985.

[143] R. J. Gaitskell. Direct detection of dark matter. *Ann. Rev. Nucl. Part. Sci.*, 54:315–359, 2004.

[144] Richard W. Schnee. Introduction to dark matter experiments. In *Physics of the large and the small, TASI 09, proceedings of the Theoretical Advanced Study Institute in Elementary Particle Physics, Boulder, Colorado, USA, 1-26 June 2009*, pages 775–829, 2011.

[145] P. Cushman et al. Working Group Report: WIMP Dark Matter Direct Detection. In *Proceedings, 2013 Community Summer Study on the Future of U.S. Particle Physics: Snowmass on the Mississippi (CSS2013): Minneapolis, MN, USA, July 29-August 6, 2013*, 2013.

[146] R. Bernabei et al. New results from DAMA/LIBRA. *Eur. Phys. J.*, C67:39–49, 2010.

[147] Christopher Savage, Graciela Gelmini, Paolo Gondolo, and Katherine Freese. XENON10/100 dark matter constraints in comparison with CoGeNT and DAMA: examining the Leff dependence. *Phys. Rev.*, D83:055002, 2011.

[148] Joachim Kopp, Thomas Schwetz, and Jure Zupan. Global interpretation of direct Dark Matter searches after CDMS-II results. *JCAP*, 1002:014, 2010.

[149] Sarah Andreas, Chiara Arina, Thomas Hambye, Fu-Sin Ling, and Michel H. G. Tytgat. A light scalar WIMP through the Higgs portal and CoGeNT. *Phys. Rev.*, D82:043522, 2010.

[150] Nassim Bozorgnia, Graciela B. Gelmini, and Paolo Gondolo. Channeling in solid Xe, Ar and Ne direct dark matter detectors. *Nucl. Instrum. Meth.*, A654:162–169, 2011.

[151] Marco Cirelli. Status of Indirect (and Direct) Dark Matter searches. 2015.

[152] Oscar Adriani et al. An anomalous positron abundance in cosmic rays with energies 1.5-100 GeV. *Nature*, 458:607–609, 2009.

[153] M. Ackermann et al. Measurement of separate cosmic-ray electron and positron spectra with the Fermi Large Area Telescope. *Phys. Rev. Lett.*, 108:011103, 2012.

[154] L. Accardo et al. High Statistics Measurement of the Positron Fraction in Primary Cosmic Rays of 0.5–500 GeV with the Alpha Magnetic Spectrometer on the International Space Station. *Phys. Rev. Lett.*, 113:121101, 2014.

[155] O. Adriani et al. Measurement of the flux of primary cosmic ray antiprotons with energies of 60-MeV to 350-GeV in the PAMELA experiment. *JETP Lett.*, 96:621–627, 2013. [Pisma Zh. Eksp. Teor. Fiz.96,693(2012)].

[156] Samuel Ting. Latest results from the Alpha Magnetic Spectrometer on the International Space Station. *PoS*, ICRC2015:036, 2016.

[157] Gaëlle Giesen, Mathieu Boudaud, Yoann Génolini, Vivian Poulin, Marco Cirelli, Pierre Salati, and Pasquale D. Serpico. AMS-02 antiprotons, at last! Secondary astrophysical component and immediate implications for Dark Matter. *JCAP*, 1509(09):023, 2015.

[158] Abdelhak Djouadi, Oleg Lebedev, Yann Mambrini, and Jeremie Quevillon. Implications of LHC searches for Higgs–portal dark matter. *Phys. Lett.*, B709:65–69, 2012.

[159] G. Belanger, B. Dumont, U. Ellwanger, J. F. Gunion, and S. Kraml. Status of invisible Higgs decays. *Phys. Lett.*, B723:340–347, 2013.

[160] Chaïmae El Aisati, Michael Gustafsson, and Thomas Hambye. New Search for Monochromatic Neutrinos from Dark Matter Decay. *Phys. Rev.*, D92(12):123515, 2015.

[161] Marco Cirelli, Gennaro Corcella, Andi Hektor, Gert Hutsi, Mario Kadastik, Paolo Panci, Martti Raidal, Filippo Sala, and Alessandro Strumia. PPPC 4 DM ID: A Poor Particle Physicist Cookbook for Dark Matter Indirect Detection. *JCAP*, 1103:051, 2011. [Erratum: JCAP1210,E01(2012)].

[162] Paolo Ciafaloni, Denis Comelli, Antonio Riotto, Filippo Sala, Alessandro Strumia, and Alfredo Urbano. Weak Corrections are Relevant for Dark Matter Indirect Detection. *JCAP*, 1103:019, 2011.

[163] Julio F. Navarro, Carlos S. Frenk, and Simon D. M. White. The Structure of cold dark matter halos. *Astrophys. J.*, 462:563–575, 1996.

[164] Alister W. Graham, David Merritt, Ben Moore, Juerg Diemand, and Balsa Terzic. Empirical models for Dark Matter Halos. I. Nonparametric Construction of Density Profiles and Comparison with Parametric Models. *Astron. J.*, 132:2685–2700, 2006.

[165] Julio F. Navarro, Aaron Ludlow, Volker Springel, Jie Wang, Mark Vogelsberger, Simon D. M. White, Adrian Jenkins, Carlos S. Frenk, and Amina Helmi. The Diversity and Similarity of Cold Dark Matter Halos. *Mon. Not. Roy. Astron. Soc.*, 402:21, 2010.

[166] K. G. Begeman, A. H. Broeils, and R. H. Sanders. Extended rotation curves of spiral galaxies: Dark haloes and modified dynamics. *Mon. Not. Roy. Astron. Soc.*, 249:523, 1991.

[167] John N. Bahcall and R. M. Soneira. The Universe at faint magnetidues. 2. Models for the predicted star counts. *Astrophys. J. Suppl.*, 44:73–110, 1980.

[168] A. Burkert. The Structure of dark matter halos in dwarf galaxies. *IAU Symp.*, 171:175, 1996. [Astrophys. J.447,L25(1995)].

[169] Jurg Diemand, Ben Moore, and Joachim Stadel. Convergence and scatter of cluster density profiles. *Mon. Not. Roy. Astron. Soc.*, 353:624, 2004.

[170] Dan Hooper and Pasquale D. Serpico. Angular Signatures of Dark Matter in the Diffuse Gamma Ray Spectrum. *JCAP*, 0706:013, 2007.

[171] James E. Taylor and Joseph Silk. The Clumpiness of cold dark matter: Implications for the annihilation signal. *Mon. Not. Roy. Astron. Soc.*, 339:505, 2003.

[172] Angelo F. Neto, Liang Gao, Philip Bett, Shaun Cole, Julio F. Navarro, Carlos S. Frenk, Simon D. M. White, Volker Springel, and Adrian Jenkins. The statistics of lambda CDM Halo Concentrations. *Mon. Not. Roy. Astron. Soc.*, 381:1450–1462, 2007.

[173] Andrea V. Maccio', Aaron A. Dutton, and Frank C. van den Bosch. Concentration, Spin and Shape of Dark Matter Haloes as a Function of the Cosmological Model: WMAP1, WMAP3 and WMAP5 results. *Mon. Not. Roy. Astron. Soc.*, 391:1940–1954, 2008.

[174] Gregory D. Martinez, James S. Bullock, Manoj Kaplinghat, Louis E. Strigari, and Roberto Trotta. Indirect Dark Matter Detection from Dwarf Satellites: Joint Expectations from Astrophysics and Supersymmetry. *JCAP*, 0906:014, 2009.

[175] Torsten Bringmann. Particle Models and the Small-Scale Structure of Dark Matter. *New J. Phys.*, 11:105027, 2009.

[176] Jatan Buch, Marco Cirelli, Gaëlle Giesen, and Marco Taoso. PPPC 4 DM secondary: A Poor Particle Physicist Cookbook for secondary radiation from Dark Matter. *JCAP*, 1509(09):037, 2015.

[177] Francis Halzen and Dan Hooper. High-energy neutrino astronomy: The Cosmic ray connection. *Rept. Prog. Phys.*, 65:1025–1078, 2002.

[178] Morihiro Honda, T. Kajita, K. Kasahara, S. Midorikawa, and T. Sanuki. Calculation of atmospheric neutrino flux using the interaction model calibrated with atmospheric muon data. *Phys. Rev.*, D75:043006, 2007.

[179] Rikard Enberg, Mary Hall Reno, and Ina Sarcevic. Prompt neutrino fluxes from atmospheric charm. *Phys. Rev.*, D78:043005, 2008.

[180] M. Honda, T. Kajita, K. Kasahara, and S. Midorikawa. Calculation of the flux of atmospheric neutrinos. *Phys. Rev.*, D52:4985–5005, 1995.

[181] G. D. Barr, T. K. Gaisser, P. Lipari, Simon Robbins, and T. Stanev. A Three - dimensional calculation of atmospheric neutrinos. *Phys. Rev.*, D70:023006, 2004.

[182] Morihiro Honda, T. Kajita, K. Kasahara, and S. Midorikawa. A New calculation of the atmospheric neutrino flux in a 3-dimensional scheme. *Phys. Rev.*, D70:043008, 2004.

[183] Thomas K. Gaisser, Ralph Engel, and Elisa Resconi. *Cosmic Rays and Particle Physics*. Cambridge University Press.

[184] Stefan Schonert, Thomas K. Gaisser, Elisa Resconi, and Olaf Schulz. Vetoing atmospheric neutrinos in a high energy neutrino telescope. *Phys. Rev.*, D79:043009, 2009.

[185] Thomas K. Gaisser, Kyle Jero, Albrecht Karle, and Jakob van Santen. Generalized self-veto probability for atmospheric neutrinos. *Phys. Rev.*, D90(2):023009, 2014.

[186] M. G. Aartsen et al. Atmospheric and astrophysical neutrinos above 1 TeV interacting in IceCube. *Phys. Rev.*, D91(2):022001, 2015.

[187] Aaron C. Vincent, Carlos A. Argüelles, and Ali Kheirandish. High-energy neutrino attenuation in the Earth and its associated uncertainties. 2017.

[188] Anatoli Fedynitch, Julia Becker Tjus, and Paolo Desiati. Influence of hadronic interaction models and the cosmic ray spectrum on the high energy atmospheric muon and neutrino flux. *Phys. Rev.*, D86:114024, 2012.

[189] C. G. S. Costa. The Prompt lepton cookbook. *Astropart. Phys.*, 16:193–204, 2001.

[190] Giovanni Fiorentini, Vadim A. Naumov, and Francesco L. Villante. Atmospheric neutrino flux supported by recent muon experiments. *Phys. Lett.*, B510:173–188, 2001.

[191] R. Abbasi et al. The Energy Spectrum of Atmospheric Neutrinos between 2 and 200 TeV with the AMANDA-II Detector. *Astropart. Phys.*, 34:48–58, 2010.

[192] R. Abbasi et al. Measurement of the atmospheric neutrino energy spectrum from 100 GeV to 400 TeV with IceCube. *Phys. Rev.*, D83:012001, 2011.

[193] R. Abbasi et al. A Search for a Diffuse Flux of Astrophysical Muon Neutrinos with the IceCube 40-String Detector. *Phys. Rev.*, D84:082001, 2011.

[194] M. G. Aartsen et al. Search for a diffuse flux of astrophysical muon neutrinos with the IceCube 59-string configuration. *Phys. Rev.*, D89(6):062007, 2014.

[195] M. G. Aartsen et al. Observation and Characterization of a Cosmic Muon Neutrino Flux from the Northern Hemisphere using six years of IceCube data. *Astrophys. J.*, 833(1):3, 2016.

[196] Atri Bhattacharya, Rikard Enberg, Mary Hall Reno, Ina Sarcevic, and Anna Stasto. Perturbative charm production and the prompt atmospheric neutrino flux in light of RHIC and LHC. *JHEP*, 06:110, 2015.

[197] Rhorry Gauld, Juan Rojo, Luca Rottoli, Subir Sarkar, and Jim Talbert. The prompt atmospheric neutrino flux in the light of LHCb. *JHEP*, 02:130, 2016.

[198] Atri Bhattacharya, Rikard Enberg, Yu Seon Jeong, C. S. Kim, Mary Hall Reno, Ina Sarcevic, and Anna Stasto. Prompt atmospheric neutrino fluxes: perturbative QCD models and nuclear effects. *JHEP*, 11:167, 2016.

[199] Enrico Fermi. On the Origin of the Cosmic Radiation. *Phys. Rev.*, 75:1169–1174, 1949.

[200] E. Fermi. Galactic Magnetic Fields and the Origin of Cosmic Radiation. *Astrophys. J.*, 119:1–6, 1954.

[201] L. Oc. Drury. An introduction to the theory of diffusive shock acceleration of energetic particles in tenuous plasmas. *Rept. Prog. Phys.*, 46:973–1027, 1983.

[202] R. Blandford and D. Eichler. Particle Acceleration at Astrophysical Shocks: A Theory of Cosmic Ray Origin. *Phys. Rept.*, 154:1–75, 1987.

[203] MA Malkov and L O'C Drury. Nonlinear theory of diffusive acceleration of particles by shock waves. *Rept. Prog. Phys.*, 64(4):429–481, 2001.

[204] Abraham Loeb and Eli Waxman. The Cumulative background of high energy neutrinos from starburst galaxies. *JCAP*, 0605:003, 2006.

[205] S. R. Kelner, Felex A. Aharonian, and V. V. Bugayov. Energy spectra of gamma-rays, electrons and neutrinos produced at proton-proton interactions in the very high energy regime. *Phys. Rev.*, D74:034018, 2006. [Erratum: Phys. Rev.D79,039901(2009)].

[206] A. Mucke, Ralph Engel, J. P. Rachen, R. J. Protheroe, and Todor Stanev. SOPHIA: Monte Carlo simulations of photohadronic processes in astrophysics. *Comput. Phys. Commun.*, 124:290–314, 2000.

[207] Pasquale Blasi and Elena Amato. Diffusive propagation of cosmic rays from supernova remnants in the Galaxy. I: spectrum and chemical composition. *JCAP*, 1201:010, 2012.

[208] Pasquale Blasi and Elena Amato. Diffusive propagation of cosmic rays from supernova remnants in the Galaxy. II: anisotropy. *JCAP*, 1201:011, 2012.

[209] Kohta Murase. On the Origin of High-Energy Cosmic Neutrinos. *AIP Conf. Proc.*, 1666:040006, 2015.

[210] Y. Uchiyama, F. A. Aharonian, T. Tanaka, T. Takahashi, and Y. Maeda. Extremely fast acceleration of cosmic rays in a supernova remnant. *Nature*, 449:576–578, 2007.

[211] Sovan Chakraborty and Ignacio Izaguirre. Diffuse neutrinos from extragalactic supernova remnants: Dominating the 100 TeV IceCube flux. *Phys. Lett.*, B745:35–39, 2015.

[212] Sovan Chakraborty and Ignacio Izaguirre. Star-forming galaxies as the origin of IceCube neutrinos: Reconciliation with Fermi-LAT gamma rays. 2016.

[213] Kohta Murase, Markus Ahlers, and Brian C. Lacki. Testing the Hadronuclear Origin of PeV Neutrinos Observed with IceCube. *Phys. Rev.*, D88(12):121301, 2013.

[214] Keith Bechtol, Markus Ahlers, Mattia Di Mauro, Marco Ajello, and Justin Vandenbroucke. Evidence against star-forming galaxies as the dominant source of IceCube neutrinos. *Astrophys. J.*, 836(1):47, 2017.

[215] Kohta Murase and Eli Waxman. Constraining High-Energy Cosmic Neutrino Sources: Implications and Prospects. *Phys. Rev.*, D94(10):103006, 2016.

[216] M. Ackermann et al. The spectrum of isotropic diffuse gamma-ray emission between 100 MeV and 820 GeV. *Astrophys. J.*, 799:86, 2015.

[217] F. W. Stecker, C. Done, M. H. Salamon, and P. Sommers. High-energy neutrinos from active galactic nuclei. *Phys. Rev. Lett.*, 66:2697–2700, 1991. [Erratum: Phys. Rev. Lett.69,2738(1992)].

[218] Oleg E. Kalashev, Alexander Kusenko, and Warren Essey. PeV neutrinos from intergalactic interactions of cosmic rays emitted by active galactic nuclei. *Phys. Rev. Lett.*, 111(4):041103, 2013.

[219] O. Kalashev, D. Semikoz, and I. Tkachev. Neutrinos in IceCube from active galactic nuclei. *J. Exp. Theor. Phys.*, 120(3):541–548, 2015.

[220] Walter Winter. Photohadronic Origin of the TeV-PeV Neutrinos Observed in IceCube. *Phys. Rev.*, D88:083007, 2013.

[221] Thorsten Glüsenkamp. Analysis of the cumulative neutrino flux from Fermi-LAT blazar populations using 3 years of IceCube data. *EPJ Web Conf.*, 121:05006, 2016.

[222] Michael Schimp, Martin Leuermann, and Christopher Wiebusch. Astrophysical interpretation of small-scale neutrino angular correlation searches with IceCube. *PoS*, ICRC2015:1085, 2016.

[223] M. G. Aartsen et al. The contribution of Fermi-2LAC blazars to the diffuse TeV-PeV neutrino flux. *Astrophys. J.*, 835(1):45, 2017.

[224] Eli Waxman and John N. Bahcall. High-energy neutrinos from cosmological gamma-ray burst fireballs. *Phys. Rev. Lett.*, 78:2292–2295, 1997.

[225] Mario Vietri. Ultrahigh-energy neutrinos from gamma-ray bursts. *Phys. Rev. Lett.*, 80:3690–3693, 1998.

[226] Markus Bottcher and Charles D. Dermer. High-energy gamma-rays from ultrahigh-energy cosmic ray protons in gamma-ray bursts. *Astrophys. J.*, 499:L131–L134, 1998.

[227] R. Abbasi et al. An absence of neutrinos associated with cosmic-ray acceleration in γ-ray bursts. *Nature*, 484:351–353, 2012.

[228] M. G. Aartsen et al. Search for Prompt Neutrino Emission from Gamma-Ray Bursts with IceCube. *Astrophys. J.*, 805(1):L5, 2015.

[229] M. G. Aartsen et al. Extending the search for muon neutrinos coincident with gamma-ray bursts in IceCube data. *Astrophys. J.*, 843(2):112, 2017.

[230] Eli Waxman and John N. Bahcall. High-energy neutrinos from astrophysical sources: An Upper bound. *Phys. Rev.*, D59:023002, 1999.

[231] Shigeo S. Kimura, Kohta Murase, and Kenji Toma. Neutrino and Cosmic-Ray Emission and Cumulative Background from Radiatively Inefficient Accretion Flows in Low-Luminosity Active Galactic Nuclei. *Astrophys. J.*, 806:159, 2015.

[232] Kohta Murase, Dafne Guetta, and Markus Ahlers. Hidden Cosmic-Ray Accelerators as an Origin of TeV-PeV Cosmic Neutrinos. *Phys. Rev. Lett.*, 116(7):071101, 2016.

[233] Nicholas Senno, Kohta Murase, and Peter Meszaros. Choked Jets and Low-Luminosity Gamma-Ray Bursts as Hidden Neutrino Sources. *Phys. Rev.*, D93(8):083003, 2016.

[234] Claudio Kopper, William Giang, and Naoko Kurahashi. Observation of Astrophysical Neutrinos in Four Years of IceCube Data. *PoS*, ICRC2015:1081, 2016.

[235] C. Kopper. . *PoS ICRC*, (981), 2017.

[236] M. G. Aartsen et al. Evidence for Astrophysical Muon Neutrinos from the Northern Sky with IceCube. *Phys. Rev. Lett.*, 115(8):081102, 2015.

[237] Lars Mohrmann. Combined Analysis of the High-Energy Cosmic Neutrino Flux at the IceCube Detector. *PoS*, ICRC2015:1066, 2016.

[238] M. G. Aartsen et al. Observation of High-Energy Astrophysical Neutrinos in Three Years of IceCube Data. *Phys. Rev. Lett.*, 113:101101, 2014.

[239] M. G. Aartsen et al. Searches for Extended and Point-like Neutrino Sources with Four Years of IceCube Data. *Astrophys. J.*, 796(2):109, 2014.

[240] M. G. Aartsen et al. All-sky Search for Time-integrated Neutrino Emission from Astrophysical Sources with 7 yr of IceCube Data. *Astrophys. J.*, 835(2):151, 2017.

[241] M. G. Aartsen et al. Constraints on Galactic Neutrino Emission with Seven Years of IceCube Data. 2017.

[242] A. Palladino, G. Pagliaroli, F. L. Villante, and F. Vissani. What is the Flavor of the Cosmic Neutrinos Seen by IceCube? *Phys. Rev. Lett.*, 114(17):171101, 2015.

[243] Carlos A. Argüelles, Teppei Katori, and Jordi Salvado. New Physics in Astrophysical Neutrino Flavor. *Phys. Rev. Lett.*, 115:161303, 2015.

[244] Mauricio Bustamante, John F. Beacom, and Walter Winter. Theoretically palatable flavor combinations of astrophysical neutrinos. *Phys. Rev. Lett.*, 115(16):161302, 2015.

[245] M. Ageron et al. ANTARES: the first undersea neutrino telescope. *Nucl. Instrum. Meth.*, A656:11–38, 2011.

[246] T. Eberl. . *PoS ICRC*, (993), 2017.

[247] J. A. Aguilar et al. Search for a diffuse flux of high-energy ν_μ with the ANTARES neutrino telescope. *Phys. Lett.*, B696:16–22, 2011.

[248] Jutta Schnabel and Steffen Hallmann. Search for a diffuse cosmic neutrino flux with ANTARES using track and cascade events. *PoS*, ICRC2015:1065, 2016.

[249] Jutta Schnabel. Muon energy reconstruction in the ANTARES detector. *Nucl. Instrum. Meth.*, A725:106–109, 2013.

[250] Tino Michael. Neutrino point source search including cascade events with the ANTARES neutrino telescope. *PoS*, ICRC2015:1078, 2016.

[251] S. Adrian-Martinez et al. Searches for Point-like and extended neutrino sources close to the Galactic Centre using the ANTARES neutrino Telescope. *Astrophys. J.*, 786:L5, 2014.

[252] A. Albert et al. First all-flavour Neutrino Point-like Source Search with the ANTARES Neutrino Telescope. *Submitted to: Phys. Rev. D*, 2017.

[253] S. Adrian-Martinez et al. Letter of intent for KM3NeT 2.0. *J. Phys.*, G43(8):084001, 2016.

[254] Steve Baker and Robert D. Cousins. Clarification of the Use of Chi Square and Likelihood Functions in Fits to Histograms. *Nucl. Instrum. Meth.*, 221:437–442, 1984.

[255] M. G. Aartsen et al. Evidence for High-Energy Extraterrestrial Neutrinos at the IceCube Detector. *Science*, 342:1242856, 2013.

[256] M. G. Aartsen et al. Energy Reconstruction Methods in the IceCube Neutrino Telescope. *JINST*, 9:P03009, 2014.

[257] M. G. Aartsen et al. A combined maximum-likelihood analysis of the high-energy astrophysical neutrino flux measured with IceCube. *Astrophys. J.*, 809(1):98, 2015.

[258] Chien-Yi Chen, P. S. Bhupal Dev, and Amarjit Soni. Two-component flux explanation for the high energy neutrino events at IceCube. *Phys. Rev.*, D92(7):073001, 2015.

[259] Andrea Palladino and Francesco Vissani. Extragalactic plus Galactic model for Ice-Cube neutrino events. *Astrophys. J.*, 826(2):185, 2016.

[260] Aaron C. Vincent, Sergio Palomares-Ruiz, and Olga Mena. Analysis of the 4-year IceCube high-energy starting events. *Phys. Rev.*, D94(2):023009, 2016.

[261] Andrea Palladino, Maurizio Spurio, and Francesco Vissani. On the IceCube spectral anomaly. *JCAP*, 1612(12):045, 2016.

[262] Luis A. Anchordoqui, Martin M. Block, Loyal Durand, Phuoc Ha, Jorge F. Soriano, and Thomas J. Weiler. Evidence for a break in the spectrum of astrophysical neutrinos. *Phys. Rev.*, D95(8):083009, 2017.

[263] Arman Esmaili, Sin Kyu Kang, and Pasquale Dario Serpico. IceCube events and decaying dark matter: hints and constraints. *JCAP*, 1412(12):054, 2014.

[264] Sergey Troitsky. Search for Galactic disk and halo components in the arrival directions of high-energy astrophysical neutrinos. *JETP Lett.*, 102(12):785–788, 2015. [Pisma Zh. Eksp. Teor. Fiz.102,no.12,899(2015)].

[265] Andrii Neronov and Dmitry Semikoz. Neutrinos from Extra-Large Hadron Collider in the Milky Way. *Astropart. Phys.*, 72:32–37, 2016.

[266] M. Ackermann et al. Fermi-LAT Observations of the Diffuse Gamma-Ray Emission: Implications for Cosmic Rays and the Interstellar Medium. *Astrophys. J.*, 750:3, 2012.

[267] Emiliano Sefusatti, Gabrijela Zaharijas, Pasquale D. Serpico, David Theurel, and Michael Gustafsson. Extragalactic gamma-ray signal from dark matter annihilation: an appraisal. *Mon. Not. Roy. Astron. Soc.*, 441(3):1861–1878, 2014.

[268] F. J. Massey. . *Journal of the American Statistical Association*, 46:253, 1951.

[269] T. W. Anderson and D. A. Darling. . *Annals of Mathematical Statistics*, 23:193–212, 1952.

[270] R. Abbasi et al. Search for dark matter from the Galactic halo with the IceCube Neutrino Telescope. *Phys. Rev.*, D84:022004, 2011.

[271] S. Adrian-Martinez et al. Search of Dark Matter Annihilation in the Galactic Centre using the ANTARES Neutrino Telescope. *JCAP*, 1510(10):068, 2015.

[272] M. G. Aartsen et al. All-flavour Search for Neutrinos from Dark Matter Annihilations in the Milky Way with IceCube/DeepCore. *Eur. Phys. J.*, C76(10):531, 2016.

[273] A. Albert et al. Results from the search for dark matter in the Milky Way with 9 years of data of the ANTARES neutrino telescope. *Phys. Lett.*, B769:249–254, 2017.

[274] S. S. Wilks. The Large-Sample Distribution of the Likelihood Ratio for Testing Composite Hypotheses. *Annals Math. Statist.*, 9(1):60–62, 1938.

[275] H. Chernoff. . *Annals Math. Statist.*, 25:573, 1938.

[276] M. Ackermann et al. Search for Gamma-ray Spectral Lines with the Fermi Large Area Telescope and Dark Matter Implications. *Phys. Rev.*, D88:082002, 2013.

[277] Kohta Murase and John F. Beacom. Constraining Very Heavy Dark Matter Using Diffuse Backgrounds of Neutrinos and Cascaded Gamma Rays. *JCAP*, 1210:043, 2012.

[278] Arman Esmaili and Pasquale Dario Serpico. Gamma-ray bounds from EAS detectors and heavy decaying dark matter constraints. *JCAP*, 1510(10):014, 2015.

[279] Timothy Cohen, Kohta Murase, Nicholas L. Rodd, Benjamin R. Safdi, and Yotam Soreq. γ-ray Constraints on Decaying Dark Matter and Implications for IceCube. *Phys. Rev. Lett.*, 119(2):021102, 2017.

[280] Kim Griest and Marc Kamionkowski. Unitarity Limits on the Mass and Radius of Dark Matter Particles. *Phys. Rev. Lett.*, 64:615, 1990.

[281] Lam Hui. Unitarity bounds and the cuspy halo problem. *Phys. Rev. Lett.*, 86:3467–3470, 2001.

[282] Alexander Kusenko and Paul J. Steinhardt. Q ball candidates for selfinteracting dark matter. *Phys. Rev. Lett.*, 87:141301, 2001.

[283] Benjamin Audren, Julien Lesgourgues, Gianpiero Mangano, Pasquale Dario Serpico, and Thomas Tram. Strongest model-independent bound on the lifetime of Dark Matter. *JCAP*, 1412(12):028, 2014.

[284] Kevork Abazajian, George M. Fuller, and Wallace H. Tucker. Direct detection of warm dark matter in the X-ray. *Astrophys. J.*, 562:593–604, 2001.

[285] Douglas P. Finkbeiner and Neal Weiner. X-ray line from exciting dark matter. *Phys. Rev.*, D94(8):083002, 2016.

[286] Mads T. Frandsen, Francesco Sannino, Ian M. Shoemaker, and Ole Svendsen. X-ray Lines from Dark Matter: The Good, The Bad, and The Unlikely. *JCAP*, 1405:033, 2014.

[287] Henry Lew and Antonio Riotto. Baryogenesis, domain walls and the role of gravity. *Phys. Lett.*, B309:258–263, 1993.

[288] Balram Rai and Goran Senjanovic. Gravity and domain wall problem. *Phys. Rev.*, D49:2729–2733, 1994.

[289] Alexey Anisimov and Pasquale Di Bari. Cold Dark Matter from heavy Right-Handed neutrino mixing. *Phys. Rev.*, D80:073017, 2009.

[290] Tetsutaro Higaki, Ryuichiro Kitano, and Ryosuke Sato. Neutrinoful Universe. *JHEP*, 07:044, 2014.

[291] Pasquale Di Bari, Patrick Otto Ludl, and Sergio Palomares-Ruiz. Unifying leptoge-nesis, dark matter and high-energy neutrinos with right-handed neutrino mixing via Higgs portal. *JCAP*, 1611(11):044, 2016.

[292] Naoyuki Haba, Yuji Kajiyama, Shigeki Matsumoto, Hiroshi Okada, and Koichi Yoshi-oka. Universally Leptophilic Dark Matter From Non-Abelian Discrete Symmetry. *Phys. Lett.*, B695:476–481, 2011.

[293] Paul H. Frampton, Sheldon L. Glashow, and Danny Marfatia. Zeroes of the neutrino mass matrix. *Phys. Lett.*, B536:79–82, 2002.

[294] Harald Fritzsch, Zhi-zhong Xing, and Shun Zhou. Two-zero Textures of the Majorana Neutrino Mass Matrix and Current Experimental Tests. *JHEP*, 09:083, 2011.

[295] P. O. Ludl, S. Morisi, and E. Peinado. The Reactor mixing angle and CP violation with two texture zeros in the light of T2K. *Nucl. Phys.*, B857:411–423, 2012.

[296] Guido Altarelli and Ferruccio Feruglio. Discrete Flavor Symmetries and Models of Neutrino Mixing. *Rev. Mod. Phys.*, 82:2701–2729, 2010.

[297] Hajime Ishimori, Tatsuo Kobayashi, Hiroshi Ohki, Yusuke Shimizu, Hiroshi Okada, and Morimitsu Tanimoto. Non-Abelian Discrete Symmetries in Particle Physics. *Prog. Theor. Phys. Suppl.*, 183:1–163, 2010.

[298] Stephen F. King and Christoph Luhn. Neutrino Mass and Mixing with Discrete Symmetry. *Rept. Prog. Phys.*, 76:056201, 2013.

[299] Stephen F. King, Alexander Merle, Stefano Morisi, Yusuke Shimizu, and Morimitsu Tanimoto. Neutrino Mass and Mixing: from Theory to Experiment. *New J. Phys.*, 16:045018, 2014.

[300] M. G. Aartsen et al. Flavor Ratio of Astrophysical Neutrinos above 35 TeV in Ice-Cube. *Phys. Rev. Lett.*, 114(17):171102, 2015.

[301] M. Re Fiorentin, V. Niro, and N. Fornengo. A consistent model for leptogenesis, dark matter and the IceCube signal. *JHEP*, 11:022, 2016.

[302] Samuel B. Roland, Bibhushan Shakya, and James D. Wells. PeV neutrinos and a 3.5 keV x-ray line from a PeV-scale supersymmetric neutrino sector. *Phys. Rev.*, D92(9):095018, 2015.

[303] Chee Sheng Fong, Hisakazu Minakata, Boris Panes, and Renata Zukanovich Funchal. Possible Interpretations of IceCube High-Energy Neutrino Events. *JHEP*, 02:189, 2015.

[304] A. Zee. Charged Scalar Field and Quantum Number Violations. *Phys. Lett.*, 161B:141–145, 1985.

[305] A. Zee. Quantum Numbers of Majorana Neutrino Masses. *Nucl. Phys.*, B264:99–110, 1986.

[306] K. S. Babu. Model of 'Calculable' Majorana Neutrino Masses. *Phys. Lett.*, B203:132–136, 1988.

[307] D. Aristizabal Sierra and M. Hirsch. Experimental tests for the Babu-Zee two-loop model of Majorana neutrino masses. *JHEP*, 12:052, 2006.

[308] Daniel Schmidt, Thomas Schwetz, and He Zhang. Status of the Zee–Babu model for neutrino mass and possible tests at a like-sign linear collider. *Nucl. Phys.*, B885:524–541, 2014.

[309] Tanja Geib, Stephen F. King, Alexander Merle, Jose Miguel No, and Luca Panizzi. Probing the Origin of Neutrino Masses and Mixings via Doubly Charged Scalars: Complementarity of the Intensity and the Energy Frontiers. *Phys. Rev.*, D93(7):073007, 2016.

[310] Hoang Ngoc Long and Vo Van Vien. Neutrino mixing with nonzero θ_{13} in Zee-Babu model. *Int. J. Mod. Phys.*, A29(13):1450072, 2014.

[311] Daniel Schmidt, Thomas Schwetz, and Takashi Toma. Direct Detection of Leptophilic Dark Matter in a Model with Radiative Neutrino Masses. *Phys. Rev.*, D85:073009, 2012.

[312] Isabel M. Oldengott, Daniel Boriero, and Dominik J. Schwarz. Reionization and dark matter decay. *JCAP*, 1608(08):054, 2016.